

TUMSAT-OACIS Repository - Tokyo

University of Marine Science and Technology

(東京海洋大学)

Observation of thin film wetting by a total reflection and interference fringe method

メタデータ	言語: eng 出版者: 公開日: 2021-06-25 キーワード (Ja): キーワード (En): 作成者: 李, 賀 メールアドレス: 所属:
URL	https://oacis.repo.nii.ac.jp/records/2171

Doctoral Dissertation

**OBSERVATION OF THIN FILM WETTING BY A TOTAL
REFLECTION AND INTERFERENCE FRINGE METHOD**

September 2020

**Graduate School of Marine Science and Technology
Tokyo University of Marine Science and Technology
Doctoral Course of Applied Marine Environmental Studies**

LI HE

Doctoral Dissertation

**OBSERVATION OF THIN FILM WETTING BY A TOTAL
REFLECTION AND INTERFERENCE FRINGE METHOD**

September 2020

**Graduate School of Marine Science and Technology
Tokyo University of Marine Science and Technology
Doctoral Course of Applied Marine Environmental Studies**

LI HE

Table of Contents

1. Introduction	1
1.1 Background	1
1.1.1 Wetting	1
1.1.2 Contact angle	2
1.1.3 Observation methods	7
1.2 Objective	1 1
1.3 Structure of this paper	1 2
References of chapter 1	1 3
2. Total reflection and interference fringe method	1 5
2.1 Background	1 5
2.2 Experimental principle	1 7
2.2.1 Calculation about the strong and weak conditions of the interferogram	1 7
2.2.2 Calculation of contact angle	2 1
2.2.3 Calculation of liquid surface profile	2 4
2.2.4 Total reflection method	2 7
2.3 Verification experiment	2 9
2.3.1 Outline of this section	2 9
2.3.2 Verification experiment of equation for contact angle	2 9
2.3.3 Verification experiment of equation for calculating the surface profile of the liquid	4 5
2.4 Wetting behavior of liquid on a super-hydrophilic surface	4 8
2.4.1 Experimental facilities and materials	4 8
2.4.2 Experimental procedure	5 1
2.5 Results	5 3
2.6 Conclusion	8 0
References of chapter 2	8 2
3. Cross-linking adhesive force of liquid bridge	8 3
3.1 Background	8 3
3.2 Calculation of cross-linking adhesive force	8 5
3.2.1 Calculation of Laplace pressure	8 5
3.2.2 Calculation of wetting force	8 6

3.3 Facilities and calibrations	8	7
3.3.1 Experimental facilities.....	8	7
3.3.2 Calibration of double cantilever spring	9	5
3.4 Experimental procedure	9	9
3.5 Results	1	0 4
3.6 Conclusion.....	1	1 1
References of chapter 3	1	1 2
4. Conclusion.....	1	1 3
Acknowledgements	1	1 4

1. Introduction

1.1 Background

1.1.1 Wetting

When a liquid comes into contact with a solid and keeps in contact with the surface of the solid by intermolecular interactions, this phenomenon is wetting. The wetting phenomenon is a very common phenomenon, no matter in nature or in a man-made system.

On rainy days, the tree leaves will be wet by rain and the leaf surface will be covered by water film. When the rain droplets on the lotus leaf will roll in an almost spherical shape without wetting the leaf surface. For rose, many small water drops will stick to the rose petals without dripping. In the animal world, ducks and geese can play in the water without worrying about being wet by water, but it seems impossible for chickens to play in the water. Plants and animals have different wetting characteristics, and they each take advantage of the favorable wettability to better adapt to the natural environment for survival [1~3].

For humans, people apply different wettability to many aspects, for example, in oil recovery [4], coating [1], friction [5, 6], printed electronics [7] and printing [8, 9]. So that, wettability plays a significant role. Specific applications include the water-repellency of window glass of the car, the non-adhesiveness of the yoghurt cap, and the self-cleaning characteristics of clothing and so on are all achieved by using poor wettability. And in machinery, lubricating oil between relatively moving parts should have a good wettability to

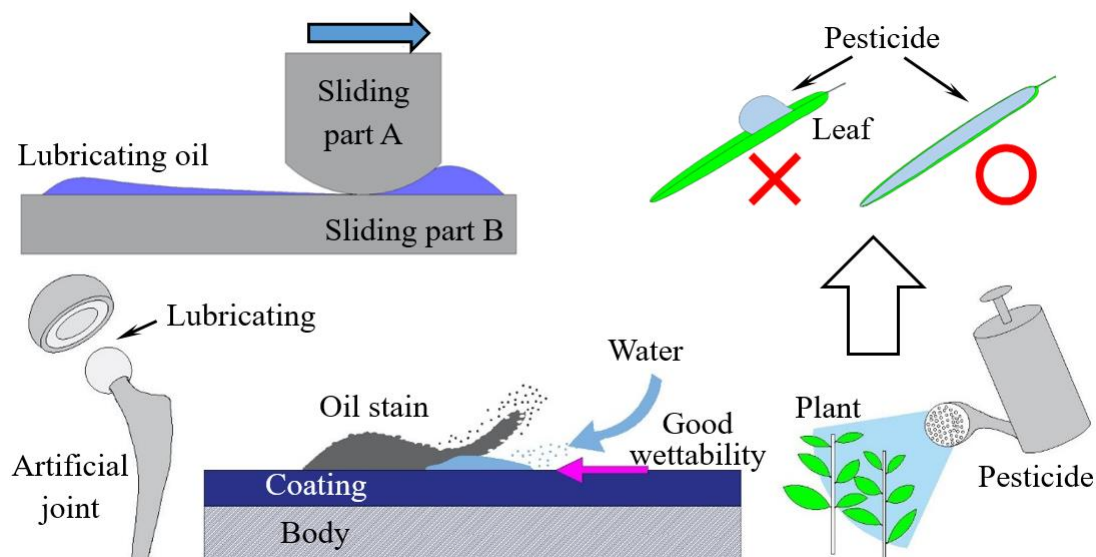


Figure 1.1 Schematic diagram of applications with good wettability.

achieve rapid recovery of the oil film. In agriculture, plants are sprayed with pesticide, and the leaf surfaces of the plants also need to have a good wettability to achieve a better effect. In addition, the lubrication of artificial joint and the decontamination of the coating on the surface of object also need good wettability. Figure 1.1 shows a schematic diagram of many applications with good wettability.

1.1.2 Contact angle

In the case of wetting when a droplet is placed on a fluid surface, the total free energy of the system tends to minimize, and finally reaches the equilibrium state. As shown in Figure 1.2 (a), three phases are A, B and C. The curve where the three phases meet is a three-phase line. In the side view, as shown in Figure 1.2 (b), the three dashed lines drawn from the three-phase line are the projections of the contact planes of the adjacent two phases. In the Figure 1.2 (c), if we only focus on these three dashed lines, the angles (interfacial angles) formed by the dashed lines are α , β and γ , respectively. Then we have:

$$\alpha + \beta + \gamma = 2\pi \quad (1-1)$$

Since it is in equilibrium, so the net force on any element of the three-phase line is zero. The interfacial tensions in the directions of these three dotted lines are σ_{AB} , σ_{BC} and σ_{AC} , respectively. Then there are equations about these interfacial tensions below [10]:

$$\sigma_{AB} + \sigma_{BC} \cos \beta + \sigma_{AC} \cos \alpha = 0 \quad (1-2)$$

$$\sigma_{AB} \cos \beta + \sigma_{BC} + \sigma_{AC} \cos \gamma = 0 \quad (1-3)$$

$$\sigma_{AB} \cos \alpha + \sigma_{BC} \cos \gamma + \sigma_{AC} = 0 \quad (1-4)$$

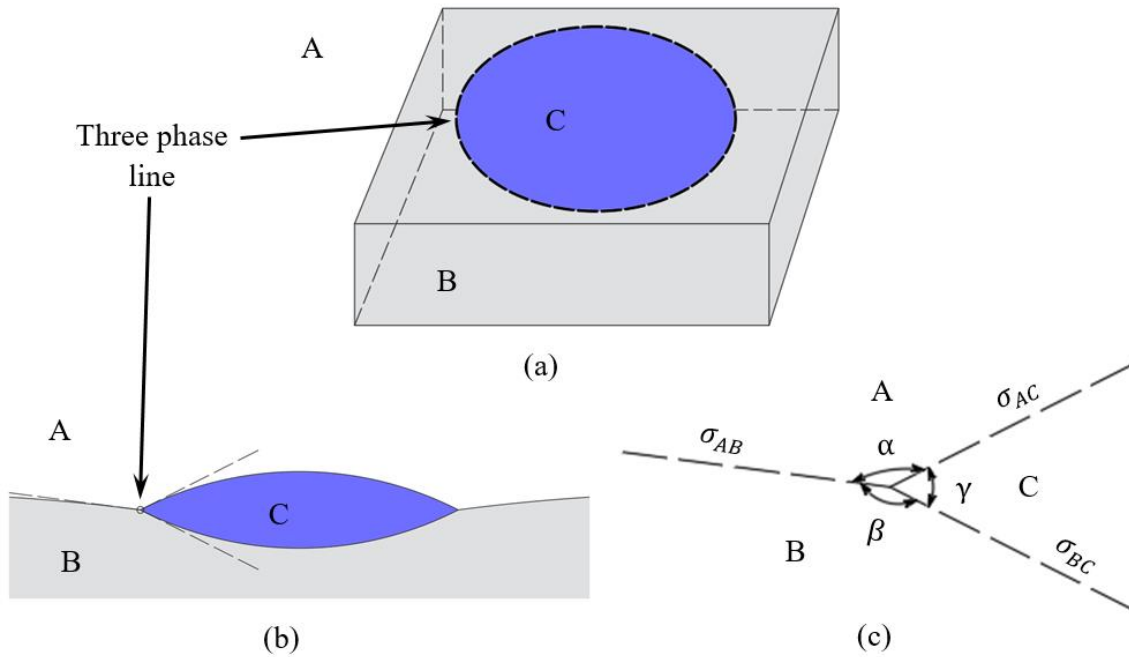


Figure 1.2 Schematic diagram of three interfacial angles which are formed at the three-phase line, when the droplet is placed on a fluid surface.

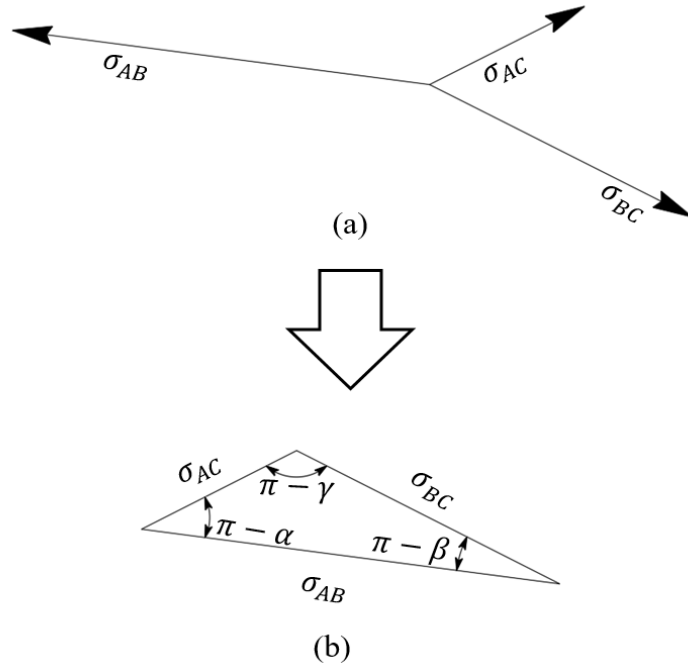


Figure 1.3 Schematic diagram of Neumann's triangle.

If the direction and length of the line segments with arrows are used to indicate the direction and magnitude of the interfacial tensions, then the relationship about these interfacial tensions is shown in Figure 1.3 (a). These three line segments can form a triangle through parallel displacement. As Figure 1.3 (b) shows, the triangle is known as Neumann's triangle [11]. Since the Neumann's triangle is a plane triangle, its net force is always vanished. According to the theorem of sine and cosine in the geometric relationship, the length of any side of a triangle changes, and at least two of its internal angles will change. Therefore, the relations between the sizes of the interfacial angles depend on the surface tensions.

In a simpler scenario, for example, in the gas-liquid-solid system. The surface tension of solid-gas interface is σ_{SG} , the surface tension of gas-liquid interface is σ_{GL} , and the surface tension of solid-liquid interface is σ_{SL} . The equilibrium state of the gas-liquid-solid system formed by the balance of σ_{SG} , σ_{GL} and σ_{SL} . The gas-liquid-solid three phases meet at the so-called three-phase contact line. Usually, the contact line is defined to be the locus of points that are simultaneously in contact with the gas, liquid and solid phases [12]. The contact angle is the angle in the liquid phase, formed by the gas-liquid interface and the solid-liquid interface at the contact line. Then we can have the well-known Young's equation [13]:

$$\sigma_{SG} = \sigma_{SL} + \sigma_{GL} \cos \theta_{eq} \quad (1 - 5)$$

In the equation, θ_{eq} is the contact angle when the three phases are in equilibrium. Figure 1.4 shows the magnitudes and directions of surface tensions in equilibrium expressed in the

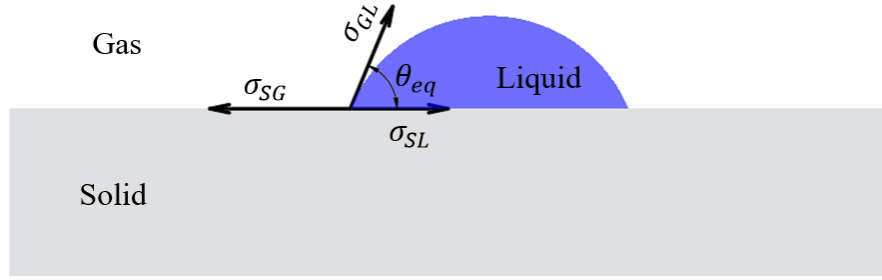


Figure 1.4 Schematic diagram of magnitudes and directions of surface tensions in equilibrium expressed in the Young's equation.

Young's equation. From the figure, it can be seen that the net force in the direction along the solid surface vanishes.

However, the Young's equation is under ideal condition, established on a rigid plane without defects, and expresses the relationship between the contact angle and surface tensions at equilibrium. Under this ideal condition, the advancing angle θ_A equals to the receding angle θ_R when the liquid moves slowly. When there are defects on the plane, the advancing angle and the receding angle are no longer equal, and there is a relationship: $\theta_R < \theta_{eq} < \theta_A$. While, the absolute values between advancing angle to equilibrium angle and receding angle to equilibrium angle are different: $|\theta_A - \theta_{eq}| \neq |\theta_R - \theta_{eq}|$. The advancing angle and the receding angle have a certain relationship with the equilibrium angle, and the equilibrium angle θ_{eq} can be calculated by the θ_A and θ_R with the equations below [14]:

$$\theta_{eq} = \cos^{-1} \left(\frac{\Gamma_A \cos \theta_A + \Gamma_R \cos \theta_R}{\Gamma_A + \Gamma_R} \right) \quad (1-6)$$

In this equation:

$$\Gamma_A \equiv \left(\frac{\sin^3 \theta_A}{(2 - 3 \cos \theta_A + \cos^3 \theta_A)} \right)^{\frac{1}{3}} \quad (1-7)$$

And

$$\Gamma_R \equiv \left(\frac{\sin^3 \theta_R}{(2 - 3 \cos \theta_R + \cos^3 \theta_R)} \right)^{\frac{1}{3}} \quad (1-8)$$

When a droplet is placed on a plane solid surface and changes from nonequilibrium to equilibrium, when the contact angle decreases, the tendency of spreading increases. So that, the contact angle is a useful inverse measure of wettability [15].

Apply the Neumann's triangle in the situation of gas-liquid-solid system, usually we can get the relationship:

$$\sigma_{SG} < \sigma_{SL} + \sigma_{GL} \quad (1 - 9)$$

Under this condition, the liquid has a finite contact angle, and the wetting at this moment is a partial wetting. However, in particular, in the Young's equation, when the equilibrium angle $\theta_{eq} = 0$:

$$\sigma_{SG} = \sigma_{SL} + \sigma_{GL} \quad (1 - 10)$$

The liquid under this condition, will continue to spread until forms a uniform liquid layer covering the solid surface. And the wetting at this moment is called complete wetting [16].

The surface free energy σ_{SG} has relation to the wetting state. The equilibrium spreading coefficient S is used to distinguish the different wetting states, and the S can be represented by σ_{SG} related equation:

$$S \equiv \sigma_{SG} - (\sigma_{SL} + \sigma_{GL}) = \sigma_{GL}(\cos \theta_{eq} - 1) \quad (1 - 11)$$

When the $S = 0$, it is complete wetting, and when $S < 0$, it is partial wetting. In addition, there is another wetting condition. Contrary to complete wetting, when the contact angle is 180° , the liquid forms a plane parallel to the solid surface, that is, the solid is not wet by the liquid. This wetting condition is complete dry. Figure 1.5 is a schematic diagram of the conversion relationship of these three wetting conditions.

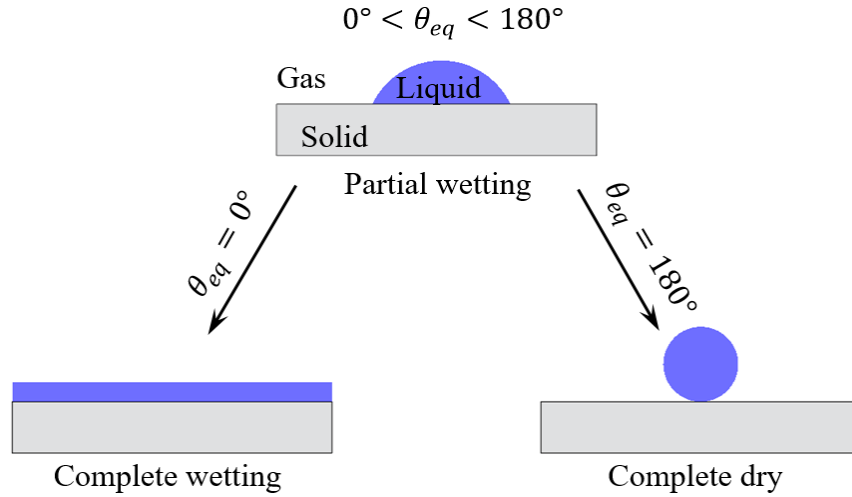


Figure 1.5 Schematic diagram of the conversion relationship of the partial wetting, complete wetting and complete dry.

Generally the wetting that can be seen is partial wetting. In the partial wetting, when the water droplet is placed on a solid surface, the wettability of the solid surface can be divided into several types, based on the size of the contact angle. They are superhydrophilic (the contact angle θ_{eq} turns smaller than 5°), hydrophilic (the contact angle: $\theta_{eq} < 90^\circ$),

hydrophobic (the contact angle: $90^\circ < \theta_{eq} < 180^\circ$) and superhydrophobic (the contact angle: $150^\circ < \theta_{eq} < 180^\circ$) [17]. Figure 1.6 is the diagram of contact angle of water droplets with different surface wettability [18].

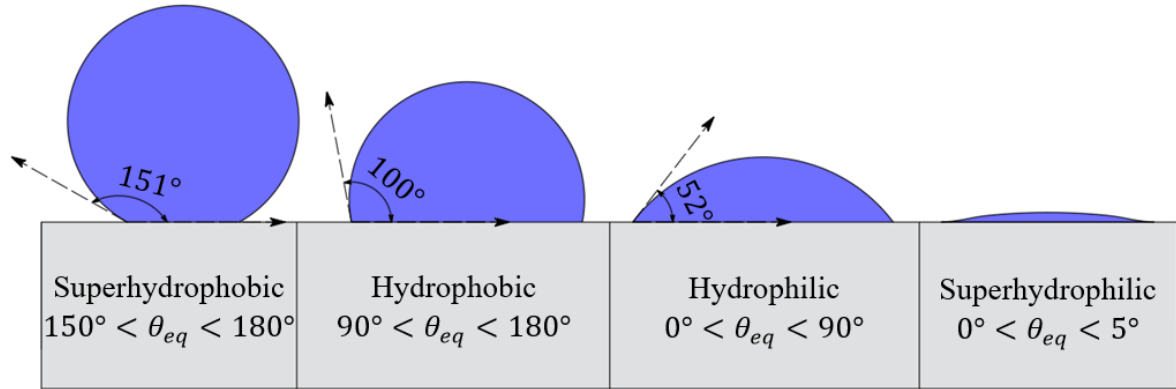


Figure 1.6 Diagram of contact angle of water droplets with different surface wettability. In the figure, the dotted lines with arrow indicate the direction of the surface tension between water and air, and the direction of the interfacial tension between water and solid. And the length of the lines do not indicate the magnitude.

1.1.3 Observation methods

Since contact angle can be used to evaluate the wettability of solids in contact with liquids, many methods of observing contact angle have been developed in the process of studying the wettability.

(I) Side view method:

Among a lot of observation methods, the side view method is relatively common and has been widely used for years. The schematic diagram of the device structure of the side view method is shown in Figure 1.7 (a), which is mainly composed of three parts: a light source, a substrate on which a droplet is placed, and a camera for observation. Figure 1.7 (b) shows an example of the contact angle of a water droplet on a glass substrate observed by the side view method. The hemispherical shape of the water droplet can be seen, and the commonly used method of calculating the contact angle is $\theta/2$ method. As shown in Figure 1.7 (c), connect the apex of the droplet to one point of the contact line on one side of the droplet with dotted line. The angle formed by this dotted line and the solid-liquid interface is half of the contact angle θ , that is, $\theta/2$.

The side view method is characterized by a simple structure, intuitive observation of droplets and a relatively large measurable angle range. But the shortcomings are also very obvious, that is, the measurement accuracy is relatively low (it is said that the measurement accuracy is $\pm 1^\circ \sim 2^\circ$ [19]) and it is very difficult to measure the contact angle and contact line in the case of superhydrophilicity. Figure 1.7 (d) shows an ethanol droplet is placed on a glass plate, and the contact angle and contact line of the droplet is difficult to observe.

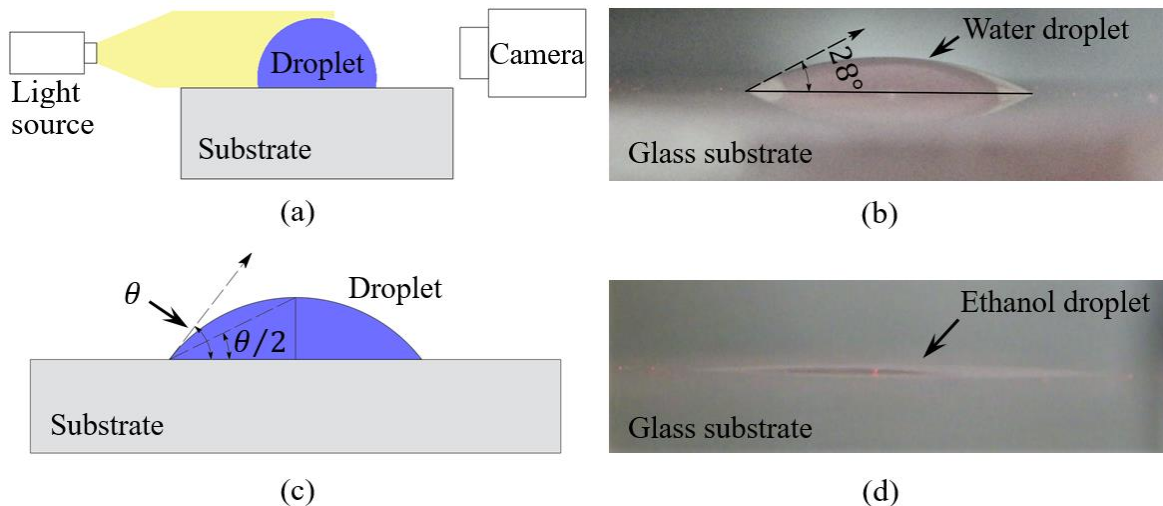


Figure 1.7 Introduction of side view method. Figure 1.7 (a) shows the schematic diagram of the device. Figure 1.7 (b) shows the contact angle of a water droplet on a glass substrate. Figure 1.7 (c) indicates the $\theta/2$ method. Figure 1.7 (d) shows an ethanol droplet on a glass plate.

(II) Reflection of a laser beam method:

Different from the side view method, the reflection of a laser beam method uses the range of the reflected laser on the screen for observation of contact angle. Figure 1.8 (a) and (b) show two types of the reflection of a laser beam method [20, 21]. Both of the two types are mainly composed of four parts: a laser, flat mirror for reflection, screen and camera for observation. In addition, the observation method in Figure 1.8 (a), the substrate is made of transparent material (such as a glass plate), and there is a flat plate for observation below the substrate. However, the material of the substrate in the observation method in Figure 1.8 (b) does not need a transparent material, and the screen for observation is placed vertically.

The principle of the two types of the reflection of a laser beam method is almost the same. As an example, in Figure 1.8 (c), a top-down laser beam is reflected at the edge of the droplet, and the reflected laser beam arrives at the screen which is placed horizontally above the droplet. By measuring the horizontal distance l which is between the position of the laser at the screen and the edge of the droplet, and the vertical height h of the screen, the angle α can be calculated according to the trigonometric function. Finally, the contact angle θ

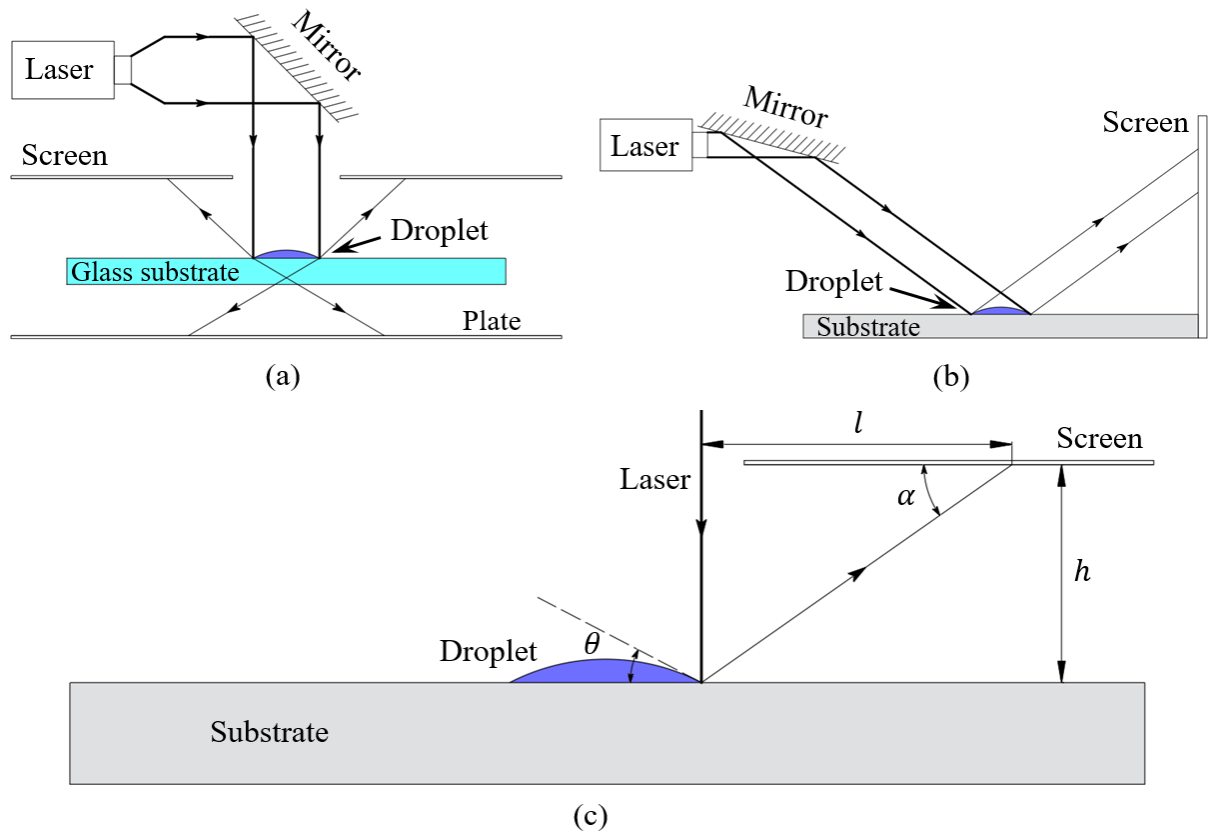


Figure 1.8 Introduction of reflection of a laser beam method. Figure 1.8 (a) and (b) show the schematic diagrams of the two types of device. Figure 1.8 (c) shows the measuring principle of the contact angle.

can be calculated by the relation $\theta = (90^\circ - \alpha)/2$. This reflection of a laser beam method is used for contact angle $\theta > 4^\circ$ with an accuracy of $\pm 0.5^\circ$ [22].

(III) Interference fringe method:

When the substrate is superhydrophilic, usually, the interference fringe method can be used to observe the wettability. The interference fringe method has the features of high measurement accuracy, available for small angles and measurable for film with thickness at micro/nano-meter levels. For example, the interferential reflection contrast microscopy can measure the contact angle $1^\circ < \theta < 4^\circ$ with high accuracy of $\pm 0.01^\circ$ [22]. A schematic diagram of a specific interference fringe method is shown in Figure 1.9 (a). Compared with the methods described above, the device of this method is slightly more complicated. The device is composed of laser, beam splitter, objective lens, substrate and camera. The image

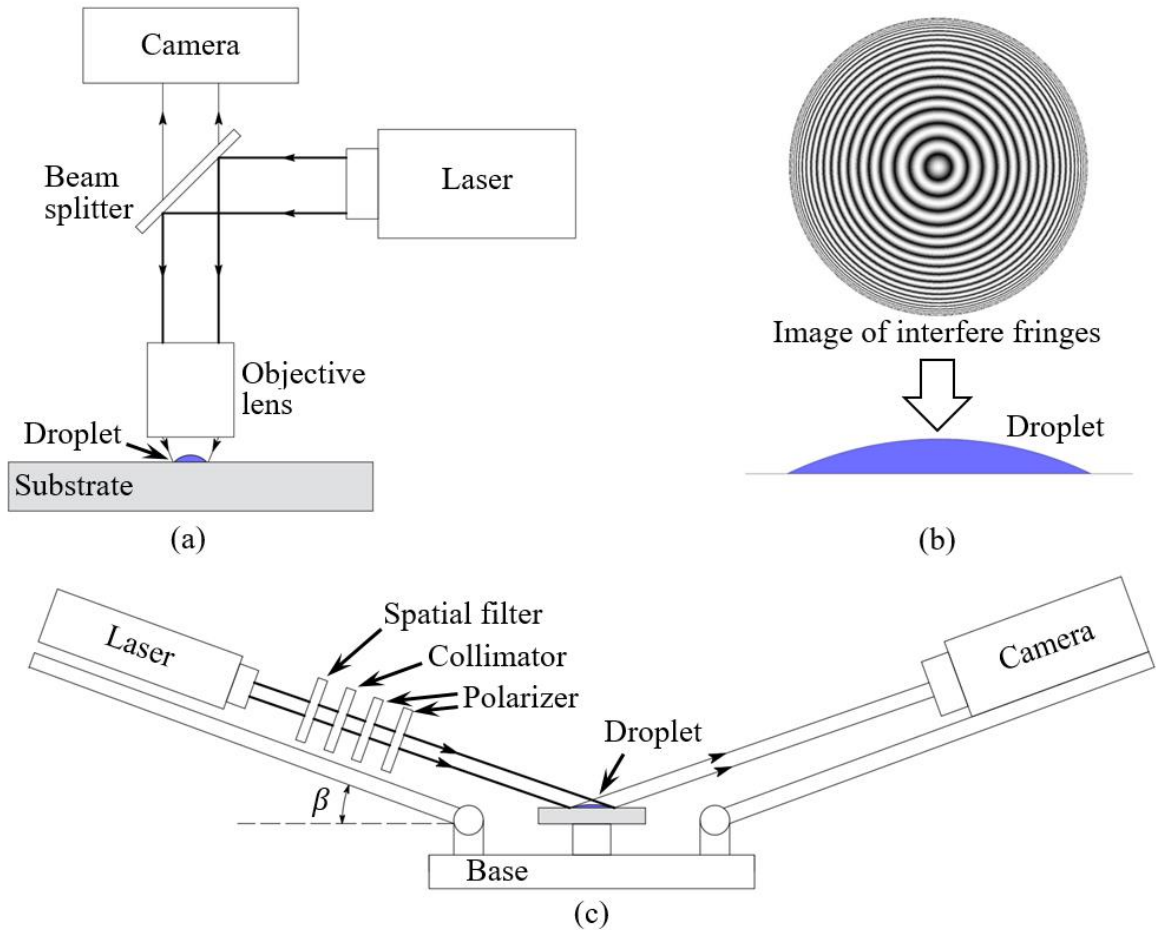


Figure 1.9 Introduction of interfere fringe method. Figure 1.9 (a) shows the schematic diagram of the device of a fringe method. Figure 1.9 (b) shows an image of interference fringes of a droplet observing by the fringe method of Figure 1.9 (a). Figure 1.9 (c) shows the schematic diagram of the Brewster angle microscope.

of the observation result is shown in Figure 1.9 (b), and a lot of fringes can be seen in the image. The measurement and calculation of the spacing of fringes are required to obtain information such as contact angle and film thickness. Information such as contact angle and film thickness can be obtained by measuring the fringe spacing and the subsequent calculation [23, 24]. When the thickness of the film is tens micrometer or even nanometer, the Brewster angle microscope can also be used to observe it [25, 26]. Figure 1.9 (c) is a schematic diagram of the device. The laser passes through the spatial filter, collimator and polarizer to form a parallel and single-direction polarized laser beam. By setting the angle β , the wetting area reflects the laser beam, while the non-wetting area does not reflect the laser beam. Thus, the contact line can be precisely measured, the contact angle and the thickness of the liquid film can also be measured at the same time.

When studying the hydrophilicity and superhydrophilicity, some of the interference fringe methods can usually be available. But, there is a problem when the liquid is located between two planes that have a narrow gap or when an object on the liquid [26, 27], observation cannot be performed because the light for interfering is blocked.

1.2 Objective

The objective of this paper is to develop a fringe method with oblique upward laser. And with this method study the wetting phenomenon and find the factors that affect spreading.

By developing this method, in the condition of superhydrophilicity, the contact angle and surface profile could be evaluated by observing interference fringes without considering whether the liquid is located between two planes that have a narrow gap or when there is an object on the liquid. And at the same time, the contact line can also be precisely determined.

In the spreading experiment, the relationship between the wetting diameter-time of several liquids, and the contact angle-diameter-time relationship of silicone oil are observed. Analyze and study the relationship between liquid parameters and the laws that appear in the spreading process through experimental results. Finally, find the factors that affect spreading.

By observing the liquid wetting behavior under superhydrophilic conditions, the liquid wetting phenomenon is studied.

For the liquid bridge experiment, the purpose is to investigate the influence of the liquid contact angle and the wetting diameter on the cross-linking adhesive force of the liquid bridge when it is hydrophilicity/superhydrophilicity between the liquid and the substrate to be contacted.

1.3 Structure of this paper

In this paper, chapter 1 introduces what is wetting and its importance in daily life and production. The wetting phenomenon from the physical level is explained and the classification and evaluation method of wettability is introduced. Finally, several methods which are commonly used to observe the wettability are introduced.

In chapter 2, the development of the experimental method used in this study is introduced. The first is the establishment of the theory of the experimental method. Before performing the verification experiment, the calculation equation is derived. The calculation results obtained from the verification experiment are in good agreement with the experimental results, thus the availability of this interference fringe method is proved. This method was used to observe the wetting phenomenon of several liquids, and the wetting phenomenon under superhydrophilicity was studied.

In the chapter 3, the experiment of liquid bridging and breaking is performed. In the chapter, the theoretical calculation is first introduced, and then the experimental equipment is calibrated. Finally, the liquid bridge experiment is performed with several liquids, and the process of which is observed by using the developed method and the side view method simultaneously.

Chapter 4 is the conclusion of this paper. In this chapter, the conclusions of the three experiments in this paper are briefly described.

References of chapter 1

- [1] Bonn, D.; Eggers, J.; Indekeu, J.; Meunier, J.; Rolley, E. Wetting and spreading. *Reviews of Modern Physics* 2009, **81**, 739-805.
- [2] Ju, J., H. Bai, Y. Zheng, T. Zhao, R. Fang, and L. Jiang. 2012. A multi-structural and multi-functional integrated fog collection system in cactus. *Nature Communications* **3**:1247.
- [3] Taylor, P. The wetting of leaf surfaces. *Current Opinion in Colloid & Interface Science* 2011, **16**, 326-34.
- [4] Bertrand, E.; Bonn, D.; Broseta, D.; Dobbs, H.; Indekeu, J.; Ragil, K.; Shahidzadeh, N. Wetting of alkanes on water. *Journal of Petroleum Science and Engineering* 2002, **33**, 217-222.
- [5] Klein, J.; Perahia, D.; Warburg, S. Forces between polymer-bearing surfaces undergoing shear. *Nature* 1991, **352**, 143-145.
- [6] Guo, F.; Li, X. M.; Wong, P. L. A novel approach to measure slip-length of thin lubricant films under high pressures. *Tribology International* 2012, **46**, 22-29.
- [7] Liu, X. Y.; Kanehara, M.; Liu, C.; Sakamoto, K.; Yasuda, T.; Takeya, J.; Minari, T. Spontaneous patterning of high-resolution electronics via parallel vacuum ultraviolet. *Advanced Materials* 2016, **28**, 6568-6573.
- [8] Yoon, H.S.; Lee, H.T.; Kim, E.S.; Ahn, S.H. Direct printing of anisotropic wetting patterns using aerodynamically focused nanoparticle (AFN) printing. *Applied Surface Science* 2017, **396**, 1450-1457.
- [9] Liu, F.; Shen, W. Forced wetting and dewetting of liquids on solid surface and their roles in offset printing. *Colloids and surfaces A: Physicochemical and engineering aspects* 2008, **316**, 62-69.
- [10] Rowlinson, J.S.; Widom, B. (1982). *Molecular Theory of Capillarity*. Oxford, UK: Clarendon Press.
- [11] Neumann, F. *Vorlesungen über die Theorie der Capillarität*; Teubner, B.G.: Leipzig, 1894.
- [12] Ye, X.M.; Zhang, X.S.; Li, M.L. Contact line dynamics of two-dimensional evaporating drops on heated surfaces with temperature-dependent wettabilities. *International Journal of Heat and Mass Transfer* 2019, **128**, 1263-1279.
- [13] Young, T. An essay on the cohesion of fluids, *Philos Trans R Soc Lond* 1805, **95**, 65-87.
- [14] Rafael, T. Line energy and the relation between advancing, receding and Young contact angles. *Langmuir* 2004, **20**, 7659-64.
- [15] Shafrin, E. G.; Zisman, W. A. Constitutive relations in the wetting of low energy surfaces and the theory of the retraction method of preparing monolayers. *The Journal of*

Physical Chemistry 1960, **64**, 519-524.

[16] Klein, J.; Perahia, D.; Warburg, S. Forces between polymer-bearing surfaces undergoing shear. *Nature* 1991, **352**, 143-145.

[17] Ahmad, D.; Boogaert, I.V.D. Hydrophilic and hydrophobic materials and their applications. *Energy Sources, Part A: Recovery, Utilization, and Environmental Effects* 2018, **40**, 22.

[18] Alharbi, A. R.; Alarifi, I. M.; Khan, W. S. and Asmatulu, R. Highly hydrophilic electrospun polyacrylonitrile/polyvinylpyrrolidone nanofibers incorporated with gentamicin as filter medium for dam water and wastewater treatment. *Journal Membrane Separation Technological* 2016, **5**, 38-56.

[19] Johnson, R. E.; Dettre, R. H. Wettability and contact angles. *Surface and Colloid Science*, Matijevic, E., Eds.; John Wiley & Sons Inc: New York, 1969; Vol. 2, pp 85-153.

[20] Allain, C.; Ausserre, D.; Rondelez, F. A new method for contact-angle measurements of sessile drops. *Journal of Colloid and Interface Science* 1985, **107**, 5-13.

[21] Zhu, F.; Miao, R.C.; Zhang, Y.N. A contact angle measurement by laser glancing incidence method. *Journal of Applied Physics* 2008, **104**, 063112.

[22] Fondecave, R.; Wyart, F. B. Polymers as dewetting agents. *Macromolecules* 1998, **31**, 9305-9315.

[23] Gokhale, S. J.; Plawsky, J. L. Experimental investigation of contact angle, curvature, and contact line motion in dropwise condensation and evaporation. *Journal of Colloid and Interface Science* **2003**, 259, 354-366.

[24] Kariyasaki, A.; Yamasaki, Y. Measurement of liquid film thickness by a fringe method. *Heat Transfer Engineering* **2009**, 30, 28-36.

[25] Hashimoto, S.; Hong, C. Transient growth process of precursor film at early stage of droplet spreading. *Journal of Thermal Science and Technology* **2012**, 7, 487-496.

[26] Mu, L.; Kondo, D. Sharp acceleration of a macroscopic contact line induced by a particle. *Journal of Fluid Mechanics* **2017**, 830, R1.

[27] Tanaka, K.; Iwamoto, K. Effective shear displacement on lateral adhesion force of a liquid bridge between separated plates. *Tribology Letters* **2016**, 64.

2. Total reflection and interference fringe method

2.1 Background

In various studies on wettability, a lot of studies have been conducted on hydrophobicity/superhydrophobicity due to its extensive antifouling and waterproof applications. In recent years, with the extensive application of hydrophilic/superhydrophilic materials in many aspects, for example the surface coating for rapid and robust membrane distillation desalination [1], application for backlight microfluidic chip [2] and coating for self-cleaning in solar panels [3] and so on, the study of hydrophilicity is very important.

The commonly used observation methods have been introduced in the chapter 1, the interference fringe method is a widely used method to observe the liquid wetting behavior on the superhydrophilic surface. All of the interference fringe methods introduced above are all methods which are using the laser irradiates from above the observing object. Although they are able to meet the most needs of the observation of superhydrophilic behavior, as mentioned in chapter 1, if the liquid being observed is located between two surfaces with a narrow gap or other object are placed on the liquid, the observation cannot be performed because the laser is blocked. In the two cases shown in Figure 2.1, the interference fringe method cannot be performed.

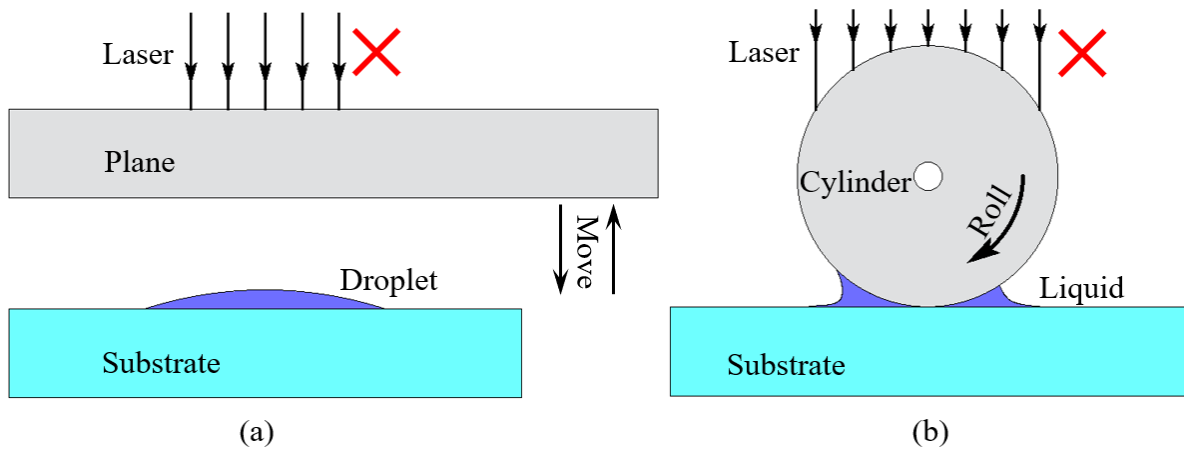


Figure 2.1 Schematic diagram of two examples that cannot be used with the interference fringe method introduced above. Figure 2.1 (a) shows a droplet is located between two surfaces with a narrow gap. Figure 2.1 (b) shows a cylinder is placed above a liquid. Both are due to objects blocking the laser, which is irradiated from above the liquid, that makes it impossible to observe the wettability such as the contact angle of the liquid.

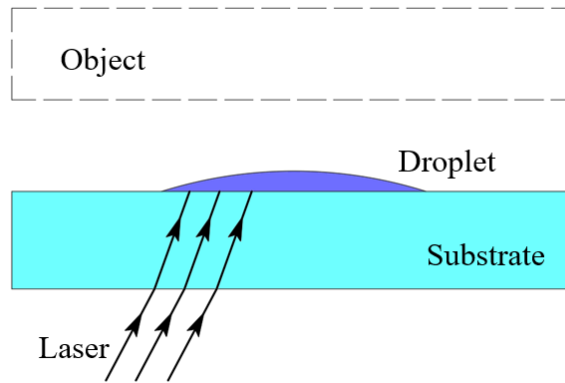


Figure 2.2 Schematic diagram of locations of laser and droplet in the observation method of interference fringe with oblique upward laser. The laser is irradiated from bottom of the liquid to be observed at a certain angle to form interference fringes at the interface between the substrate and the liquid. The spacing between adjacent fringes varies according to the shape of the interface between the liquid and the air.

Therefore, in order to be able to observe the liquid wetting behavior on superhydrophilic surface, without considering the existence of objects above the liquid blocking the laser, in the research of this paper, the observation method of interference fringe with oblique upward laser is developed. Figure 2.2 shows the schematic diagram of locations of laser and droplet in the developed method.

Although the total reflection method and the interference fringe method are both widely used, we first combine the two methods into one method to observe the wetting phenomena.

With this method, in machinery, as shown in the example of relative motion in Figure 1.1 and Figure 2.1, the change in the thickness of the lubricating oil film in relative motion can be measured. And in lubrication, this method can be used to determine that the area in the narrow gap is filled with oil or dry. This is important for detecting lubrication status and reducing friction loss.

2.2 Experimental principle

2.2.1 Calculation about the strong and weak conditions of the interferogram

Two coherent lights emitted by the same laser, if they have the same phase at the initial time, in the process of propagation, one of the lights passes through more light path than the other by refraction/reflection, interference will occur when the two lights meet. As shown in Figure 2.3, light 1 intersects light 2 after two reflections, and interferes with light 2 at the

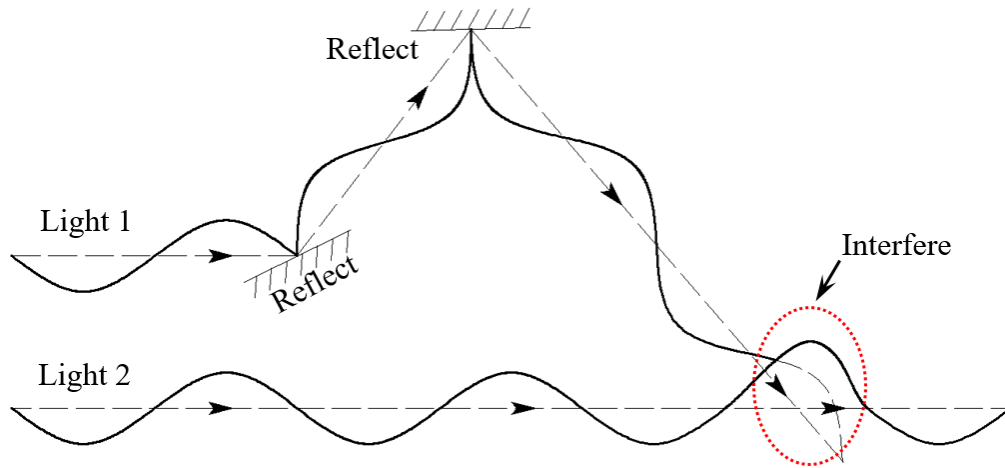


Figure 2.3 Schematic diagram of interference. In the figure, the dotted line with arrows represents the direction of light propagation. Light 1 reflects twice, and when it interferes with light 2, it travels one wavelength longer than light 2. At this moment, the effect of interference is that the amplitude of the wave becomes larger.

intersection. Such interference principle is applied to the interference fringe method.

In this experiment, the observation method is interference fringe method with oblique upward laser. Figure 2.4 shows a schematic diagram of the generation of interference fringe in this experiment. When a droplet is placed on a glass substrate and forms a liquid film, if only the surface profile of the liquid film near the contact line is concerned, the curve at the air-liquid interface can be approximated as a straight line. Figure 2.4 schematically shows the profile of liquid film near the contact line on the glass substrate, for which the contact angle is β . Light E_1 enters and refracts at point A on the liquid-glass interface with incident angle θ_i and penetrates into the liquid, and then reflects at point B on the air-liquid interface, finally, refracts at point C on the liquid-glass interface. Coherent light E_2 intersects light E_1 at point C . The point H on light E_1 and point C on light E_2 have same phase. $HB + BC = L$ is the optical path difference between reflected light of E_1 and

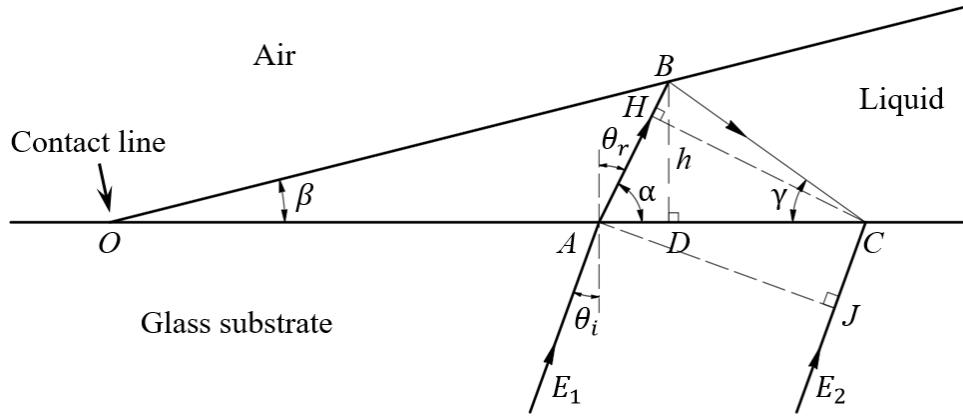


Figure 2.4 Schematic diagram of the interference of two lights in this experiment. The contact angle of the liquid and glass substrate is β . Two lights E_1 and E_2 have the same phase at point A and point J . At point H and point C , the two lights also have the same phase. The light E_1 is reflected by the air-liquid interface to point C , and interferes with E_2 . The dashed lines AJ , BD and CH are perpendicular to CJ , AC and AB , respectively.

light E_2 at point C . When the phase difference between the lights is an even multiple of π , constructive interference occurs, and the intensity of the interferogram is strong (light fringe). Similarly, when the phase difference is an odd multiple of π , destructive interference occurs, and the intensity of the interferogram is weak (dark fringe). The optical path difference of one wavelength corresponds to one phase difference of 2π .

The specific calculation process of interference is as follows:

First here introduce the meaning of various symbols.

α : the angle between light E_1 and the liquid-glass substrate interface.

γ : the angle between reflected light E_1 and the glass substrate-liquid interface.

θ_i : the angle of incidence when light enters the liquid.

θ_r : refraction angle when light enters the liquid.

t : the time that light takes from point J to point C .

c_0 : speed of light in vacuum.

λ_0 : wave length of light in vacuum.

λ : wave length of light in liquid.

h : distance from point B to liquid-glass interface.

n_a , n_l and n_g are the refractive index of air, liquid and glass substrate respectively.

According to Snell's law,

$$\sin \theta_i = n_l \sin \theta_r / n_g$$

Since light E_1 and light E_2 are parallel,

$$CJ = AC \cdot \sin \theta_i \quad (2-1)$$

$$t = \frac{CJ \cdot n_g}{c_0} \quad (2-2)$$

When light E_2 propagates from point J to point C , light E_1 propagates from point A to point H ,

$$AH = \frac{t \cdot c_0}{n_l} \quad (2-3)$$

According to the Equations (2-1), (2-2) and (2-3), we can get,

$$AH = AC \cdot \sin \theta_r \quad (2-4)$$

In triangle ABC , according to angles α and γ , using trigonometric functions, we can express AD and DC with the equations about h ,

$$AD = \frac{h}{\tan \alpha} \quad (2-5)$$

$$DC = \frac{h}{\tan \gamma} \quad (2-6)$$

Then,

$$AC = AD + DC = \frac{h}{\tan \alpha} + \frac{h}{\tan \gamma} \quad (2-7)$$

$$AH = AC \cdot \cos \alpha = h \cdot \left(\frac{1}{\tan \alpha} + \frac{1}{\tan \gamma} \right) \cdot \cos \alpha \quad (2-8)$$

$$AB = \frac{h}{\sin \alpha} \quad (2-9)$$

$$BC = \frac{h}{\sin \gamma} \quad (2-10)$$

As mentioned before, $HB + BC = L$ is the optical path difference between reflected light of E_1 and light E_2 at point C , then

$$\begin{aligned} L &= HB + BC \\ &= AB + BC - AH \\ &= \frac{h}{\sin \alpha} + \frac{h}{\sin \gamma} - h \cdot \left(\frac{1}{\tan \alpha} + \frac{1}{\tan \gamma} \right) \cdot \cos \alpha \\ &= h \cdot \left(\frac{1}{\sin \alpha} + \frac{1}{\sin \gamma} - \frac{\cos^2 \alpha}{\sin \alpha} - \frac{\sin \alpha}{\tan \gamma} \right) \\ &= h \cdot \left(\frac{1 + \sin \alpha \cdot (\sin \gamma - \cos \gamma)}{\sin \gamma} \right) \end{aligned} \quad (2-11)$$

The relationships about α , β and γ are as follows,

$$\alpha = \beta + \angle OBA$$

$$\angle OBA = \beta + \gamma$$

Then,

$$\gamma = \alpha - 2\beta \quad (2 - 12)$$

$$L = h \cdot \left[\frac{1 + \sin \alpha \cdot \{\sin(\alpha - 2\beta) - \cos(\alpha - 2\beta)\}}{\sin(\alpha - 2\beta)} \right] \quad (2 - 13)$$

The wavelength of light in liquid is

$$\lambda = \frac{\lambda_0}{n_l}$$

As light E_1 is reflected at the air-liquid interface, its phase changes by π . So the strong and weak conditions at point C where interference occurs are as follows,

strong (light fringe):
$$L = \left(m + \frac{1}{2}\right) \lambda$$

weak (dark fringe):
$$L = m\lambda$$

where the m in the equations is an integer.

2.2.2 Calculation of contact angle

When the liquid forms a contact angle β on the glass substrate, the schematic diagram of laser transmission and interference is shown in Figure 2.5. λ_0 , λ and n_l have the same meaning as described in section 2.2.1 above. In addition, the meaning of the other symbols in Figure 2.5 are as follows:

h_1 : distance from point B_1 to liquid-glass interface.

h_2 : distance from point B_2 to liquid-glass interface.

Y_1 : distance from contact line to No. m bright fringe (or dark fringe).

Y_2 : distance from contact line to No. $(m + 1)$ bright fringe (or dark fringe).

x : distance between two adjacent bright fringes (or dark fringes)

The specific calculation process about contact angle and interference fringes are as follows:

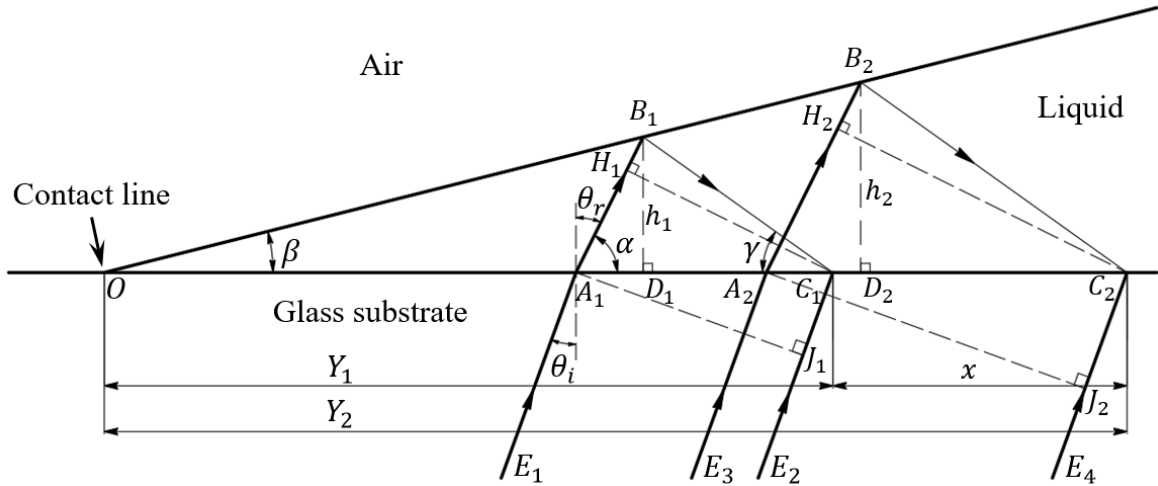


Figure 2.5 Schematic diagram of relationship between spacing of interference fringe and contact angle. The liquid is placed on the glass substrate and forms a film with a contact angle of β . At points C_1 and C_2 , there are two adjacent dark fringes. The contact angle β equals the inclination angle of the line where the reflection points B_1 and B_2 are located. θ_i is the angle of incidence and θ_r is the angle of refraction. Angle α and γ are the angles between light E_1 and the liquid-glass substrate interface.

First, we can get the equation about x ,

$$x = Y_2 - Y_1 \quad (2 - 14)$$

As the same with the relationship in Equation (2 - 9), we can get

$$A_1 B_1 = \frac{h_1}{\sin \alpha} \quad (2 - 15)$$

$$B_1C_1 = \frac{h_1}{\sin \gamma} \quad (2-16)$$

$$A_2B_2 = \frac{h_2}{\sin \alpha} \quad (2-17)$$

$$B_2C_2 = \frac{h_2}{\sin \gamma} \quad (2-18)$$

When light E_2 propagates from point J_1 to point C_1 , light E_1 propagates from point A_1 to point H_1 . The same for the lights E_3 and E_4 , when light E_4 propagates from point J_2 to point C_2 , light E_3 propagates from point A_2 to point H_2 . According to the Equation (2-8), we can have

$$A_1H_1 = A_1C_1 \cdot \cos \alpha = h_1 \cdot \left(\frac{1}{\tan \alpha} + \frac{1}{\tan \gamma} \right) \cdot \cos \alpha \quad (2-19)$$

$$A_2H_2 = A_2C_2 \cdot \cos \alpha = h_2 \cdot \left(\frac{1}{\tan \alpha} + \frac{1}{\tan \gamma} \right) \cdot \cos \alpha \quad (2-20)$$

In this calculation, only the dark fringe is counted. Therefore, the optical path difference between E_1 and E_2 at point C_1 , $L_1 = m\lambda$. And the optical path difference between E_3 and E_4 at point C_2 , $L_2 = (m+1)\lambda$. Thus,

$$L_1 = A_1B_1 + B_1C_1 - A_1H_1 = m\lambda \quad (2-21)$$

$$L_2 = A_2B_2 + B_2C_2 - A_2H_2 = (m+1)\lambda \quad (2-22)$$

So,

$$\begin{aligned} \lambda &= L_2 - L_1 \\ &= A_2B_2 + B_2C_2 - A_2H_2 - (A_1B_1 + B_1C_1 - A_1H_1) \\ &= h_2 \cdot \left\{ \frac{1 + \sin \alpha \cdot (\sin \gamma - \cos \gamma)}{\sin \gamma} \right\} - h_1 \cdot \left\{ \frac{1 + \sin \alpha \cdot (\sin \gamma - \cos \gamma)}{\sin \gamma} \right\} \\ &= (h_2 - h_1) \cdot \left\{ \frac{1 + \sin \alpha \cdot (\sin \gamma - \cos \gamma)}{\sin \gamma} \right\} \end{aligned} \quad (2-23)$$

Due to

$$OD_1 = \frac{h_1}{\tan \beta} \quad (2-24)$$

$$OD_2 = \frac{h_2}{\tan \beta} \quad (2-25)$$

Thus,

$$D_1D_2 = \frac{h_2 - h_1}{\tan \beta} \quad (2-26)$$

The distance x between two adjacent fringes can be expressed as

$$x = Y_2 - Y_1 = D_2C_2 + D_1D_2 - D_1C_1 \quad (2-27)$$

While,

$$D_1 C_1 = \frac{h_1}{\tan \gamma} \quad (2-28)$$

$$D_2 C_2 = \frac{h_2}{\tan \gamma} \quad (2-29)$$

Then,

$$x = \frac{h_2 - h_1}{\tan \gamma} + \frac{h_2 - h_1}{\tan \beta} \quad (2-30)$$

The height difference between point B_1 and point B_2 can be expressed by the equation about x ,

$$h_2 - h_1 = \frac{x}{\frac{1}{\tan \gamma} + \frac{1}{\tan \beta}} \quad (2-31)$$

According the Equation (2-23), the height difference between point B_1 and point B_2 can also be expressed by the equation about λ ,

$$h_2 - h_1 = \frac{\lambda \cdot \sin \gamma}{1 + \sin \alpha \cdot (\sin \gamma - \cos \gamma)} \quad (2-32)$$

Combine the Equations (2-31) and (2-32), and we can get the relation about x and λ ,

$$\frac{x}{\frac{1}{\tan \gamma} + \frac{1}{\tan \beta}} = \frac{\lambda \cdot \sin \gamma}{1 + \sin \alpha \cdot (\sin \gamma - \cos \gamma)} \quad (2-33)$$

Simplify Equation (2-33), and we can finally get the equation for x with λ and contact angle β ,

$$x = \frac{\lambda \cdot \cos \gamma \cdot (\tan \beta + \tan \gamma)}{\{1 + \sin \alpha \cdot (\sin \gamma - \cos \gamma)\} \cdot \tan \beta} \quad (2-34)$$

When using the measured value of x to calculate β , convergence calculation is performed by using Equation (2-34) with a calculation accuracy of 1/1000 of x , and then contact angle β can be obtained.

2.2.3 Calculation of liquid surface profile

Generally, when calculating the contact angle of a liquid, the gas-liquid interface located near the contact line can be regarded as a plane due to the superhydrophilic condition. Therefore, the contact angle can be calculated by using Equation (2 – 34).

However, when calculating the surface profile of the liquid film, the surface profile can no longer be seen as a plane, as shown in Figure 2.6 Light E_1 and light E_2 are parallel coherent light, thus, $\angle B_1A_1C_1$ equals $\angle B_2A_2C_2$. The tangent line at point B_1 is B_1O_1 and the tangent line at point B_2 is B_2O_2 , and the inclination angles are β_1 and β_2 , respectively. The angle between the reflected light B_2C_2 and substrate OC_2 is γ_2 . At this moment, if the angle β_1 and the height h_1 of the point B_1 are used to calculate the height h_2 of point B_2 , the calculated height will be the height of B'_2 . As shown in Figure 2.6, the point B'_2 is higher than point B_2 . If the subsequent points are also calculated accordingly, the final calculated result is bound to a large error. To reduce this cumulative error, we connect points B_1 and B_2 to form a line segment B_1B_2 . B_1O is its extension line, and angle β_{12} is its inclination angle. If it is assumed that the curve between point B_1 and point B_2 is part of a circle, then β_{12} can be represented by β_1 and β_2 . Similarly, the inclination angles of the next segments can be obtained by the same method. With these corrected

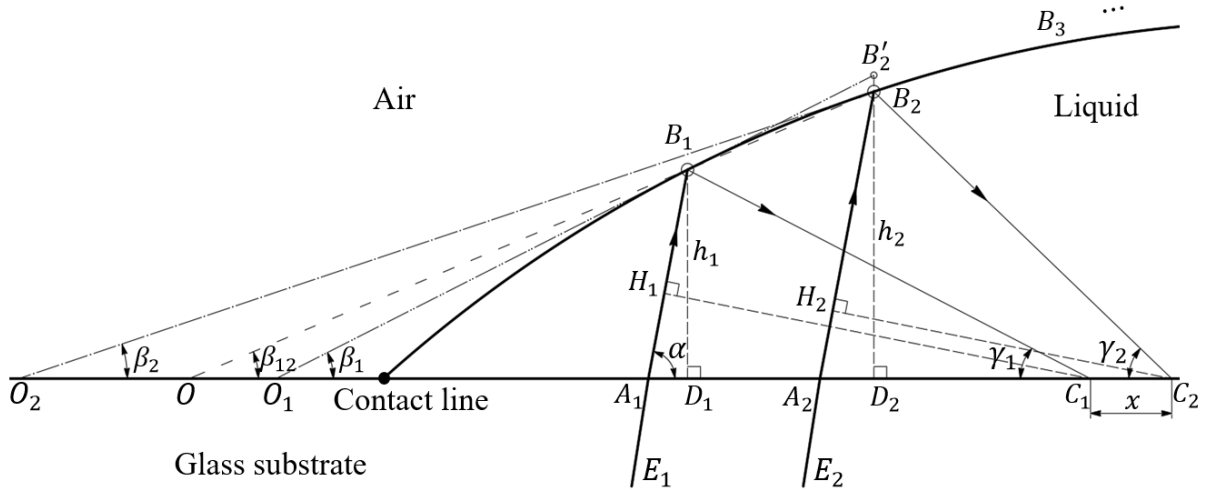


Figure 2.6 Image of the surface profile of a liquid film. Long dash-double dotted line B_1O_1 is a tangent line passing through point B_1 , long dash-dotted line B_2O_2 is a tangent line passing through point B_2 , and the corresponding inclination angles of these two lines are β_1 and β_2 . And β_{12} is the inclination angle of line B_1B_2 . The surface profile of the liquid is composed of line segments such as B_1B_2 and B_2B_3 . The height of point B_1 relative to the liquid-glass substrate interface is h_1 , and similarly, the height of B_2 is h_2 .

inclination angles, the horizontal and vertical positions of the reflection points at the air-liquid interface can be calculated.

α and γ_1 are the angles between the light E_1 and the liquid-glass substrate interface, γ_2 is the angle between the light E_2 and the liquid-glass substrate interface. Since lights E_1 and E_2 are coherent parallel lights, $\angle B_2A_2C_2$ is equal to angle α . The meanings of x and λ are the same as in section 2.2.2.

The specific calculation process about inclination angle in curve surface are as follows: First, the optical path difference at the interference points C_1 and C_2 are L_1 and L_2 . And,

$$L_1 = H_1B_1 + B_1C_1$$

$$L_2 = H_2B_2 + B_2C_2$$

As the same with Equations (2 – 15) ~ (2 – 22), the

$$\begin{aligned} \lambda &= L_2 - L_1 \\ &= A_2B_2 + B_2C_2 - A_2H_2 - (A_1B_1 + B_1C_1 - A_1H_1) \\ &= h_2 \left(\sin \alpha + \frac{1}{\sin \gamma_2} - \cot \gamma_2 \cos \alpha \right) - h_1 \left(\sin \alpha + \frac{1}{\sin \gamma_1} - \cot \gamma_1 \cos \alpha \right) \quad (2 - 35) \end{aligned}$$

According the assume that the curve between point B_1 and point B_2 is part of a circle,

$$\beta_{12} = \beta_1 - \frac{\beta_1 - \beta_2}{2} = \frac{\beta_1 + \beta_2}{2}$$

Similar to the Equations (2 – 24) ~ (2 – 27),

$$OD_1 = \frac{h_1}{\tan \beta_{12}}$$

$$OD_2 = \frac{h_2}{\tan \beta_{12}}$$

$$D_1D_2 = \frac{h_2 - h_1}{\tan \beta_{12}}$$

According to Equations (2 – 28) and (2 – 29),

$$D_1C_1 = \frac{h_1}{\tan \gamma_1}$$

$$D_2C_2 = \frac{h_2}{\tan \gamma_2}$$

Thus,

$$\begin{aligned} x &= D_2C_2 + D_1D_2 - D_1C_1 \\ &= h_2 \cot \gamma_2 + (h_2 - h_1) \cot \beta_{12} - h_1 \cot \gamma_1 \quad (2 - 36) \end{aligned}$$

Here the γ_1 and γ_2 can be represented by α , β_1 and β_2 :

$$\gamma_1 = \alpha - 2\beta_1$$

$$\gamma_2 = \alpha - 2\beta_2$$

In the Equation (2 – 35), h_1 can be calculated by the condition of the optical path difference $L = \lambda$. With Equation (2 – 34) and Equation (2 – 35), h_2 can be represented by x , h_1 and β_{12} :

$$h_2 = \frac{x + h_1 \cot \gamma_1 + h_1 \cot \beta_{12}}{\cot \beta_{12} + \cot \gamma_2} \quad (2 - 37)$$

In Equation (2 – 37), except h_2 , only β_{12} is unknown. Next, with Equation (2 – 35) and Equation (2 – 36), an equation about β_{12} and x can be derived:

$$x = \frac{\left\{ h_1 \left(\sin \alpha + \frac{1}{\sin \gamma_1} - \cot \gamma_1 \cos \alpha \right) + \lambda \right\} (\cot \beta_{12} + \cot \gamma_2)}{\left(\sin \alpha + \frac{1}{\sin \gamma_2} - \cot \gamma_2 \cos \alpha \right) (h_1 \cot \beta_{12} + h_1 \cot \gamma_1)} \quad (2 - 38)$$

In Equation (2 – 38), the β_{12} cannot be calculated directly. Therefore, as the same with Equation (2 – 34), a convergence calculation is performed by using Equation (2 – 38) with a calculation accuracy of 1/1000 of x . The angles for next segments can be obtained in the same manner. Then all the horizontal and vertical positions of the reflection points can be calculated.

2.2.4 Total reflection method

When light travels from media 1 to media 2, if it has different velocities in the two media, then the ratio of phase velocities in the two media is equal to the refractive index ratio of the two media. According to Snell's law, the ratio of phase velocities in the two media is also equal to ratio of sine of incidence angle θ_i in media 1 and sine of refraction angle θ_r in media 2 [4]. That is as follows:

$$\frac{v_1}{v_2} = \frac{n_2}{n_1} = \frac{\sin \theta_i}{\sin \theta_r} \quad (2 - 39)$$

From Equation (2 – 39), it is easy to know that when the refractive index n_1 of the media 1 is greater than the refractive index n_2 of the media 2, the incidence angle θ_i is smaller than the refraction angle θ_r .

Figure 2.7 shows the light propagating from the glass to the air at different incidence angle θ_i . Since the refractive index n_g of glass is greater than the refractive index n_a of air, the incidence angle θ_i is smaller than the refraction angle θ_r . When incidence angle θ_i gradually increases from 0° , refracted light and reflected light appear. When incidence angle θ_i changes to $\sin^{-1}(n_a/n_g)$, as shown in Figure 2.7 ③, the refracted light is parallel to the air-glass interface. The incidence angle θ_i at this moment is called the critical angle θ_c .

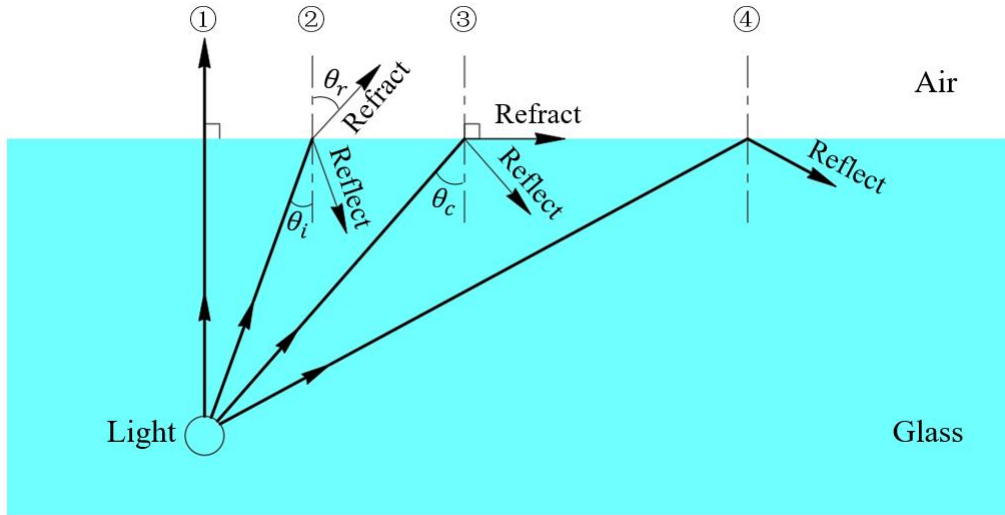


Figure 2.7 Image of light propagating from the glass to the air at different incidence angle. In the figure, ① is when incidence angle θ_i is 0° , and at this moment θ_i equals θ_r . ② is when incidence angle $0^\circ < \theta_i < \theta_c$, and the refracted light and reflected light exist. ③ is when incidence angle θ_i equals θ_c , and refracted light is parallel to the air-glass interface. ④ is the case of total reflection when the incident angle θ_i is greater than θ_c .

of total reflection. When the incidence angle θ_i is greater than the critical angle θ_c , as shown in Figure 2.7 ④, only reflected light exists and no refracted light appears.

However, when there are two media with different refractive indexes on the glass surface, as shown in Figure 2.8, there will be two critical angles of total reflection. n_l is the refractive index of the liquid. If there is a relationship: $n_a < n_l < n_g$, then, the critical angle θ_{cl} of total reflection between liquid and glass equals $\sin^{-1}(n_l/n_g)$. Therefore, $\theta_c < \theta_{cl}$.

So that, there is an angular range: $\theta_c < \theta_i < \theta_{cl}$, in which the incidence angle yields total reflection at solid-gas interface and partial reflection at solid-liquid interface, and by this way, the wetting and non-wetting area can be distinguished clearly. Hence, the contact line can be determined by this total reflection method.

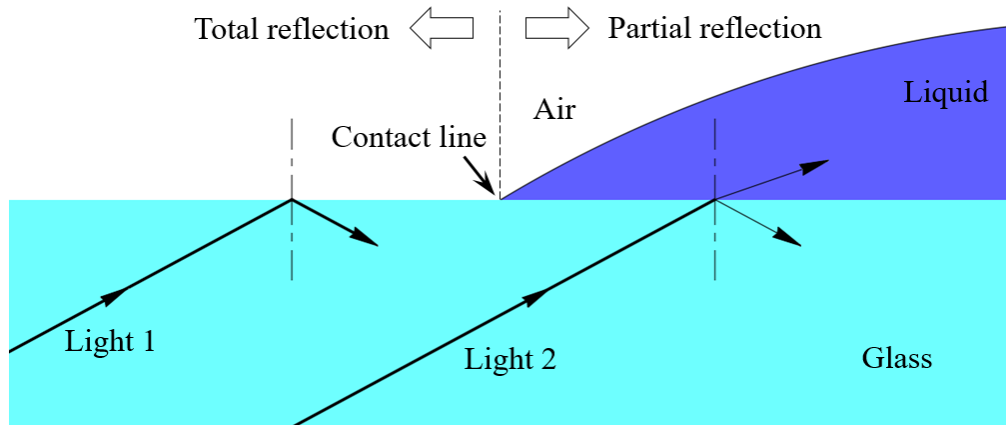


Figure 2.8 Image of two lights propagate from the glass to the air and liquid in an incidence angle θ_i , and $\theta_c < \theta_i < \theta_{cl}$. The contact line is the dividing line, the gas-glass interface is totally reflection, and the liquid-glass interface is partially reflection.

2.3 Verification experiment

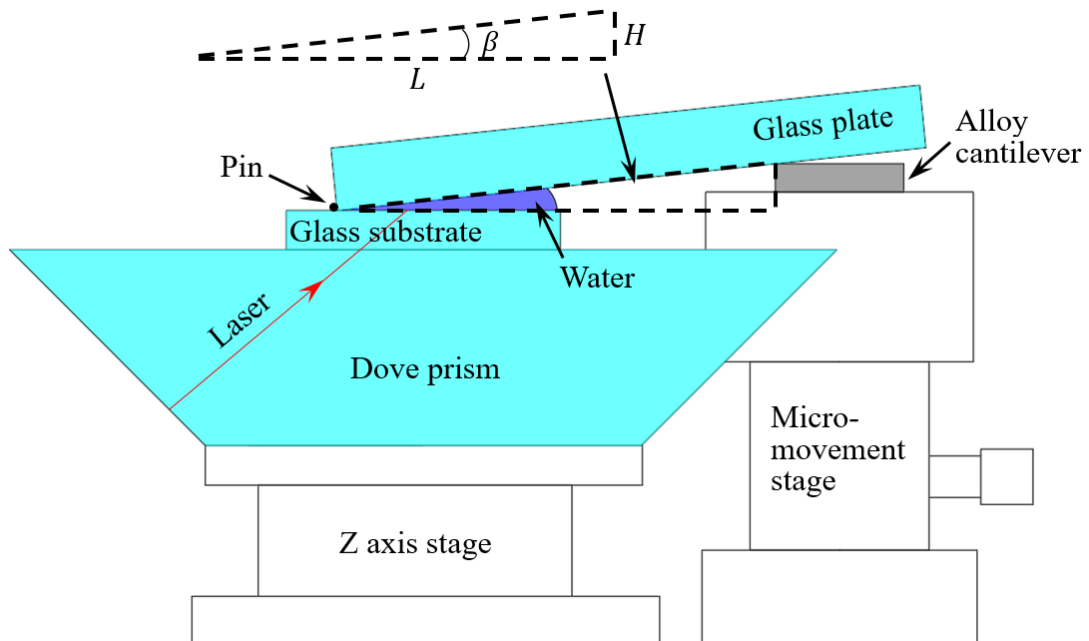
2.3.1 Outline of this section

In section 2.2, the equation for calculating the contact angle by using interference fringes and the equation for calculating the surface profile of the liquid are derived. But the correctness of the equations need to be verified by experiment. In this section, two sets of experiments are conducted to verify the two equations.

2.3.2 Verification experiment of equation for contact angle

(I) Facilities and materials

In order to verify the correctness of Equation (2 – 32), a verification experiment was performed. The schematic diagram of verification experiment apparatus is shown in Figure 2.9. A glass substrate (MATSUNAMI MAS-GP S9902) with surface roughness $Ra = 0.006\mu\text{m}$ is set on the dove prism (Thorlabs PS995 N-BK7). To eliminate the effect of the gap between the glass substrate and the dove prism, the gap is filled with cedar oil (FUJIFILM Wako chemicals 8000-27-9), which has an almost same refractive index with



contact angle. The micro-movement stage controls the inclination angle of the glass plate. The wedge region formed by the glass plate and the glass substrate is filled with water. Laser is irradiated from the lower left of dove prism, and the camera is placed on the lower right of the dove prism.

glass [5]. In this experiment, contact angle β equals the angle of inclination of the glass plate. The length of horizontal side of contact angle β is L and the length of vertical side which opposites to contact angle β is H . Contact angle β can be calculated with L and H easily by using inverse trigonometric functions. The glass plate is used as the hypotenuse of a triangle, and metal alloy cantilever is used to up and down along the vertical line to tilt the glass plate. To prevent the glass plate from sliding, a pin is placed at the contact point between the glass plate and the glass substrate. Water is injected between the glass plate and the glass substrate. The glass substrate was placed on the dove prism so that the angle could be changed from 0° .

In order to control the contact angle β , a micro-movement stage (Sigmakoki TSD-603) with an adjustment knob is used. When the knob rotates one turn, it moves up or down by 0.5 mm. There are 50 marks on one turn of the knob, and two rounds are 1 mm, hence, the adjustment accuracy of the stage is under 0.01 mm.

When the wedge formed by the glass plate and the glass substrate faces the opposite direction of laser incidence, as shown in Figure 2.9, here we call it a positive angle. On the contrary, when the wedge faces the direction of laser incidence, the angle is a negative angle.

(II) Results

Turn the knob to make the metal alloy cantilever rise at 0.05mm every time. During this process, images of fringes are taken by the camera. When the contact angle was positive and negative, the experiment was performed 4 times respectively.

Figure 2.10 (b) to (g) show the interference images when the angle changes from 0.16° to 2.64° in positive. From these interference images, it can be easily seen that as the angle becomes larger, the spacing of the interference fringes becomes narrower. When the angle gradually becomes greater than 2.64° , the interference fringes gradually become indistinguishable for the naked eye. When the angle exceeds 3° , with the current method, it is no longer possible to accurately distinguish the interference fringes.

Similar to Figure 2.10, Figure 2.11 shows the interference images when the angle changes from 0.14° to 2.28° in negative. Since the principle of interference fringe formation for positive and negative angles is the same, the images have similar fringe patterns.

In order to measure the fringe spacing in the interference images, the position of each light and dark fringe needs to be determined. Figure 2.12 shows two examples of reading brightness of the interference fringe image when the angle β is 0.16° and 1.15° in positive. Because the surface of the glass plate is a plane, the inclination angles at all reflection points on the glass plate are the same. Therefore, the brightness of the interference images in Figure 2.12 have uniform period variations. By measuring the spacing between

two adjacent peaks (or valleys) in the brightness images in Figure 2.12, so that the x in Equation (2 – 34) can be measured. Furthermore, the contact angle β can also be calculated by the equation.

When reading the brightness along the green line, if the reading width is 2 pixels, as shown in Figure 2.13 (a), there is a lot of noise on the peak value of the read brightness. Adjust the reading width to 40 pixels, as shown by the black line in Figure 2.13 (b), which has much less noise than Figure 2.13 (a). However, it is still impossible to accurately determine the specific location of the brightness peak. In order to reduce noise, we choose to filter the data. We used a Butterworth filter. The red line in Figure 2.13 (b) is the data processed by the Butterworth filter. According to the processed graphics, we can quickly and accurately find the brightness peak value, thereby measuring the distance between adjacent fringes.

As mentioned before, the brightness of the interference images have uniform period variations, and in order to accurately measure the period variation, a Fourier transform program is used to read the frequency of light and dark brightness changes. Figure 2.14 shows the result of using that program to read the interference image when angle β is 0.16° . The frequency of the brightness change of the fringes is the frequency indicated by the highest point in the power-frequency diagram. By using the same method, the spacing of interference fringes in other angles can be calculated.

Figure 2.15 and Figure 2.14 show the four times verification experimental results when the angle is positive (the situation of contact angle β in Figure 2.10 (a)). All of the four results show almost the same, and all of them maintain a high consistency with the set angle. It can be seen from the four results of the experiments that:

First, Equation (2 – 34) can be used to the calculation of β when the contact angle β is positive.

Second, when the contact angle β is greater than 3° , the measurement cannot be performed because the interference fringes cannot be clearly distinguished. That is, the measurable range is $0^\circ < \beta < 3^\circ$.

However, when the angle is negative (the situation of contact angle β in Figure 2.11 (a)), four times' results are calculated by using Equation (2 – 34), and all of the four calculated results have similar values. Two of the calculated results are shown in Figure 2.17. the measured angles are very different from the set angles. From this result, it can be known that Equation (2 – 34) is not suitable for the calculation when the contact angle β is negative.

Therefore, the equation for calculating contact angle β when it is negative, needs to be derived. According to the schematic diagram of condition for generating interference fringes

and relationship between spacing of interference fringe and contact angle β when the contact angle β is negative, as shown in Figure 2.18, the principle of generating interference fringe is the same as when the contact angle β is positive, except that the relationship about α , β and γ changes. When contact angle β is positive, the relationship about α , β and γ can be expressed by Equation (2 – 12). When contact angle β is negative the three angle have relationship:

$$\gamma = \alpha + 2\beta \quad (2 - 40)$$

Finally, calculate according to the relationship shown in Figure 2.18, we can get the equation about x and β when the contact angle β is negative:

$$x = \frac{\lambda \cdot \cos \gamma \cdot (\tan \gamma - \tan \beta)}{\{1 + \sin \alpha \cdot (\sin \gamma - \cos \gamma)\} \cdot \tan \beta} \quad (2 - 41)$$

With Equation (2 – 41), when the contact angle is negative (the situation of contact angle β in Figure 2.11 (a)), four times' results are calculated, and the four calculated results are shown in Figure 2.19 and Figure 2.20. From the figures, all of the results have similar values, and the measured angles and the set angles have a good consistency.

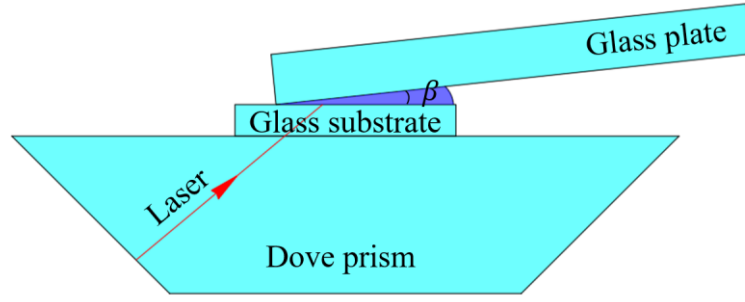
From the results when the contact angle is negative, the Equation (2 – 41) can be used to the calculation of contact angle β when the contact angle β is negative. As when the contact angle is positive, when the contact angle is greater than 3° in negative, the measurement cannot be accurately performed. The measurable range is also $0^\circ < \beta < 3^\circ$.

According the results of eight times' experiments, the minimum measurable angle is 0.007° . When the contact angle is between 0.5° and 3° , the error percentage is $\pm 6\%$. From 0.5° to 0.2° , there is a linear increase in the error percentage from $\pm 6\%$ to $\pm 10\%$. And the error percentage from 0.2° to 0.007° is $\pm 10\%$.

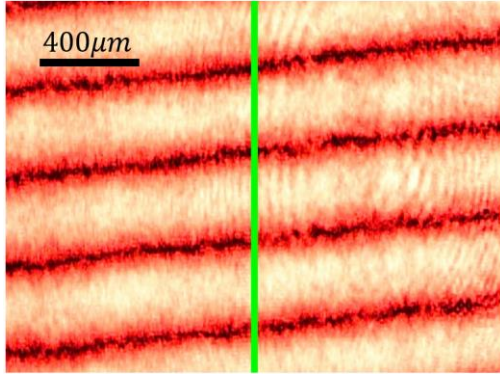
In theory, as long as there is a light reflected from the gas-liquid interface to the observed area on the solid-liquid interface, interference fringes may appear. But in fact, due to the loss of the reflected energy of light and the scattering effect of the liquid on the light, when the liquid film is thick, the reflected light will become weaker, making the interference insignificant and thus the fringes unable to be observed. The thickest liquid film measured in this verification experiment is 3.04mm.

The maximum measurable angle obtained in this verification experiment is 3° . In theory, the angle can be measured as long as the light is reflected from the gas-liquid interface to the observed area on the solid-liquid interface and forms interference fringes. As shown in Figure 2.4, the reflected light BC needs to intersect the liquid-glass substrate interface, and when the reflected light BC is parallel to the liquid-glass substrate interface, the inclination angle β_m is equal to half of the angle α . Therefore, the theoretically measurable angle limit is less than 0.5α . Reducing the incident angle θ_i can increase the maximum

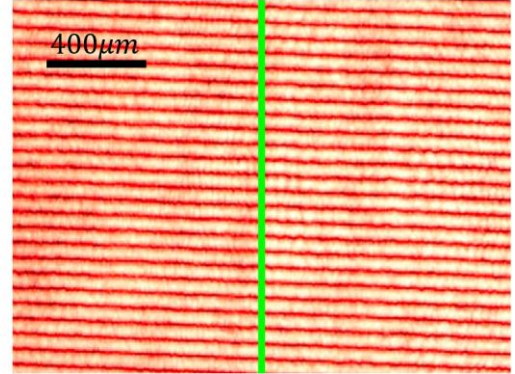
measurable angle β_m . When θ_i is equal to 0° , that is, when α is equal to 90° , β_m reaches the maximum.



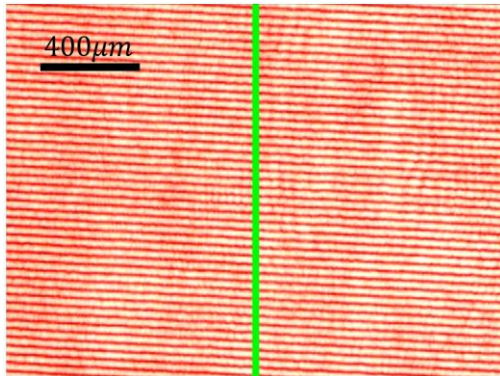
(a)



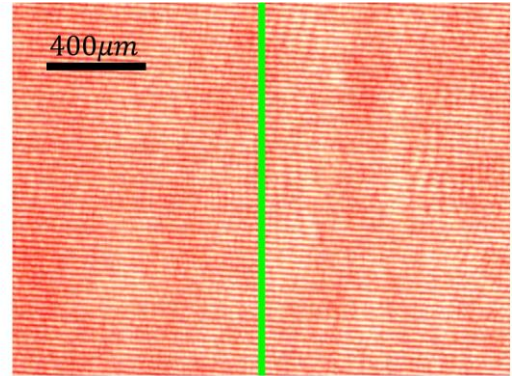
(b) $\beta = 0.16^\circ$



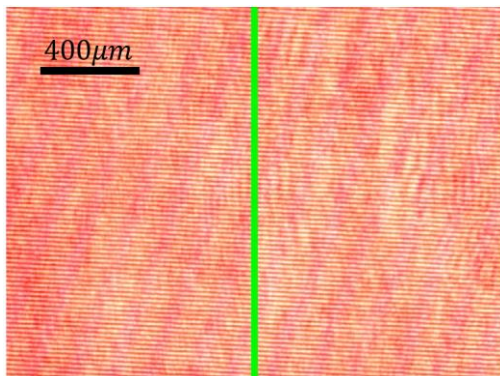
(c) $\beta = 0.66^\circ$



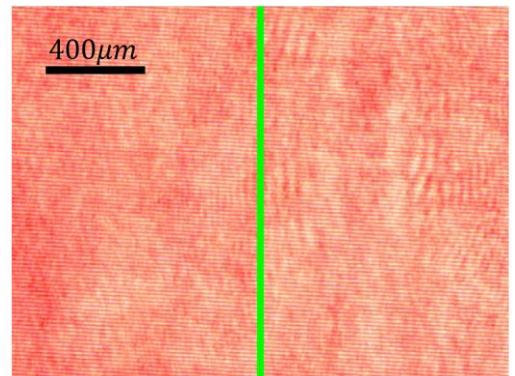
(d) $\beta = 1.15^\circ$



(e) $\beta = 1.65^\circ$

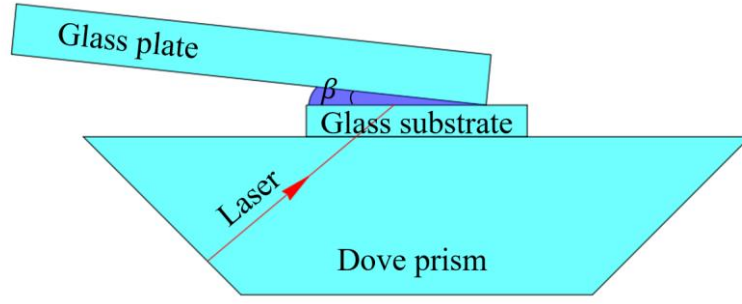


(f) $\beta = 2.14^\circ$

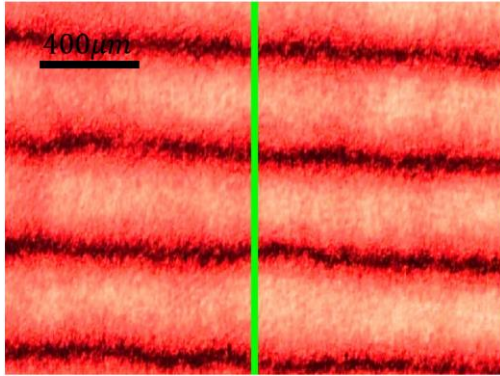


(g) $\beta = 2.64^\circ$

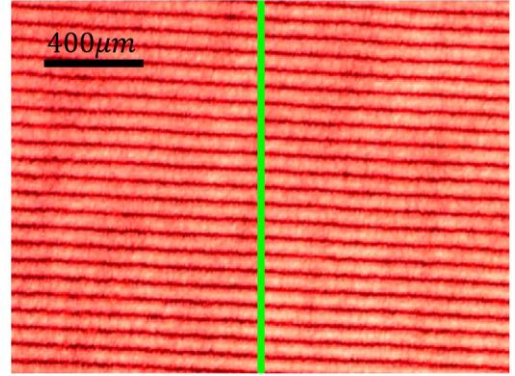
Figure 2.10 Interference images when the angle β changes from 0.16° to 2.64° in positive. The vertical green lines in the middle of the pictures indicate that the analysis is along this line.



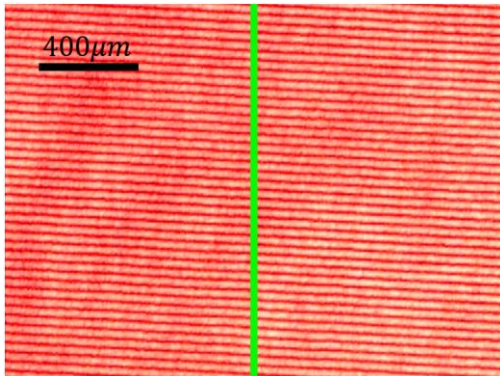
(a)



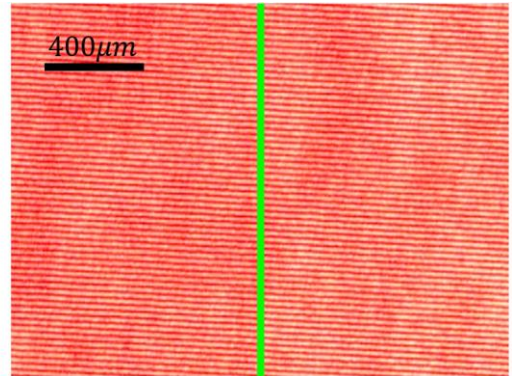
(b) $\beta = 0.14^\circ$



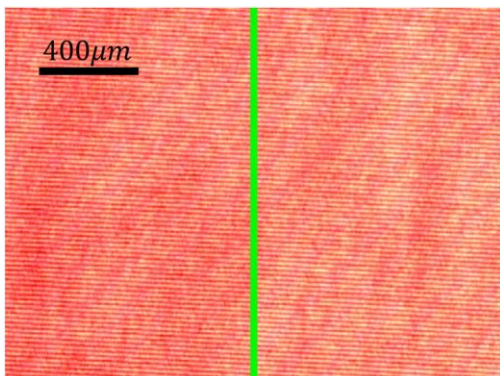
(c) $\beta = 0.57^\circ$



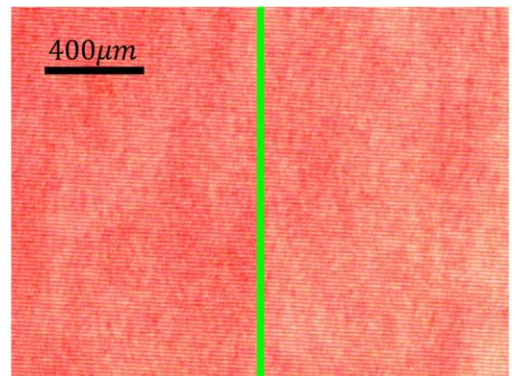
(d) $\beta = 1.00^\circ$



(e) $\beta = 1.43^\circ$

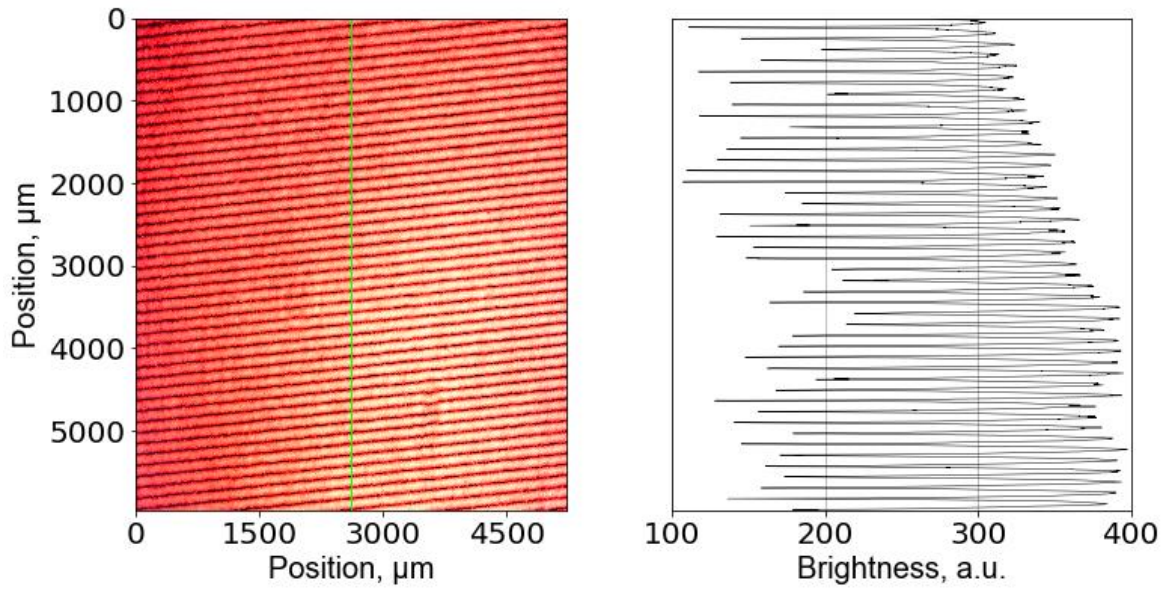


(f) $\beta = 1.86^\circ$

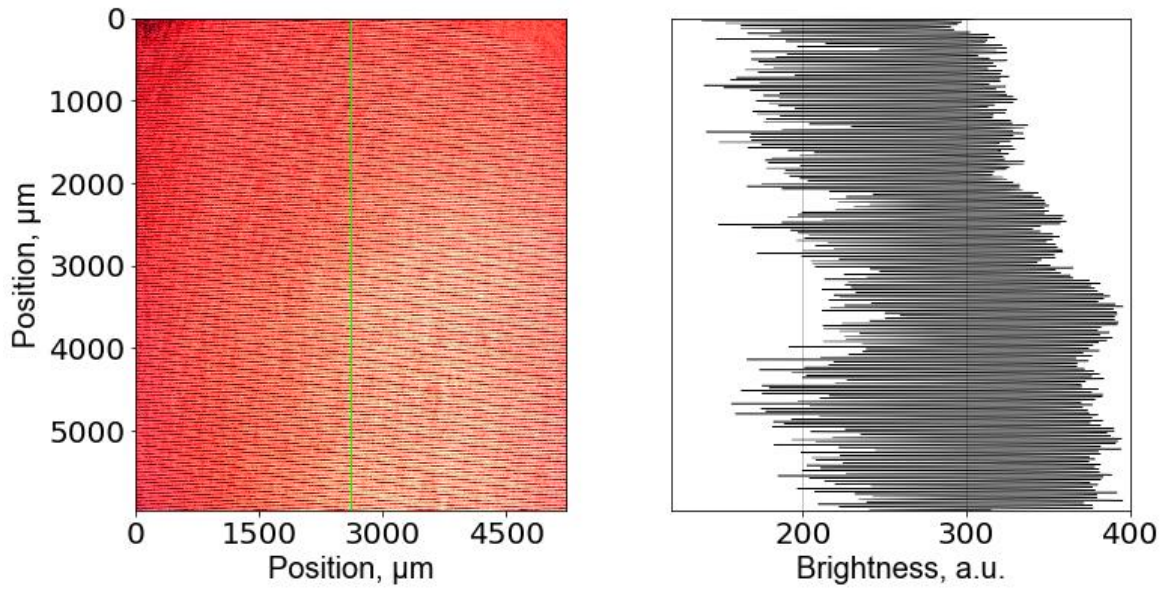


(g) $\beta = 2.28^\circ$

Figure 2.11 Interference images when the angle β changes from 0.14° to 2.28° in negative.



(a) $\beta = 0.16^\circ$



(b) $\beta = 1.15^\circ$

Figure 2.12 Two examples of reading brightness of the interference fringe image when the angle β is 0.16° and 1.15° in positive.

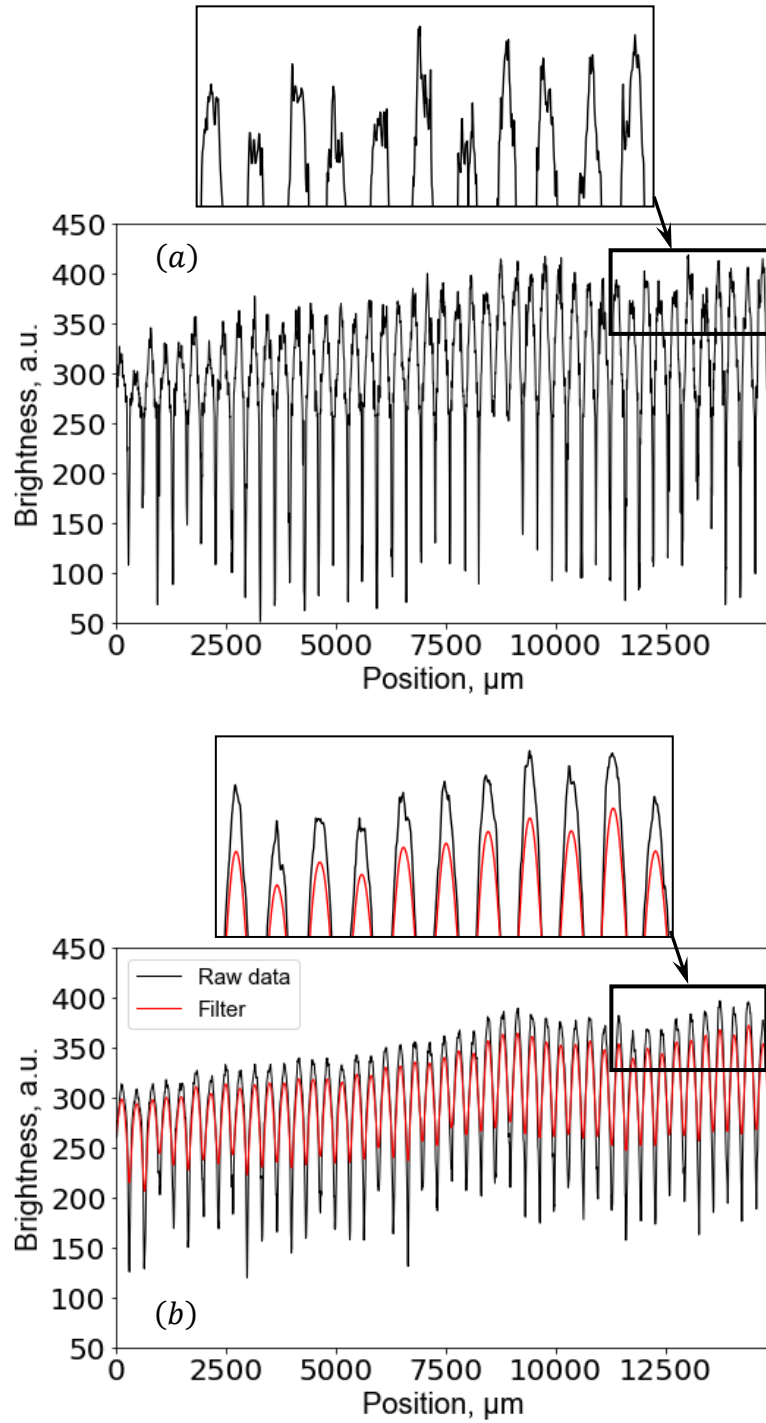


Figure 2.13 Brightness graph when $\beta = 0.16^\circ$. Figure 2.13 (a) is an image of the brightness graph analyzed with 2 pixels' width. We can see that there is a lot of noise on the peak brightness through the partial enlarged image. Figure 2.13(b) is the brightness graph analyzed with 40 pixels' width (black line) and filtered brightness graph (red line). From the partial enlarged image, we can see that the noise read out at 40 pixels' width at the peak brightness is much less, and there is no noise in the filtered graph.

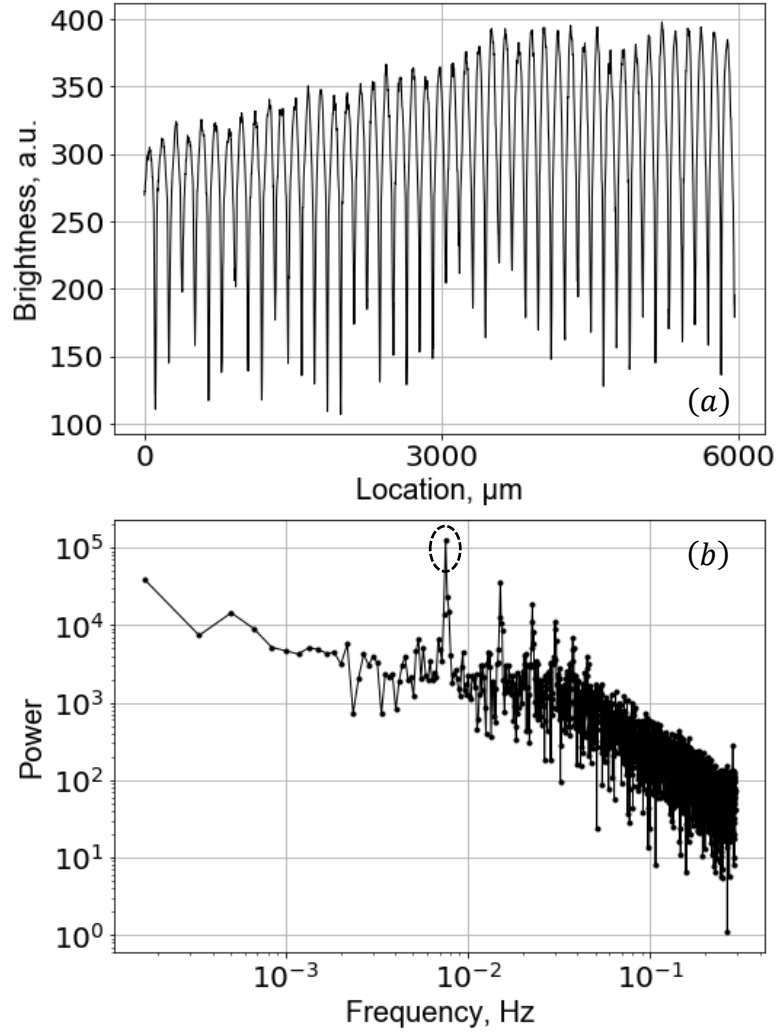


Figure 2.14 Image of using the Fourier transform program to read the frequency of light and dark brightness changes when β is 0.16° in positive. In the Figure 2.14 (b), the point encircled by black dots are the frequency of light and dark changes in the Figure 2.14 (a). From the frequency the period can be calculated, which is, the spacing between two adjacent dark fringes (bright fringes).

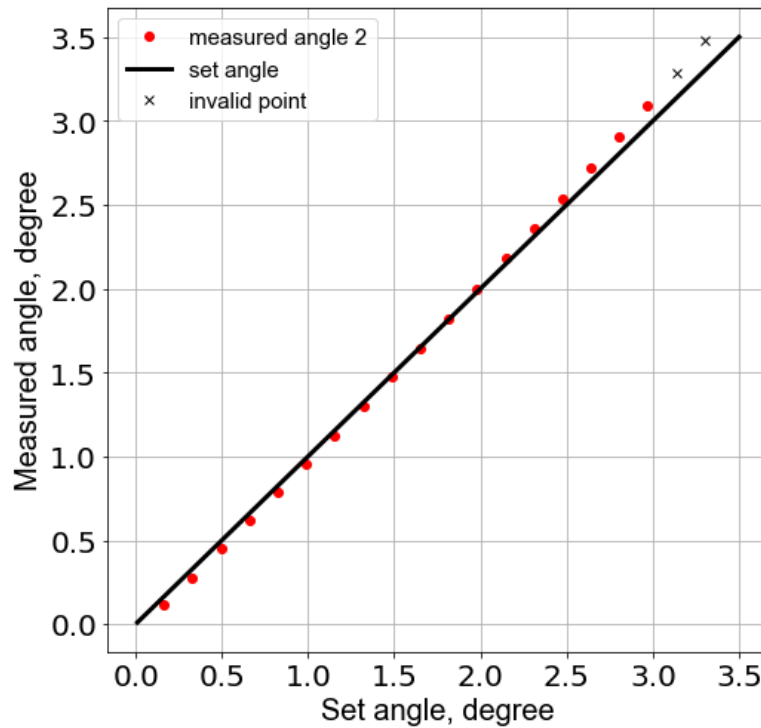
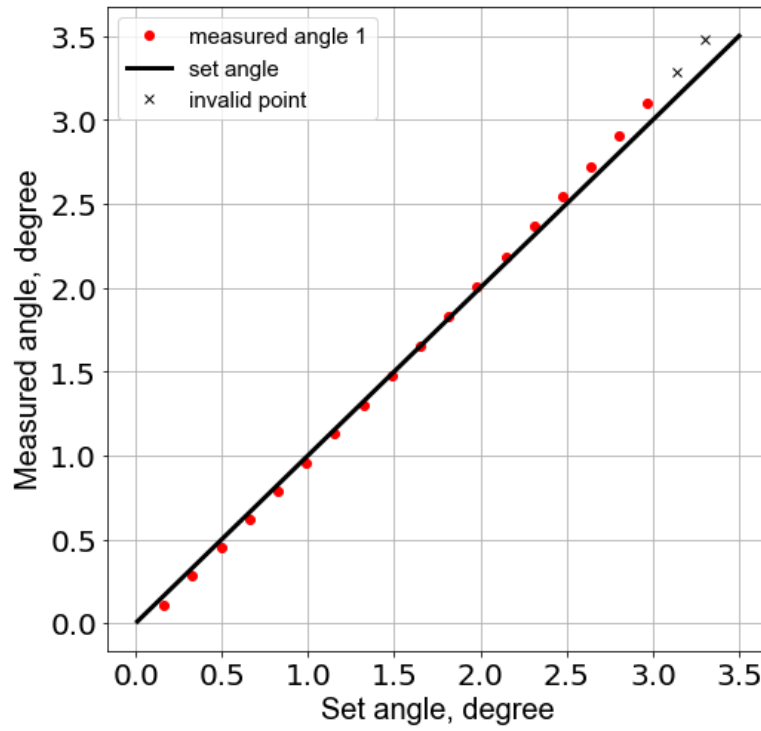


Figure 2.15 Results of No. 1 and No. 2 verification experiments when the angle is positive. In the figure, the red points indicate the measured angles, which are calculated based on the spacing of interference fringes with Equation (2 – 33). And the black line indicates the set angle.

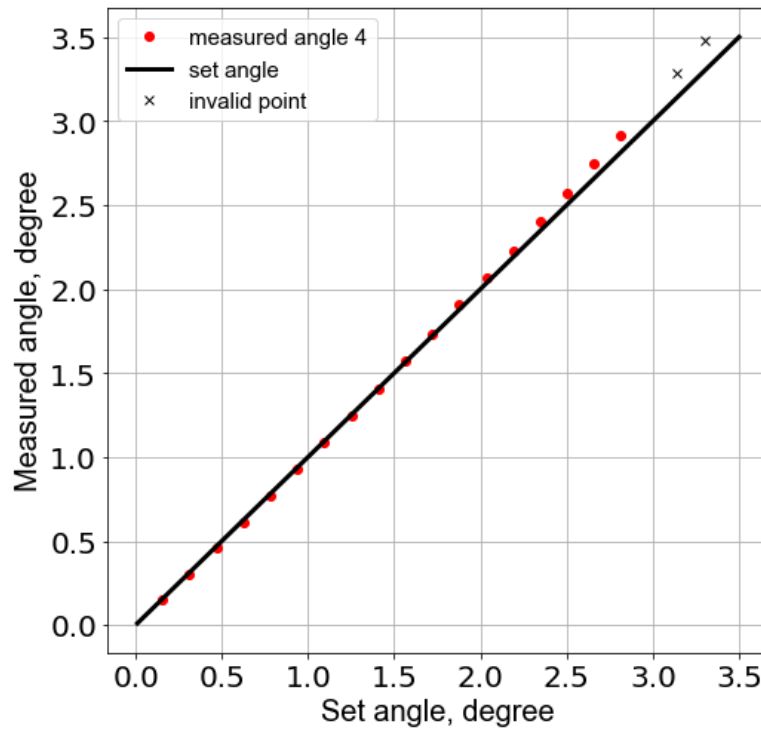
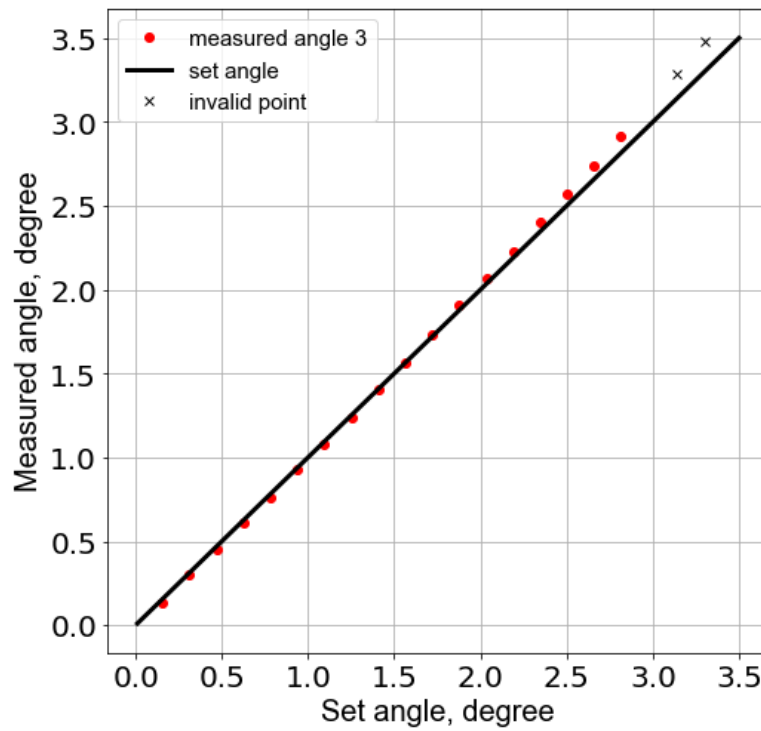


Figure 2.16 Results of No. 3 and No. 4 verification experiments when the angle is positive. Results of No. 3 and No. 4 show almost the same, both of them maintain a high consistency with the set angle.

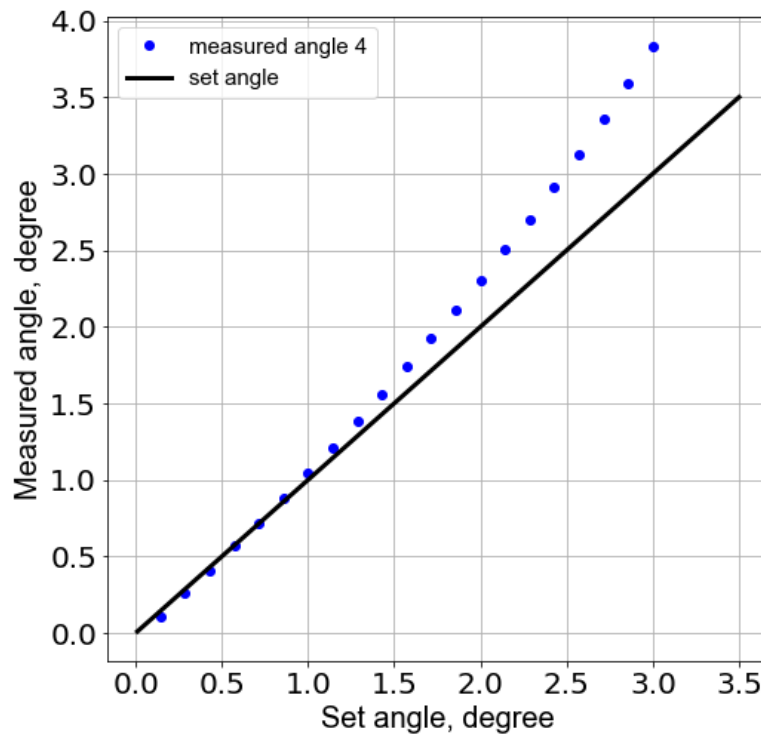
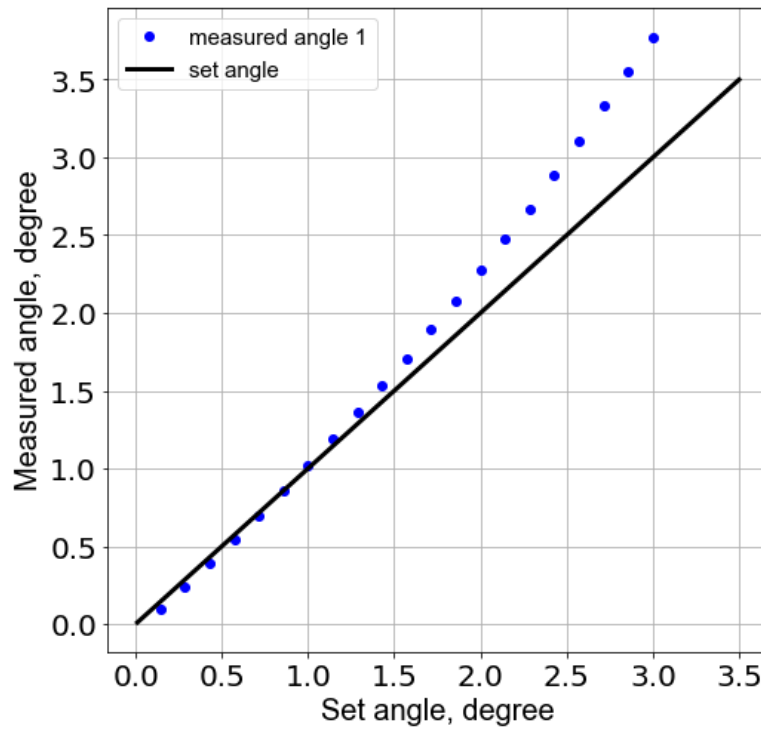


Figure 2.17 Results of No. 1 and No. 4 verification experiments when the angle is negative. The results are calculated with Equation (2 – 33). The results from No. 1 to No. 4 are almost the same, but they are very different from the set angles.

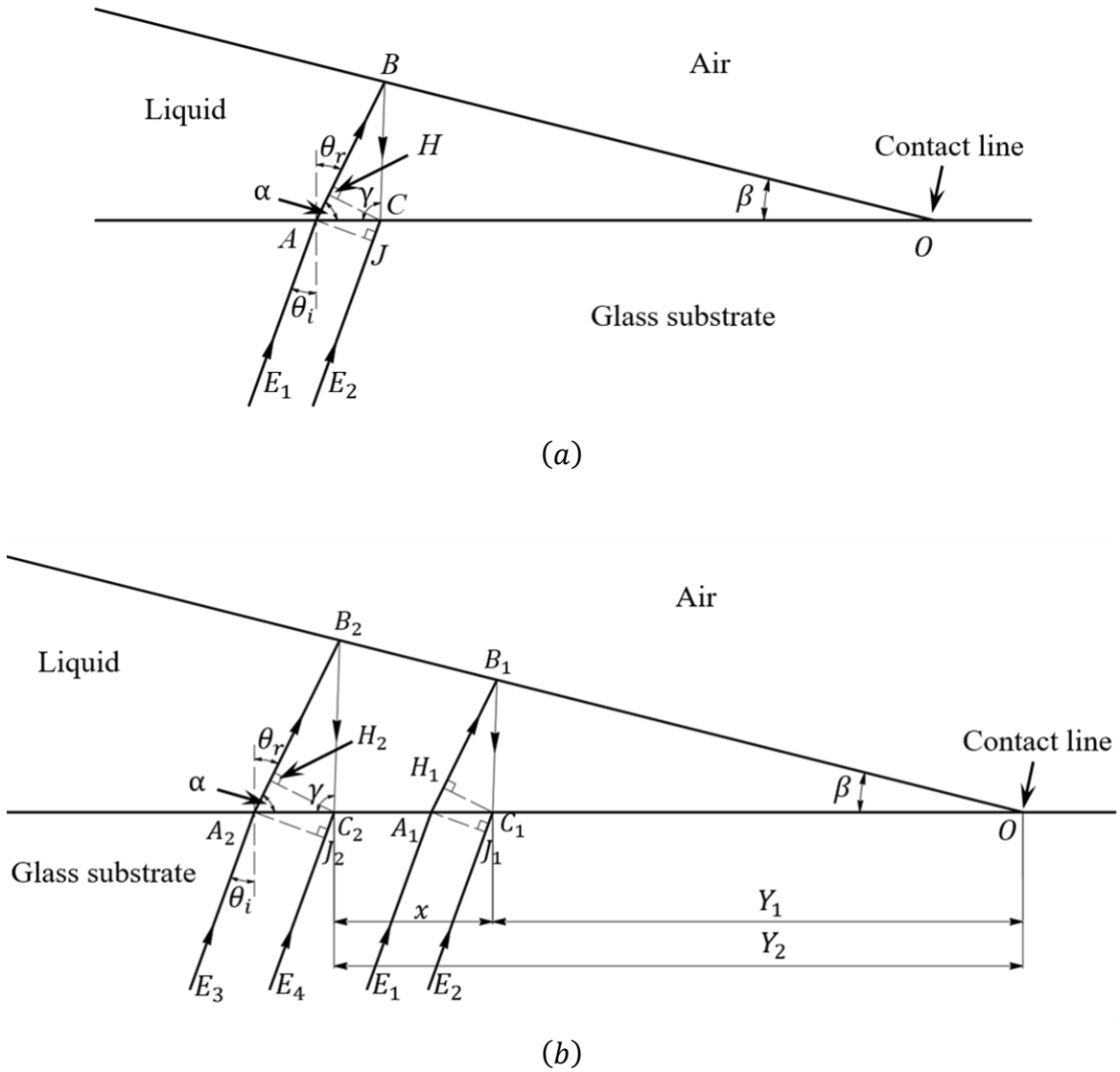


Figure 2.18 Schematic diagram of condition for generating interference fringes (shown in Figure 2.18 (a)) and relationship between spacing of interference fringe and contact angle β (shown in Figure 2.18 (b)) when the contact angle β is negative.

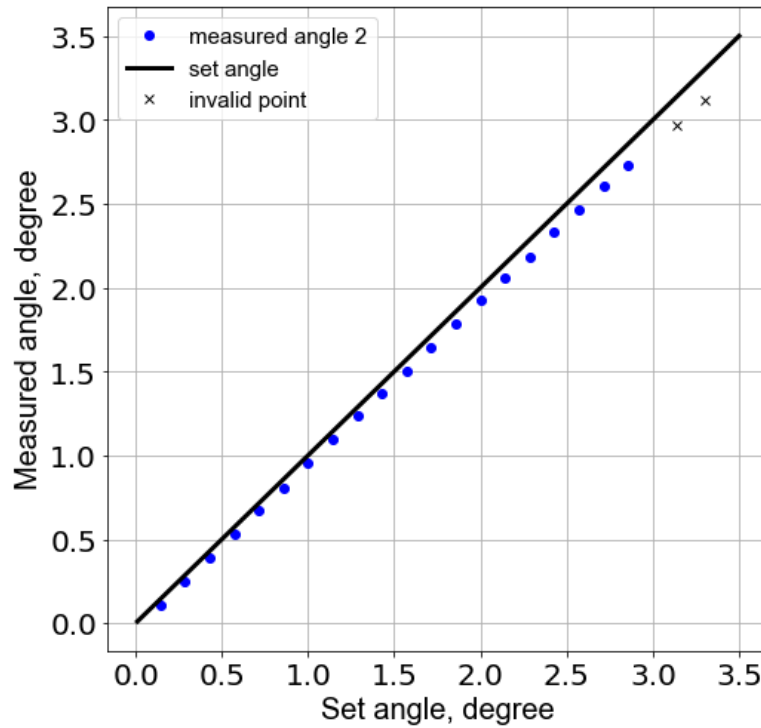
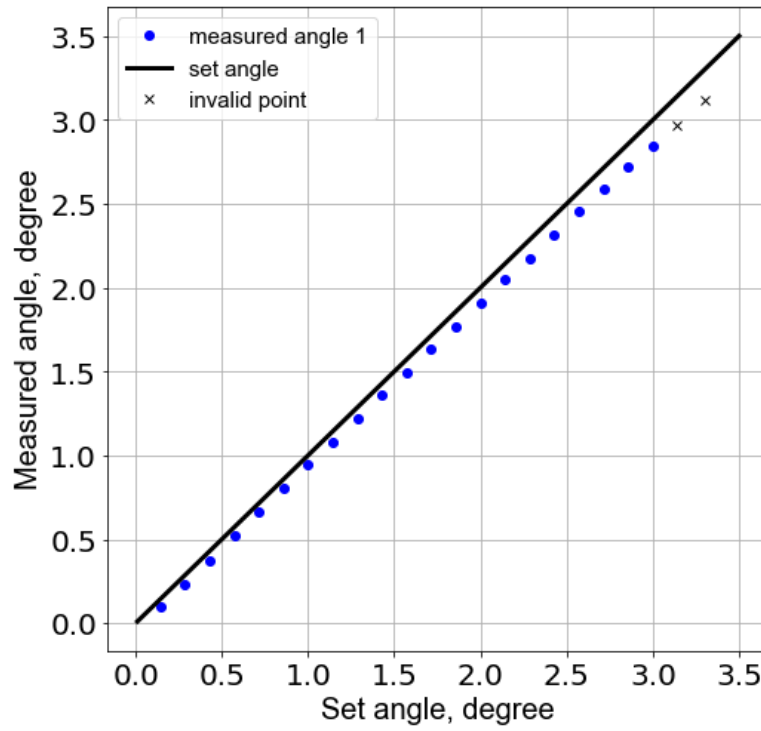


Figure 2.19 Results of No. 1 and No. 2 verification experiments when the angle is negative. In the figure, the blue points indicate the measured angles, which are calculated based on the spacing of interference fringes with Equation (2 – 39). And the black line indicates the set angle.

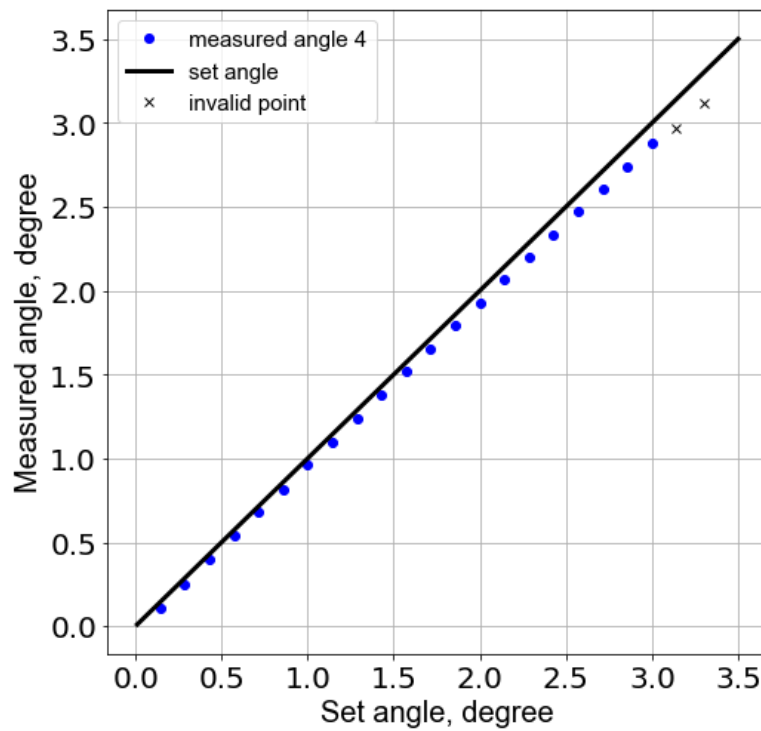
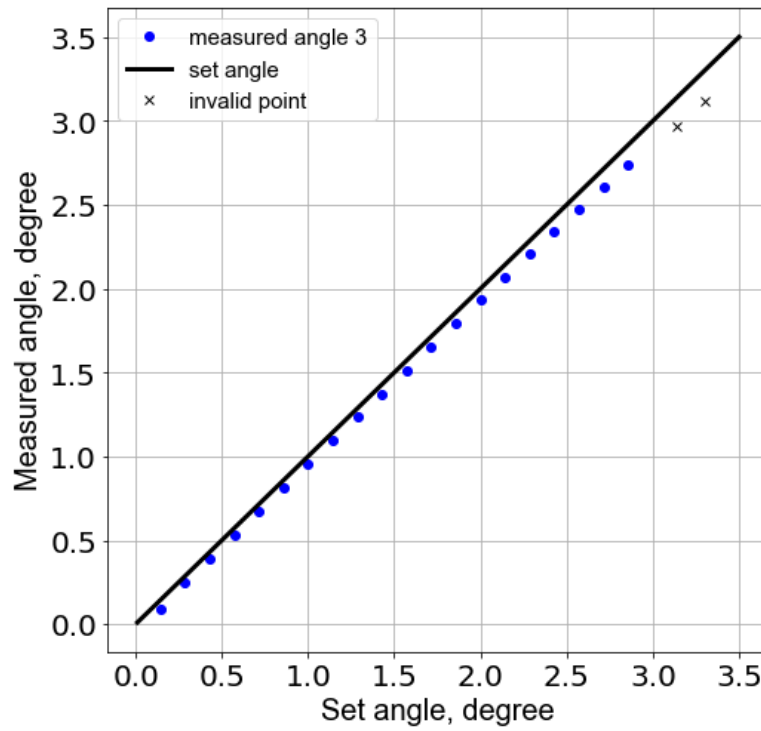


Figure 2.20 Results of No. 3 and No. 4 verification experiments when the angle is negative. Results of No. 3 and No. 4 show almost the same, both of them maintain a high consistency with the set angle.

2.3.3 Verification experiment of equation for calculating the surface profile of the liquid

In section 2.3.2, the Equations (2 – 34) and (2 – 41) for calculating the contact angle have been verified. The Equations (2 – 37) and (2 – 38) which are used to calculate the liquid surface profile also need to be verified.

Generally, the liquid surface is a continuous and smoothly changing curved surface. In order to facilitate comparison with the calculated value, in this verification experiment the lens with a spherical surface and known parameters is selected.

As shown in Figure 2.21 (a) is a part of the schematic diagram of the verification experimental facilities. Figure 2.21 (b) is an enlarged view of the part enclosed by the dotted line in Figure 2.21 (a). The lens (SIGMAKOKI Co., TLD SLB-07-50P) is placed on the glass substrate and the spherical portion of the lens is in contact with the glass substrate. The gap between the lens and the glass substrate is filled with water. The laser passes through the water and reflects to the water-lens interface, and then forms interference fringes at the water-glass substrate interface. Figure 2.21 (c) shows the image of interference fringes formed the lens. Due to the surface of lens is spherical surface, the interference fringes are some rings. The green horizontal line in the Figure 2.21 (c) indicates where the brightness of the interference fringes are read.

According the read brightness, the spacing of the light fringes (or dark fringes) can be measured. If we just use the equation that calculating for contact angle and profile of plane to calculate the surface profile of the lens, the measured profile will have big error with the real profile. For example, as shown in Figure 2.22 (a), the black line indicates the spherical profile of the lens and the red line with dot mark indicates the measured profile with Equations (2 – 34) and (2 – 41). Contrary to the situation of the assumed point B'_2 in Figure 2.6, in Figure 2.22 (a) the red line with dot mark is smaller than the black line. Thus, it is clear that Equations (2 – 34) and (2 – 41) are not available to calculate the curve.

Put the measured spacing into Equations (2 – 37) and (2 – 38), and we can get the reflection points at the spherical surface. Then the measured profile can be drawn. In Figure 2.22 (b) the red line with dot mark is calculated by Equations (2 – 37) and (2 – 38), it is clearly that the measured profile has a good consistency with the spherical profile of the lens. Thus, through this experiment, Equations (2 – 37) and (2 – 38) are proved that they can be used to calculate the surface profile of the curved surface.

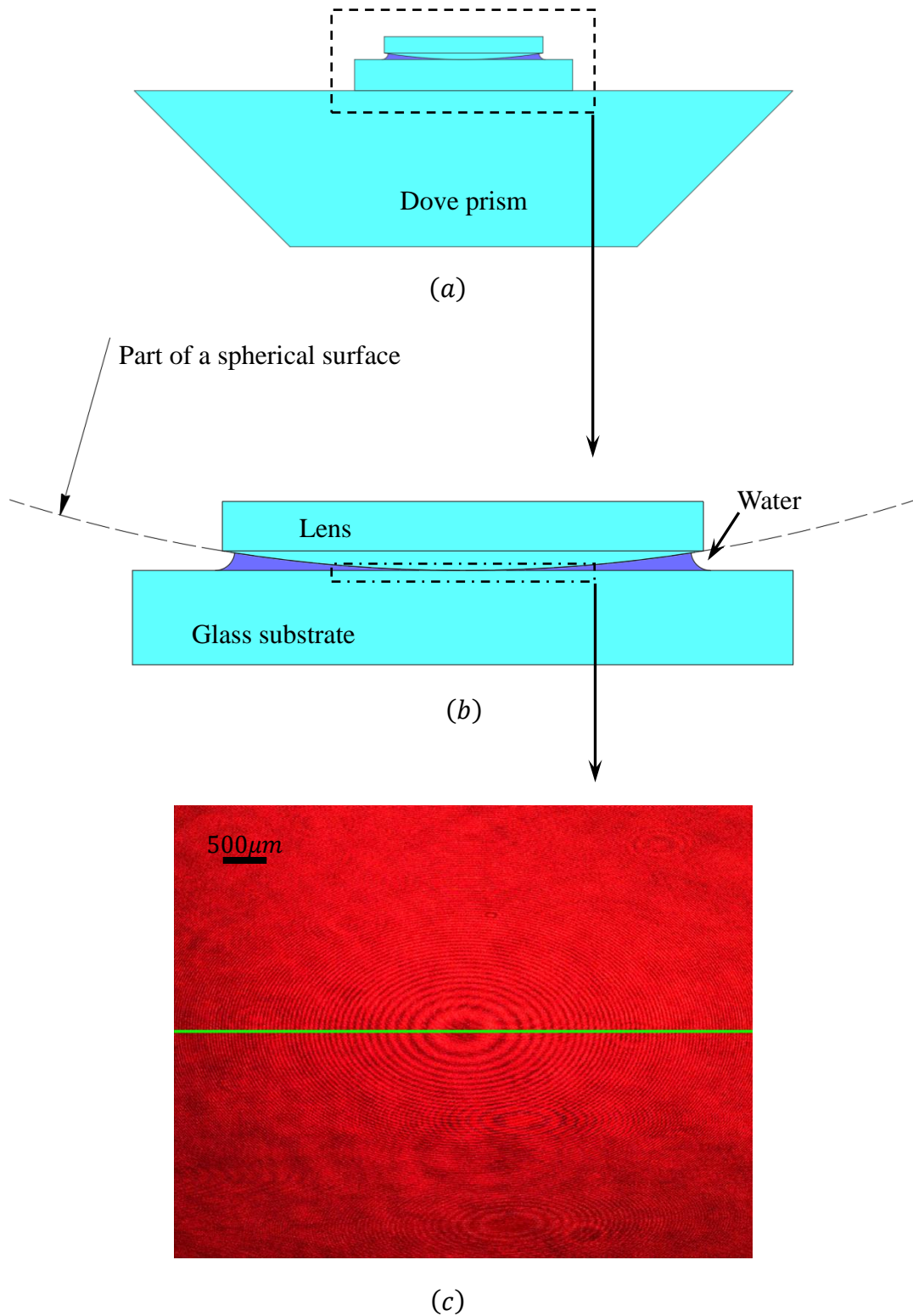
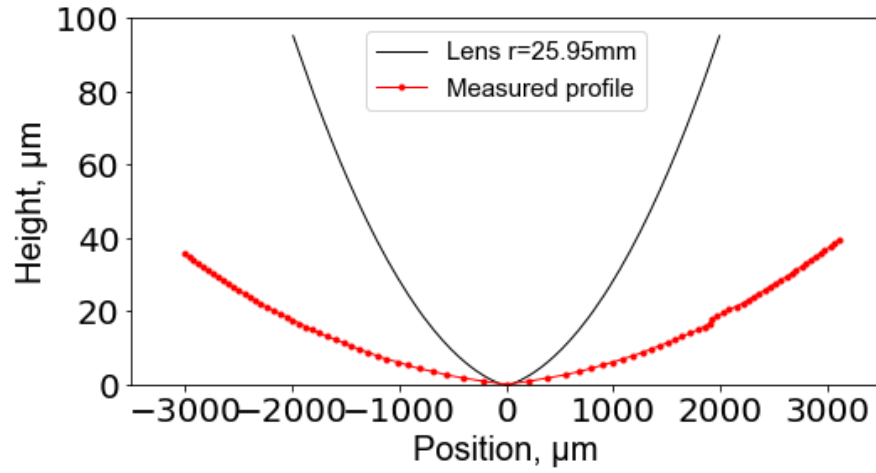
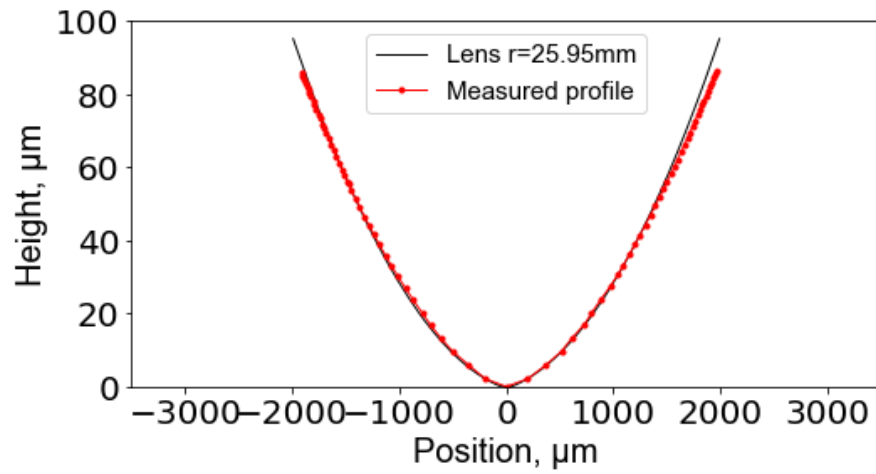


Figure 2.21 A part of the schematic diagram of the verification experimental facilities when the lens on the glass substrate. Figure 2.21 (c) is the image of interference fringes formed by the lens.



(a)



(b)

Figure 2.22 Spherical profile of the lens and measured profiles calculated by different equations. The measured profile in Figure 2.22 (a) is calculated by the Equations (2 – 34) and (2 – 41) and the measured profile in Figure 2.22 (b) is calculated by the Equations (2 – 37) and (2 – 38).

2.4 Wetting behavior of liquid on a super-hydrophilic surface

2.4.1 Experimental facilities and materials

In section 2.2 and section 2.3, the total reflection and interference fringe method used in this experiment has been introduced and verified. Observations about the wetting behavior of liquids on the super-hydrophilic surface will be performed in this section.

The features of light that easily cause interference fringes are that the spectrum width is short and the phase difference is stable. A typical example of a light source with a short spectral width is laser light. Among them, the He-Ne laser has good monochromaticity (short spectral width) and well-aligned phases, so that interference occurs easily. Therefore, in this research the laser is He-Ne laser (Thorlabs HNL100L-JP wavelength: 632.8nm).

It can be seen from Equation (2 – 34) that the wavelength of the laser is proportional to the spacing x of the interference fringes. When using a laser with a shorter wavelength, the minimum measurable angle will be smaller. But when the angle β becomes larger, because the wavelength is shorter, x becomes smaller, so that x reaches the limit that the

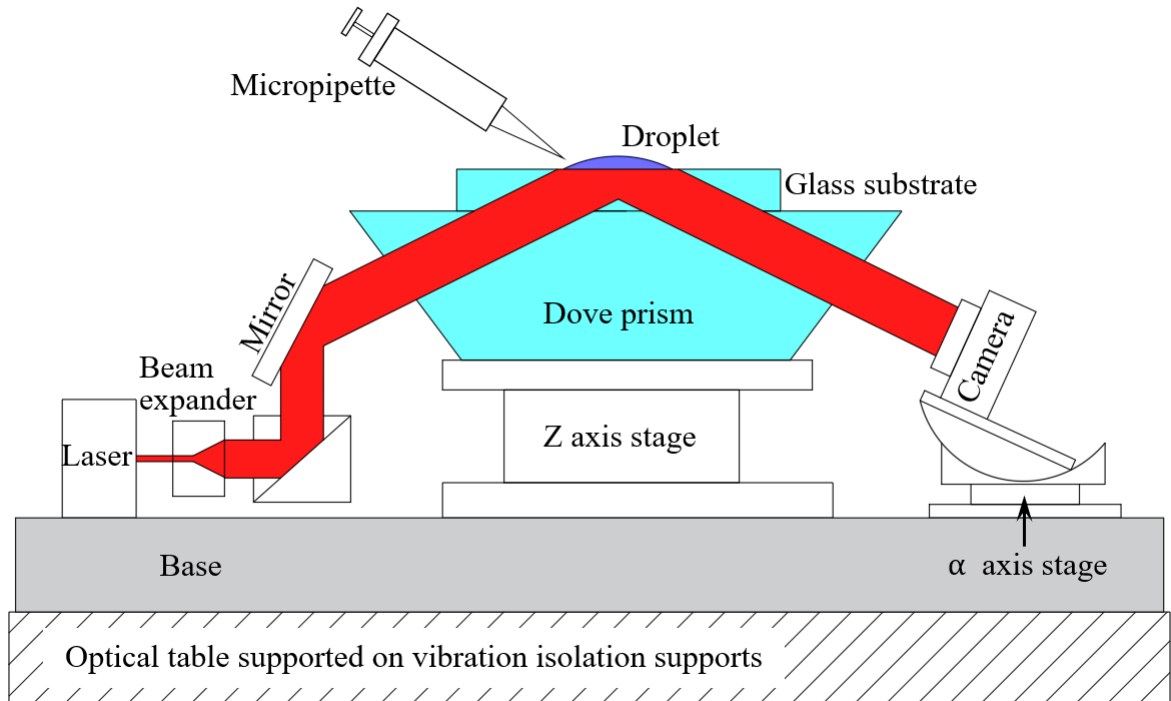


Figure 2.23 Schematic diagram of the experimental facilities for observing wetting behavior.

observation equipment can resolve earlier. Thereby the maximum measurable angle becomes smaller.

The schematic diagram of experimental facilities are shown in Figure 2.23. First, the laser passes through the beam expander, and the beam is converted from parallel light with a diameter of 0.68mm to parallel light with a diameter of 25.4 mm. The dove prism is fixed on the Z axis stage, so that it can be adjusted to a suitable height. The glass substrate placed on the dove prism is the same with the one in verification experiment in section 2.3. The expanded laser is reflected by the mirror and enters from oblique bottom of the dove prism. The incident angle of the laser is determined by the inclination angle of the mirror. And then the laser is reflected at the air-glass substrate interface where the total reflection and interference fringes occurs. In the reflection area, the droplet is placed by a micropipette (NICHIRYO Nichipet EX 0.5-10 μ L) and begins spreading behavior. In order to avoid the impact of the droplet colliding with the glass substrate on the wetting behavior when dripping the droplet from a high place, before squeezing out the droplet, the micropipette tip is brought into 1~2 mm with the glass substrate. The wetting behavior is observed by the camera (Nikon Nikon1V3 18.39million pixels, CMOS captures images in 24-bit RGB format with resolution 2.5 μ m/pixel). The inclination angle of the camera is controlled by the α axis stage. The facilities are fixed on the base, and in order to reduce the impact of external vibration, the base is placed on the vibration isolator.

In this experiment, 6 liquids are used, and they are ethanol (057-00456), octane (153-00065), decane (044-21605) from Wako Pure Chemical Industries, Ltd., silicone oil of 1 cSt and 10 cSt (Shin-Etsu Chemical Co., Ltd. KF-96L-1CS, KF-96L-10CS) and water (KOGA Chemical Mfg Co., Ltd. 05-232). Their parameters of surface tension and viscosity at 25°C are shown in Table 2.1 (These values are the data obtained from the product performance instructions of the respective manufacturers.).

Different liquids have different refractive indices. Considering the refractive index of all the liquids in the experiment, the incident angle θ_i is set between 50° and 58°, in which the reflection of non-wetting area is total reflection, and the reflection of wetting area is partial reflection. In this experiment, take a value close to the middle of the range, the incident angle θ_i is 53°.

The reason why several alkane hydrocarbons are used in this experiment instead of industrial lubricants is because there are many types of lubricants in actual industrial applications, with complex components and high viscosity, which are not conducive to initial research. Select single-component hydrocarbons with good fluidity for initial research. In the future, the established methods can be used to research specific industrial lubricants.

Table 2.1 Parameters (surface tension, viscosity and volume) of the 6 liquids.

	Surface tension σ mN/m	Viscosity η mPa · s	Volume V μ L
Octane	21.4	0.56	3
Octane	21.4	0.56	1
Decane	23.8	0.838	3
Decane	23.8	0.838	1
Ethanol	22.16	1.148	3
Silicone oil 1 cSt	16.9	1.222	1
Silicone oil 10 cSt	20.1	10.695	1
Water	72.28	0.936	5

2.4.2 Experimental procedure

(I) Spreading behavior

The first performed is to observe the free spreading after the droplet is placed on the glass substrate.

As shown in Figure 2.24, after the droplet squeezed out from the micropipette, the droplet spread freely like a round pancake onto the glass substrate. Due to the total reflection, the wetting area can be clearly observed, so that the dynamic change of the wetting radius R can be measured. At the same time, because of the camera recording, the spreading time t can also be synchronized with the radius R . Before each new experiment, the glass substrate is placed in an ethanol environment, and placed in an ultrasonic cleaner to clean for ten minutes and then placed in a drying cabinet for drying ten minutes at 70°C .

The alkanes (Octane and Decane), organic solvent (Ethanol) and Silicone oil 10cSt used in this experiment have similar surface tensions. As control experiments, Octane and Decane is taken $1\ \mu\text{L}$ and $3\ \mu\text{L}$, respectively, for the experiment. In addition, the Silicone oil of 1 cSt and 10 cSt with $1\ \mu\text{L}$, and water $5\ \mu\text{L}$ are taken for the control experiment.

When observing the spreading behavior, it mainly uses total reflection to make $R - t$ diagrams of the 6 liquids. And the factors affecting $R - t$ is analyzed. Experiments were performed under $20 \pm 0.5^{\circ}\text{C}$ room temperature and $50\% \pm 2\%$ of relative humidity. During the spreading process, the wetting radius is recorded by the camera with a frame rate of 30 f.p.s.. In the experiment, ethanol, which has the fastest spreading speed, the spreading speed is also less than $4.5\ \text{mm} \cdot \text{s}^{-1}$. The spreading time is greater than 10 s, and the spreading

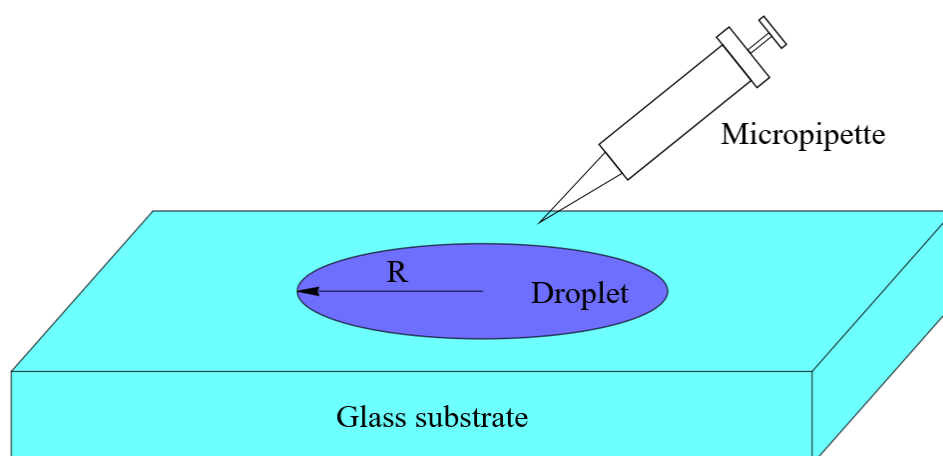


Figure 2.24 Schematic diagram of the experiment procedure for observing the free spreading.

radius is greater than 10 mm. The speed of 30 f.p.s. is sufficient for the observation of spreading behavior.

(II) Wetting behavior

While when observing the wetting behavior, the experiment is conducted with Silicone oil 1 cSt. Make the diagram of position of contact line—contact angle—time, and analyze the observation results.

The silicone oil is deposited on the horizontal surface of glass substrate by the micropipette through a needle and then forms a liquid film immediately. Experiments were performed under $18 \pm 0.5^\circ\text{C}$ room temperature and $46\% \pm 2\%$ of relative humidity. The capillary length under this condition is $l_c = 1.45$ mm. The volume is 1 μL . Before each new experiment, the glass substrate is replaced with a new one.

During the wetting process, the contact line and the interference fringes formed by the surface shape of the liquid film are recorded by the camera with a frame rate of 30 f.p.s..

When observing the wetting behavior of silicone oil 1cSt, the observed spreading time of the liquid is greater than 100 s. And in the following Figure 2.42 between moment 4 and moment 6, there are 140 frames of picture. There are 60 frames of picture between time 4 and time 5. And these are sufficient for studying the wetting behavior of silicone oil 1 cSt. So that the speed of 30 f.p.s. is sufficient for the observation of wetting behavior.

Because the laser used this experiment is the He-Ne laser with a wavelength of 632.8 nm. According to the absorption rate of various wavelengths of light by silicone oil in the literature [6], we can know that silicone oil hardly absorbs the laser light with wavelength of 632.8 nm. Therefore, it can be considered that the laser does not generate heat in the silicone oil, and therefore does not affect the wetting behavior of the silicone oil.

2.5 Results

(I) Spreading behavior

Figure 2.25 shows the images of total reflection of Silicone oil 1 cSt when it is placed on the substrate. It can be seen intuitively from the figure that the existence of the wetting area. And from the figure we can see that in the initial stage of contact between the droplet and the glass substrate, the spreading behavior occurs very quickly.

For the specific measurement of the wetting radius, the brightness of the wetting area needs to be read. Figure 2.26 shows an example of the method of reading the wetting radius in the picture by using the difference in brightness when the silicone oil of 1 cSt droplet spreads freely. Since the area where there is no liquid wetted is total reflection, generally, the intensity of light reflected by the wetting area must be smaller than that of the total reflection area. Therefore, in order to accurately measure the wetting radius, it is necessary to set a control reference in the same area where the brightness is read. The method used in this experiment is to read the brightness value of the same area before the droplet is placed, and then put the two brightness values together for comparison. As shown in Figure 2.26 (b), the wetting radius can be measured by the difference in reflected brightness. Using this method, radius-time data during the spreading process can be obtained.

When to express the relationship about liquid wetting radius, time, surface tension, dynamic viscosity and volume of the liquid in the spreading process, the Tanner's law [7] is usually used. The equation of Tanner's law is as follows:

$$R(t) \approx \left[\frac{10\sigma}{9B\eta} \left(\frac{4V}{\pi} \right)^3 t \right]^{1/10} \propto t^n \quad (2 - 42)$$

The parameters in Equation (2 – 42) are as follows:

R : The wetting radius

σ : Surface tension of the liquid

B : Constant term, $B^{1/10} = 1.186$ (Bonn et al. 2009 [8])

η : Dynamic viscosity

V : Volume of the liquid

t : The spreading time

After Tanner's law is simplified, the wetting radius is proportional to the n -th power of the wetting time. In Equation (2 – 42), the power $n = 1/10$ was corroborated for the viscous spreading of small droplets in many experiments [8], [9~11]. However, this value is not applicable to all liquid's spreading, the value of n between $1/10$ and $1/7$ was reported in some other experiments [10, 12, 13]. Numerical simulations were performed to investigate

the effect of some main parameters, such as surface tension, viscosity, volume. And the simulations showed that in the spreading process of a droplet the combined effect of contact angle and viscosity played an important role [14]. There are two stages in the wetting process when a viscous droplet places on a substrate. One exists before 10^{-3} s, and the other one begins from 10^{-2} s. And in the first stage, the spreading speed is fast. While, in the second stage, the spreading speed is very slow (about 1/500 of the speed in the first stage) and the spreading behavior can be expected from Tanner's law [15]. In this experiment, only the spreading behavior of the second stage is studied, that is, the spreading after 10^{-2} s.

The first experiment performed is the observation of the spreading behavior of 3 μ L of ethanol. The results of wetting radius R and spreading time t are fitted as Tanner's law. The specific form is as follows:

$$R(t) \approx at^n \quad (2 - 43)$$

In the Equation (2 – 43), a is the fitting coefficient.

Figure 2.27 shows the fitting image of the spreading process of ethanol. It can be clearly seen that in the first half of the wetting process, the fitting curve is consistent with the experimentally measured value, but in the later half, the wetting radius stagnates and shrinks. This shrink in the radius is caused by the evaporation of ethanol. According to the result, the value of n equals $0.335 \approx 1/3$ and the fitting coefficient a equals 4741.6. Because there is only one time's experiment, the error range of the measurement results is unknown. Therefore, in the same condition, the spreading experiment of ethanol is performed nine times. The fitting image of the spreading process of ethanol in nine times is shown in Figure 2.28. The result has the same tendency as the result of the first experiment of ethanol. However, the difference is that there are some small deviations. According to the result of the nine times' experiment, the value of n equals $0.311 \approx 1/3$ and the fitting coefficient a equals 4563.4. The error percentage of n between the first time's and the rest eight times' is 7.7%. And in the nine times' values of n , the deviation percentage between the maximum and the average, and the deviation percentage between the minimum and the average is in 9%. With the same method, we have performed three times' experiments in decane and octane, respectively. And the similar results happened. Hence, in this experiment, the value of n , which is fitting by one time's experimental result can be regarded as the approximate the fitting value of multiple experiments under the same conditions.

Figure 2.29 shows the R - t image of the spreading process of 1 μ L of decane. Unlike the image of ethanol, the wetting radius of decane does not shrink rapidly in the latter stage of spreading. While, the inclination of the curve in Figure 2.29 (b) is obviously not as large as that in Figure 2.27 (b). Figure 2.30 shows the R - t image of the spreading process of

decane of 1 μL and 3 μL . It can be seen that the wetting radius of a large volume is larger, but the change rate of the radius seems to have no significantly different. The fitting result also shows that the n value of decane with different volumes is the same, which is $1/6$.

Figure 2.31 shows the R - t image of the spreading process of 1 μL of octane. Although it is similar to the image of decane, which is also alkane, it is obvious that the octane's wetting radius spreading stagnation time is earlier, and the radius's shrinking time is faster than that of decane, but the contraction time is slower than that of ethanol. However, the n value of octane is the same as the n value of decane, which is $1/6$. Figure 2.32 shows the R - t image of the spreading process of 1 μL and 3 μL of octane. It is similar to the image of decane with different volume, the volume is different but has the same n value, and the shrinking time of the wetting radius is similar.

Figure 2.33 shows the R - t image of the spreading process of 5 μL of water. Unlike the previous ethanol and alkanes, the wetting radius of water does not appear to be rapidly shrinking. Only after the water reaches the maximum radius at around 20s, the radius remains constant for a period of time. And according to Figure 2.33(b), the inclination of the curve of radius-exponential time is relatively flat. The fitting result of n value of water is $1/10$.

The wetting experiments of silicone oil 1 cSt and 10 cSt are performed. The first one to be performed is the spreading experiment of silicone oil 1cSt. Figure 2.34 shows the R - t image of the spreading process of 1 μL of silicone oil 1 cSt. Compared with the aforementioned liquids, except for decane, the maximum radius of silicone oil 1cSt appears later. The fitting result of n value of silicone oil 1cSt is $1/4$. As a control of silicone oil 1cSt, silicone oil with a viscosity of 10cSt is also observed. Figure 2.35 shows the R - t image of the spreading process of 1 μL of silicone oil 1cSt and 1 μL of silicone oil 10cSt. Due to the difference in viscosity and surface tension, the two liquids with the same volume also show different spreading behaviors as expected. The spreading of silicone oil 10 cSt is significantly slower, and in this experiment, the time for the wetting radius R to reach the maximum is the latest of all the 6 liquids. After fitting, the n value of silicone oil 10 cSt is the same as that of octane and decane, which is $1/6$.

The R - t images of the wetting process of decane 3 μL , ethanol 3 μL , octane 3 μL , silicone oil 1cSt 1 μL and water 5 μL are drawn together, as shown in Figure 2.36. It can be clearly seen from the figure that the spreading of ethanol is the fastest, and the inclination of the radius-exponential time curve is the largest among these liquids. The curves of decane and octane of alkanes almost overlap, and they have the same n value and similar fitting coefficient a . In the figure, the time when the radius of the liquid decreases in the same

volume indicates the ease of evaporation of the liquid. In Figure 2.36(b), the height of the curves of liquids at 10^0 s indicates the magnitude of their fitting coefficient a .

In order to compare the factors that affect the value of n and a during the spreading process, we put all the parameters and results of the liquids during the experiment in the Table 2.2.

From the results shown in Table 2.2, we can know that the spreading behavior of the same liquid in different volumes has the same n value. Therefore, it can be known that the volume does not affect n . However, the a value changes due to changes in volume. And it can be seen that when the liquid is octane, the a value of 3 μL and 1 μL are 3781.8 and 2379.3 respectively. There is a relationship: $\sqrt[3]{3} = 1.442 \approx 3781.8/2379.3 = 1.589$. Similarly, when the liquid is decane, the a value of 3 μL and 1 μL are 3396.9 and 2324.0 respectively. There is a relationship: $\sqrt[3]{3} = 1.442 \approx 3396.9/2324.0 = 1.462$. The volume V of the liquid has a relationship with the spherical radius R_0 before the liquid spreads: $V \propto R_0^3$. Therefore, we can know that $R_0 \propto a$.

When the liquid is octane : surface tension of octane is σ_o , and a value of 1 μL and 3 μL are a_{o1} and a_{o3} respectively. Similarly, the symbols for decane are σ_d , a_{d1} and a_{d3} respectively. For silicone oil 1cSt and 10 cSt, the symbols are σ_{si1c} , σ_{si10c} , a_{si1c} and a_{si10c} respectively. There are such relationships:

$$\frac{\sigma_o}{\sigma_d} = 0.899 \approx \frac{a_{d1}}{a_{o1}} = 0.977 \approx \frac{a_{d3}}{a_{o3}} = 0.898$$

$$\frac{\sigma_{si1c}}{\sigma_{si10c}} = 0.841 \approx \frac{a_{si10c}}{a_{si1c}} = 0.846$$

That is:

$$\frac{\sigma_1}{\sigma_2} \approx \frac{a_2}{a_1} \quad (2 - 44)$$

Equation (2 – 44) is valid between octane and decane, and it is also valid between silicone oil 1 cSt and silicone oil 10 cSt.

As can be seen from Table 2.2, silicone oil 10cSt, octane and decane have similar surface tension, but the viscosity of silicone oil 10cSt is more than ten times that of the latter two. But the three of them have the same n value. It can be seen that viscosity does not play a leading role in the influence factors of n value. The result obtained here is different from the conclusions obtained by Eddi et al. [15], because in the second stage of spreading ($t > 10^{-2}\text{s}$), the speed is very slow compared to the first stage ($0\text{s} < t < 10^{-3}\text{s}$).

In the spreading process, besides surface tension, viscosity and volume, the contact angle also plays an important role [14]. Figure 2.37 shows the surface profiles of 5 μL of water, 3 μL of decane, 1 μL of silicone oil 1 cSt and 3 μL of ethanol at the contact line near 3mm

when the wetting radius is the largest. From Figure 2.37, we can see the inclination of the surface profile curves of these liquids. Compared with the results in Figure 2.36 and Table 2.2, we can see that liquids with small contact angles have a larger n value. This result is consistent with the conclusion of Legendre et al [14].

In the spreading process of all liquids, the capillary number Ca of silicone oil 1cSt is the largest, about 0.001. Since $Ca=0.001 \ll 1$, we can know that the surface tension effects of all liquids dominate over the viscous effect during the spreading process.

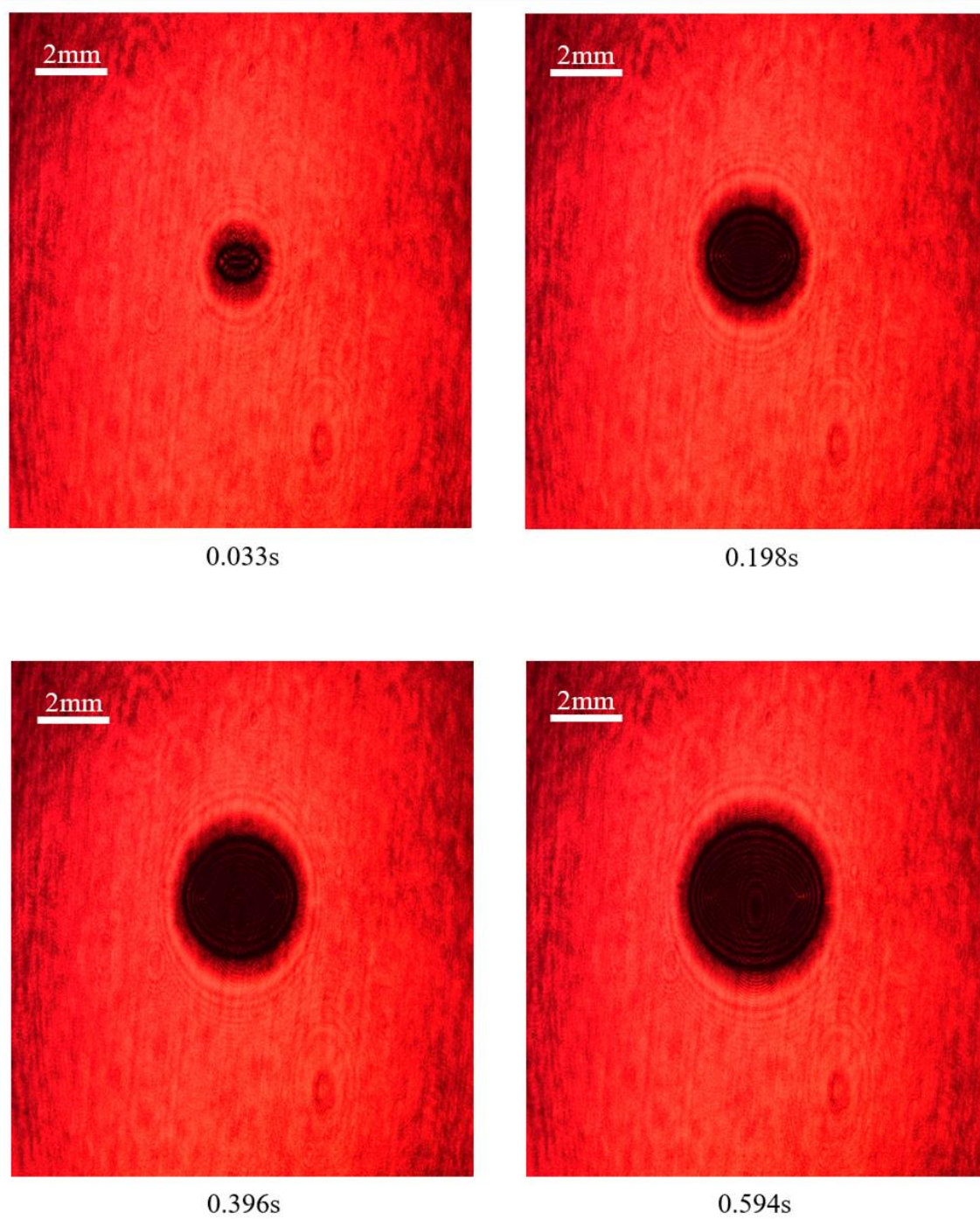


Figure 2.25 Images of total reflection of Silicone oil 1 cSt when it is at 0.033s, 0.198s, 0.396s and 0.594s.

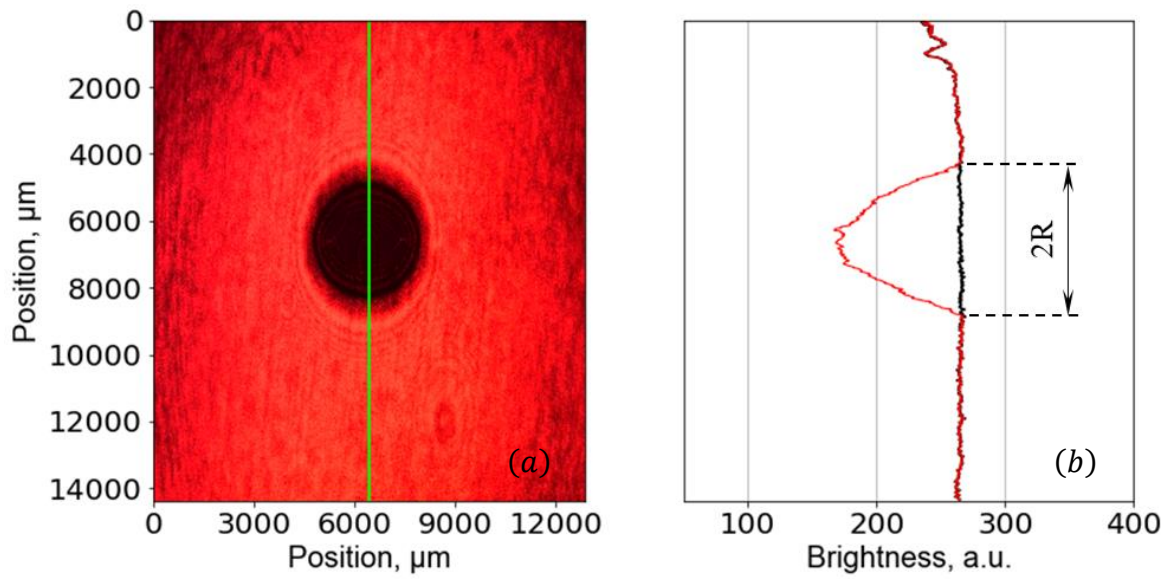


Figure 2.26 An example of the method of reading the wetting radius in the picture by using the difference in brightness when the silicone oil of 1 cSt droplet spreads for 0.396s. The green vertical line in the Figure 2.26 (a) is the line where the brightness is read along. In the Figure 2.26 (b), the red brightness line with an obvious change in the middle is the line read in the Figure 2.26 (a). And the black brightness line without an obvious change in the middle is the line read from the image before placing the droplet. The length of the difference between the two brightness lines is the wetting diameter.

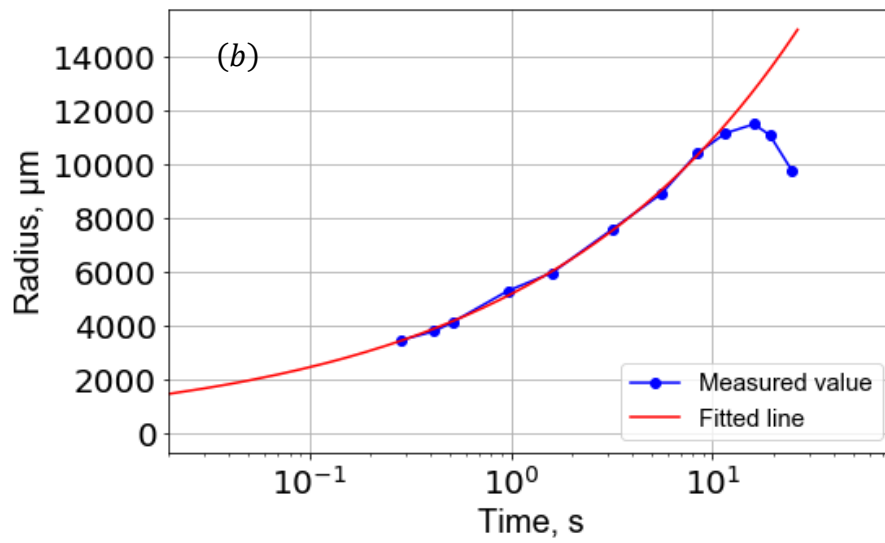
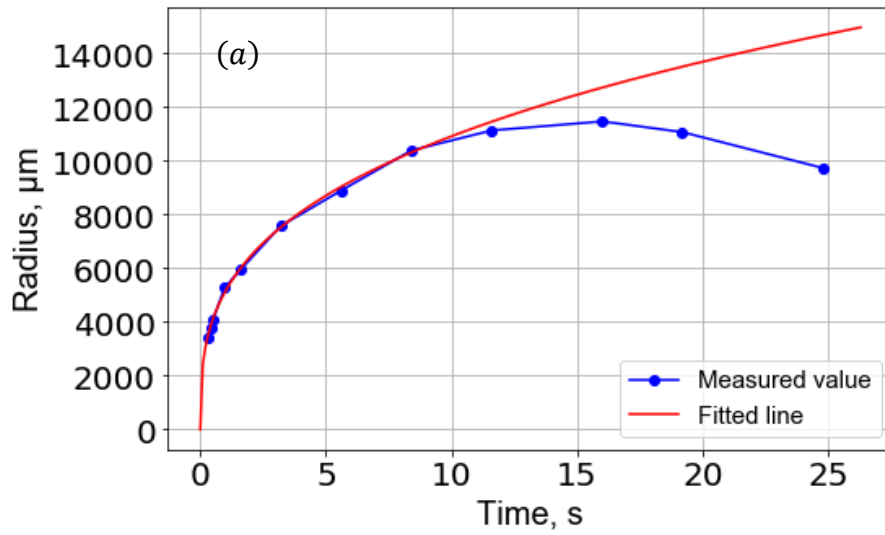


Figure 2.27 The wetting radius of ethanol of $3\mu\text{L}$ as a function of time as fitting by Tanner's law.

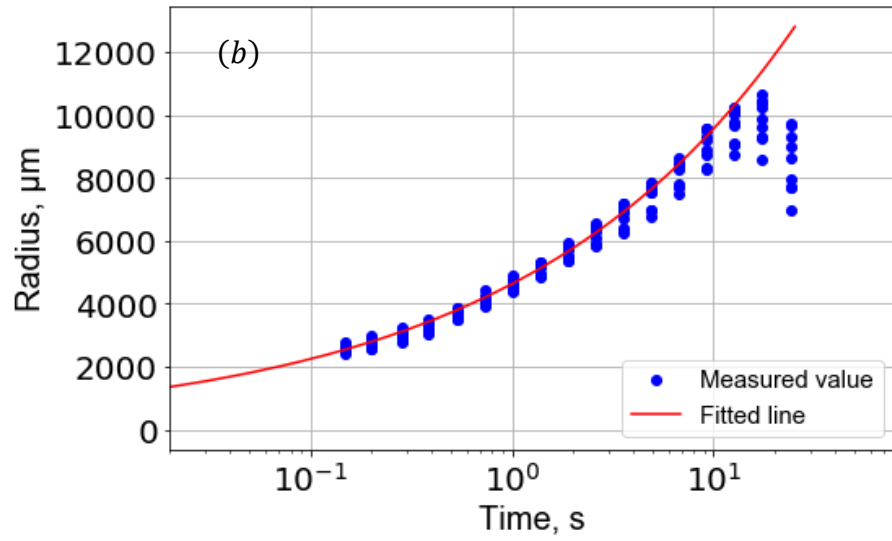
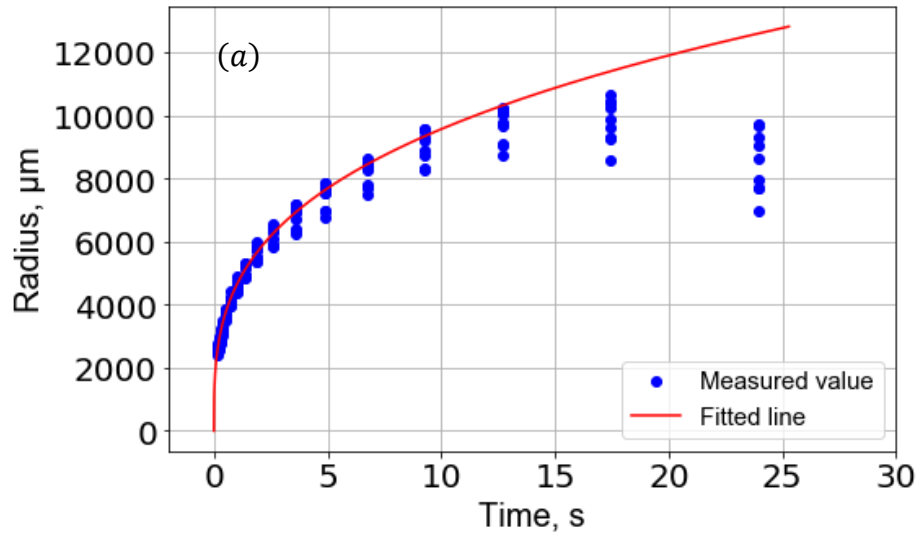


Figure 2.28 The wetting radius of ethanol of $3\mu\text{L}$ as a function of time as fitting by Tanner's law. In order to reduce the errors caused by individual experiments, the fitted values are taken from the results of nine times' experiments.

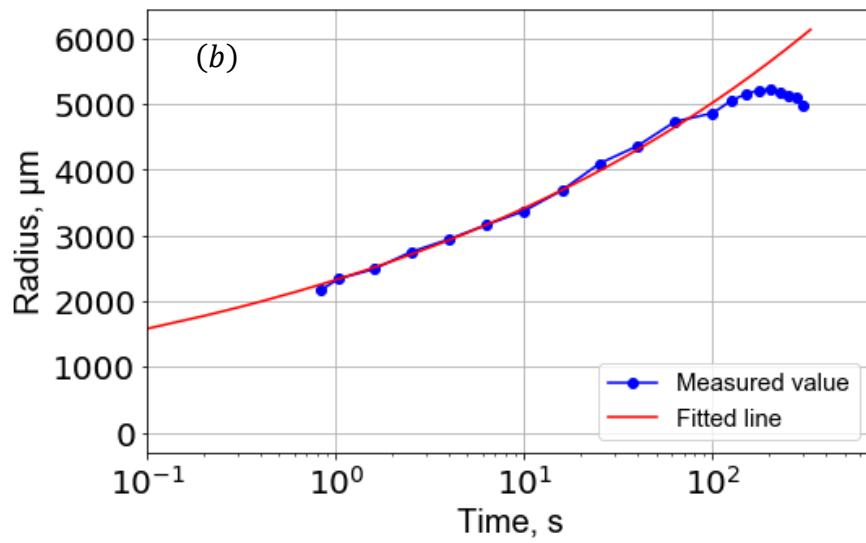
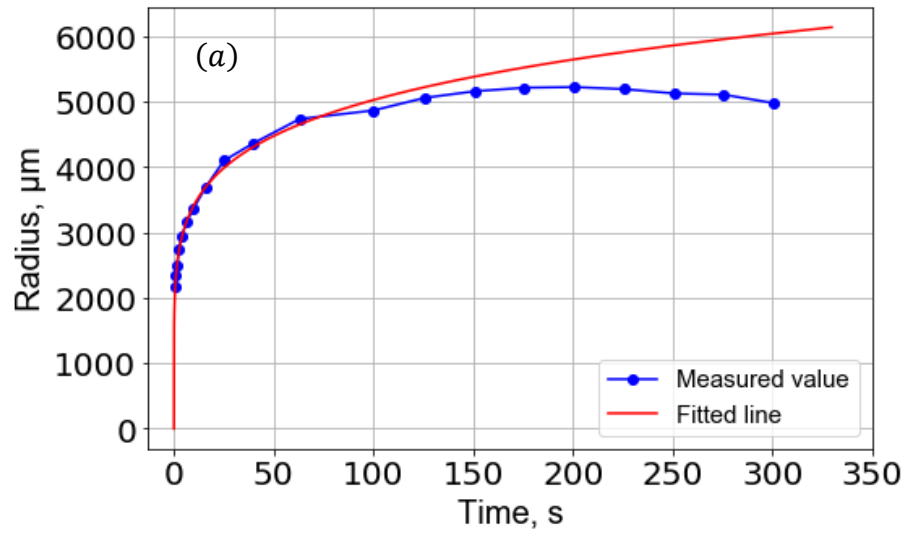


Figure 2.29 The wetting radius of decane of $1\mu\text{L}$ as a function of time as fitting by Tanner's law.

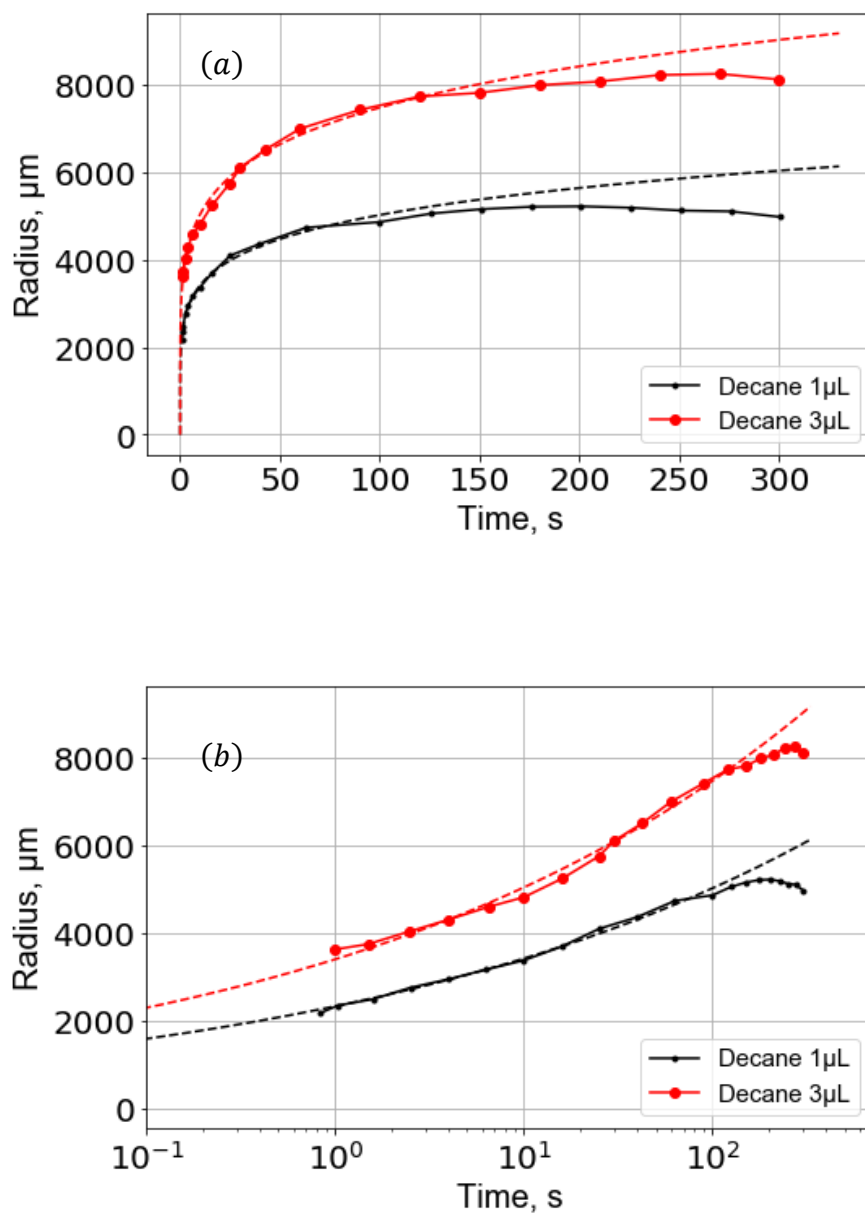


Figure 2.30 The wetting radius of decane of 1 μL and 3 μL as a function of time as fitting by Tanner's law.

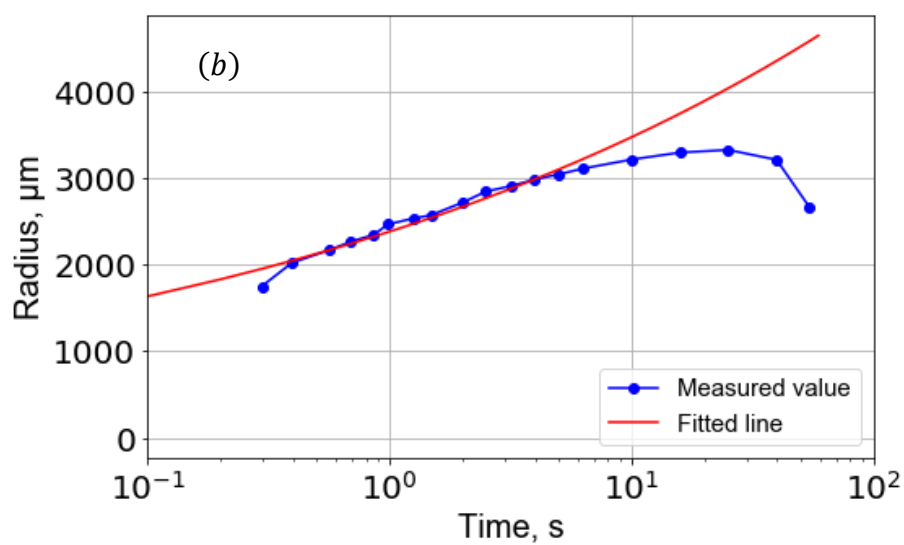
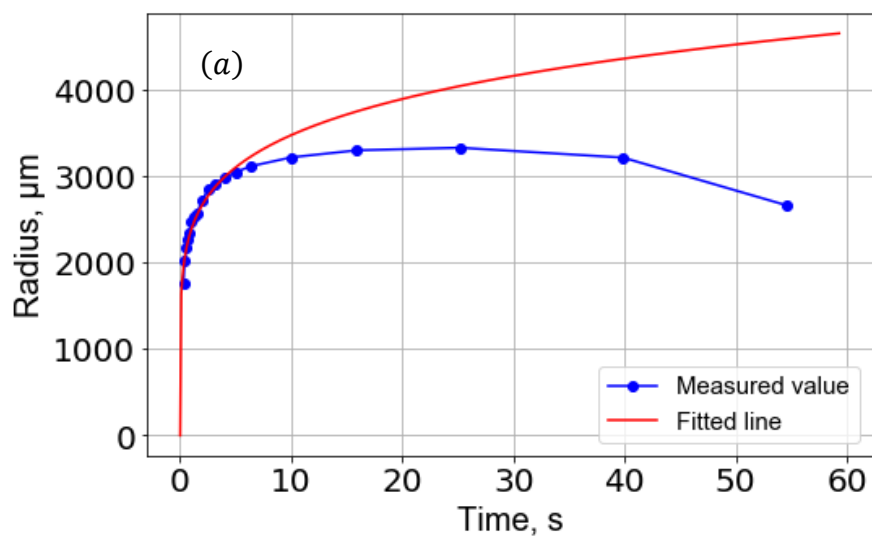


Figure 2.31 The wetting radius of octane of $1\mu\text{L}$ as a function of time as fitting by Tanner's law.

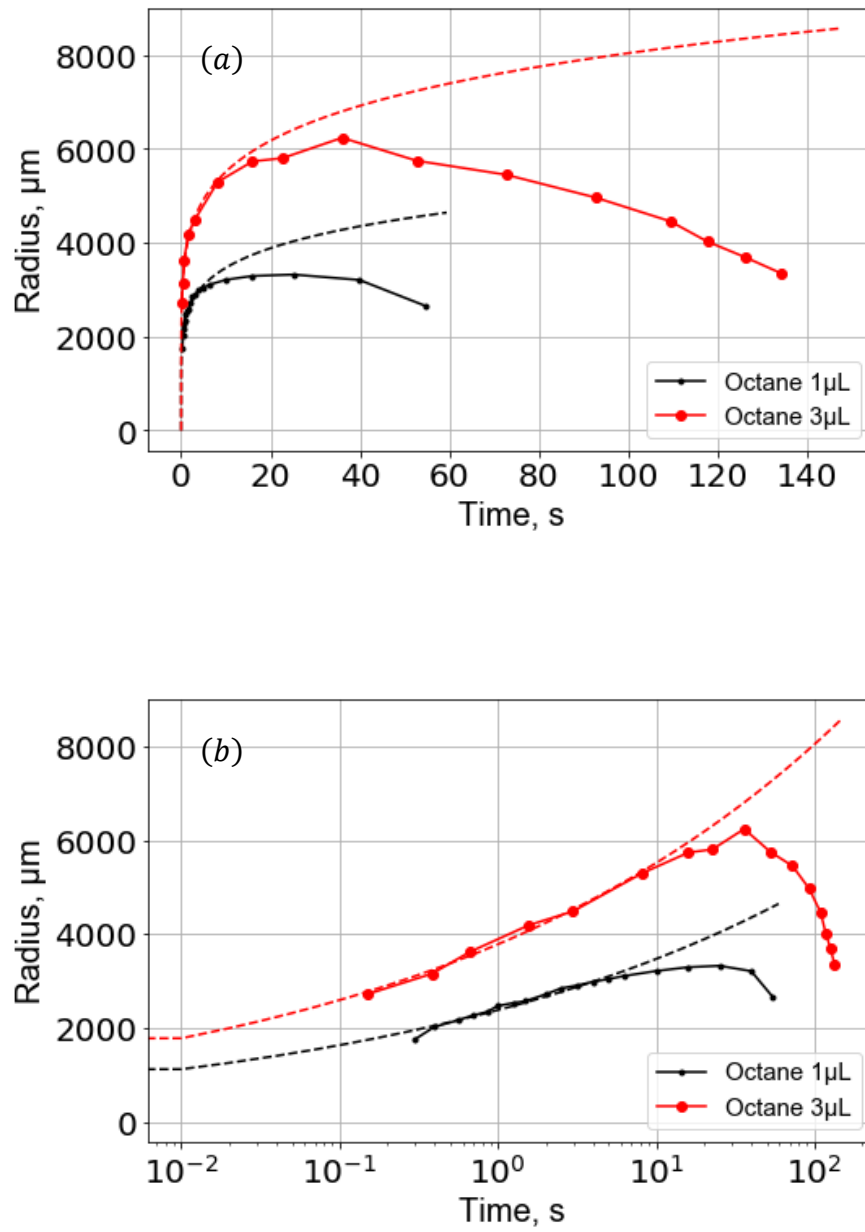


Figure 2.32 The wetting radius of octane of 1 μL and 3 μL as a function of time as fitting by Tanner's law.

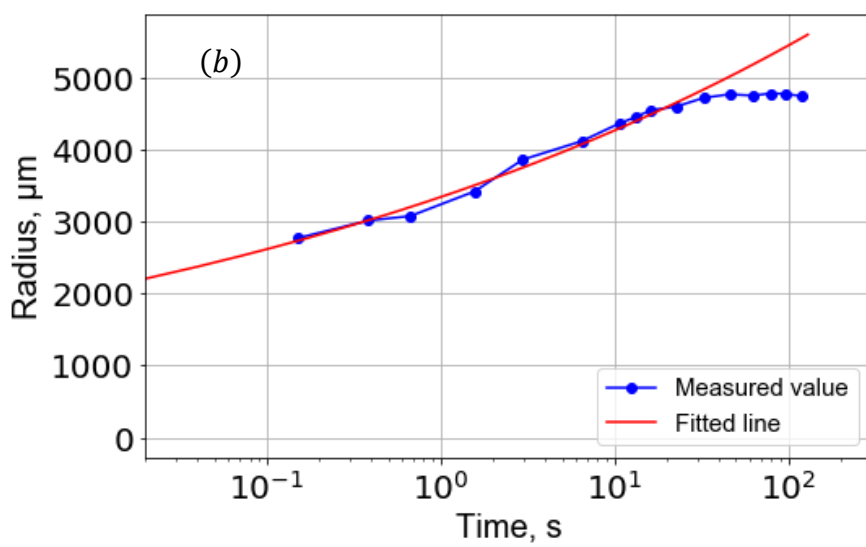
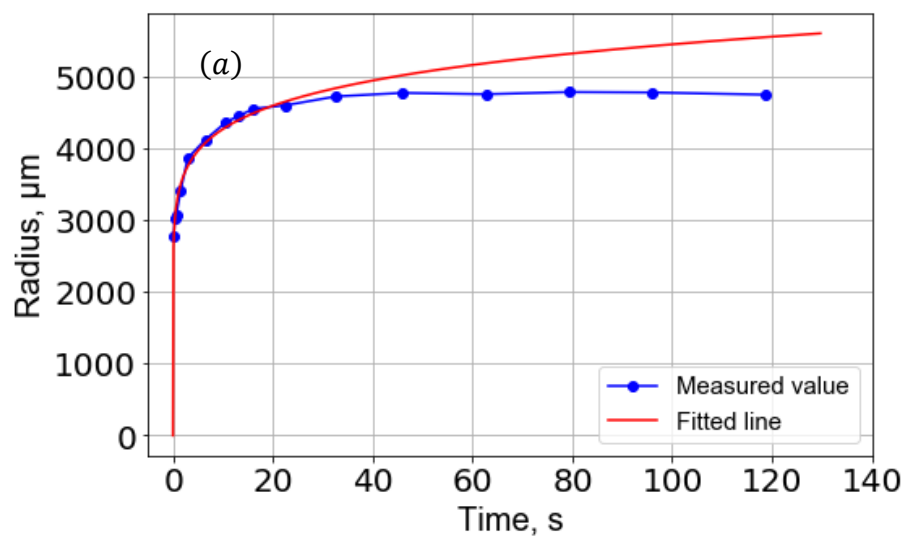


Figure 2.33 The wetting radius of water of $5\mu\text{L}$ as a function of time as fitting by Tanner's law.

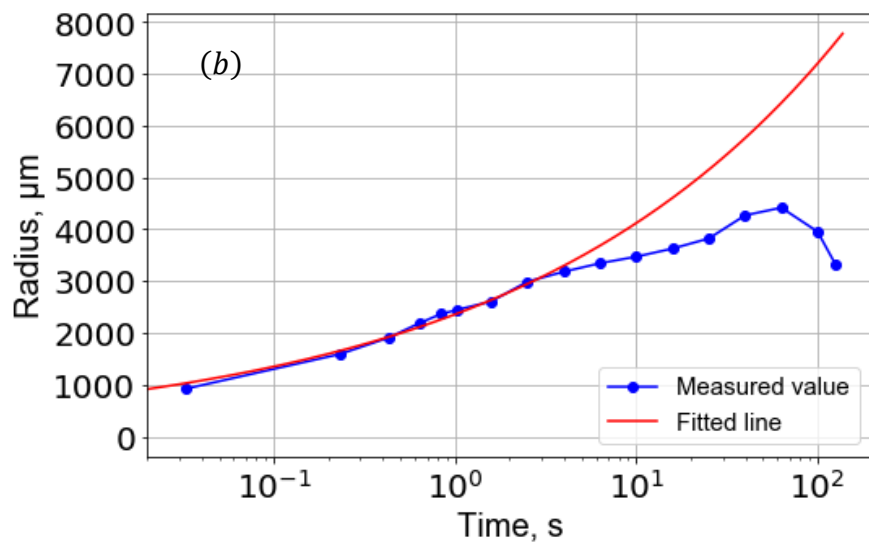
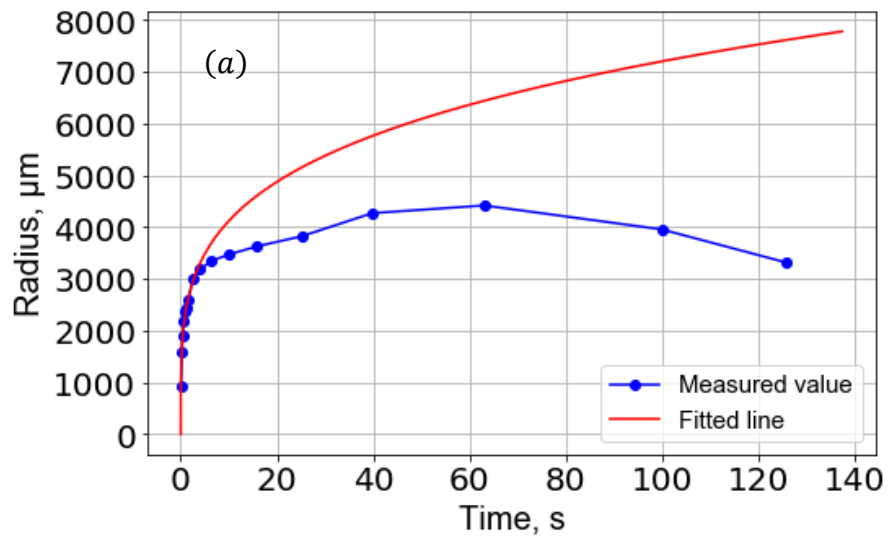


Figure 2.34 The wetting radius of silicone oil 1cSt of $1\mu\text{L}$ as a function of time as fitting by Tanner's law.

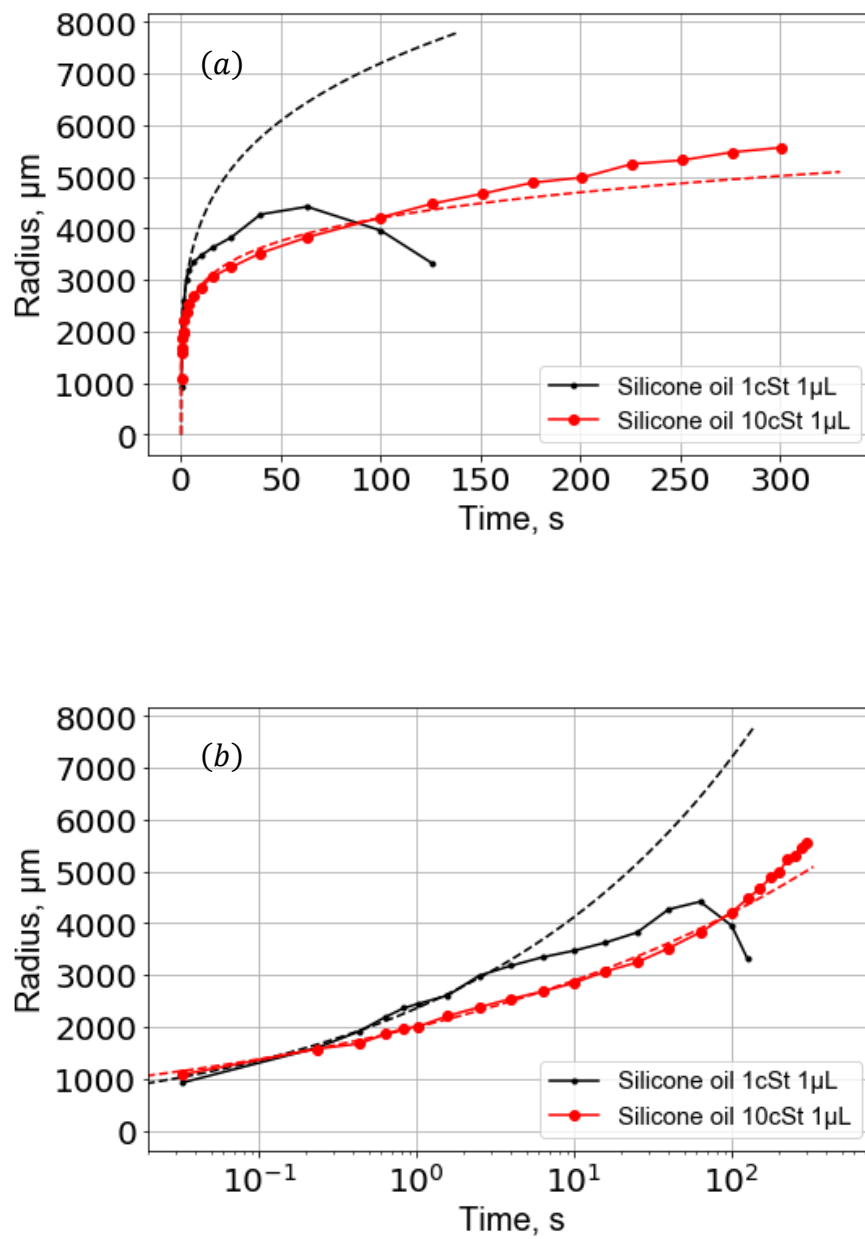


Figure 2.35 The wetting radius of silicone oil 1cSt of $1\mu\text{L}$ and silicone oil 10cSt of $1\mu\text{L}$ as a function of time as fitting by Tanner's law.

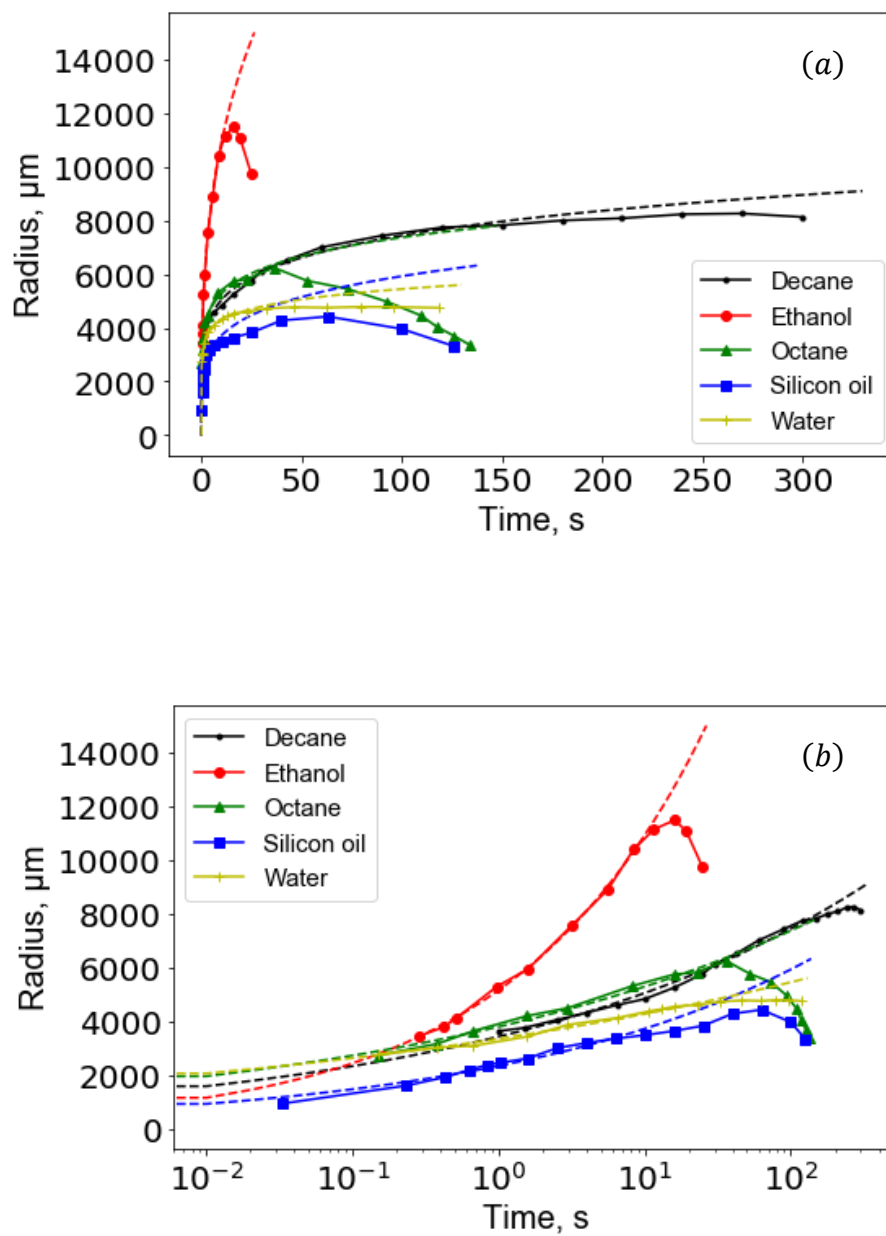


Figure 2.36 The wetting radius as a function of time as fitting by Tanner's law. The liquids are decane of $3\mu\text{L}$, ethanol of $3\mu\text{L}$, octane of $3\mu\text{L}$, silicone oil 1cSt of $1\mu\text{L}$ and water of $5\mu\text{L}$.

Table 2.2 Parameters (surface tension, viscosity, volume, a and n) of the 6 liquids.

	Surface tension σ mN/m	Viscosity η mPa · s	Volume V μ L	a	n
Octane	21.4	0.56	3	3781.8	$0.164 \approx \frac{1}{6}$
Octane	21.4	0.56	1	2379.3	$0.164 \approx \frac{1}{6}$
Decane	23.8	0.838	3	3396.9	$0.171 \approx \frac{1}{6}$
Decane	23.8	0.838	1	2324.0	$0.167 \approx \frac{1}{6}$
Ethanol	22.16	1.148	3	4741.6	$0.335 \approx \frac{1}{3}$
Silicone oil 1cSt	16.9	1.222	1	2358.7	$0.242 \approx \frac{1}{4}$
Silicone oil 10cSt	20.1	10.695	1	1995.8	$0.162 \approx \frac{1}{6}$
Water	72.28	0.936	5	3338.5	$0.106 \approx \frac{1}{10}$

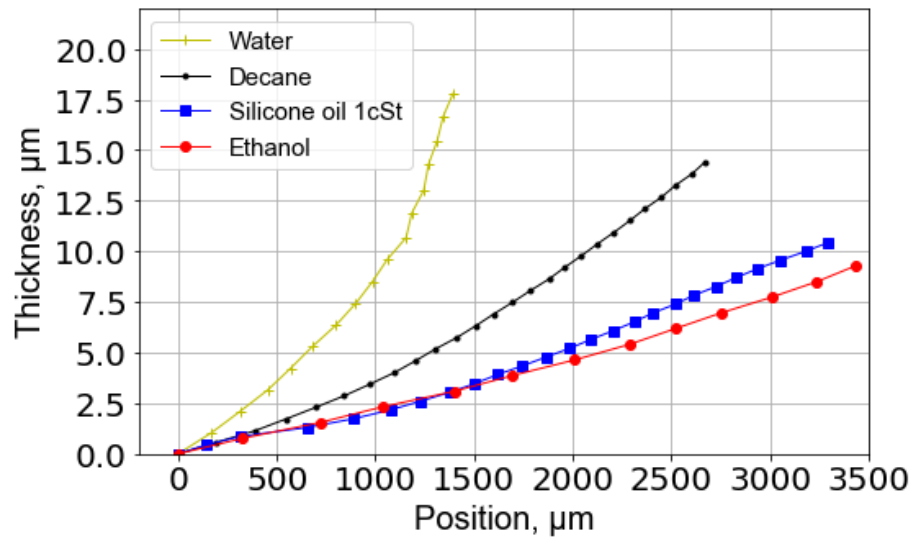


Figure 2.37 Surface profiles of 5 μL of water, 3 μL of decane, 1 μL of silicone oil 1 cSt and 3 μL of ethanol at the contact line near 3mm when the wetting radius is the largest.

(II) Wetting behavior

The wetting experiment of silicone oil 1cSt droplet is observed by our interference fringe method. Figure 2.38 shows the typical interference fringe, brightness curve and calculated surface profile of the liquid film. Figure 2.38 (b) shows the brightness-position curve. Due to the total reflection area and partial reflection area, it is easy to determine the position of the contact line from the brightness-position curve. The first fringe is the first dark fringe adjacent to the contact line. By measuring the spacing of the adjacent interference fringes which are produced by the curvature of the air-liquid interface, the surface profile of the liquid film can be calculated with Equation (2 – 37) and (2 – 38) (as shown in Figure 2.38 (c)). Figure 2.39 shows the surface profiles which are calculated by this method at four moments during the wetting process. In this figure, the dashed lines are fitted according to a part of a circle. The thickest part of the liquid film is around 20 μm . With the passage of time, the wetting diameter is constantly changing. At the same time, the thickness of the liquid film is getting thinner and the total volume continues decreasing due to evaporation. During the entire evaporation process, although the profiles of the left and right sides of the droplet do not differ greatly, they do not change completely symmetrically.

When liquid droplets spread freely on a solid surface with uniform material, the shape is usually a rotating body of the section. Figure 2.40 shows that the surface profile of the silicone oil 1cSt droplet is placed on the x - y coordinate axis. We can see that the surface profile of the droplet is composed of smooth curves. Therefore, we can fit the profile curve to several equations about x and y . Then when calculating the droplet volume, it can be calculated by using Equation (2 – 45) according to the fitted equations.

$$V = \int_0^{h_f} \pi \{f(y)\}^2 dy \quad (2 - 45)$$

In the Equation (2 – 45):

V : Volume of the droplet

h_f : Thickness of the highest point of the droplet film

$f(y)$: The relationship between y and x

Using this method, we obtained that the droplet volume at 41.6s is 0.3596 μL , and the droplet volume at 64.6s is 0.3356 μL . Therefore, we can know that the average evaporation rate of the droplet is 0.0010 $\mu\text{L} \cdot \text{s}^{-1}$ during the process from 41.6s to 64.6s. The evaporation rate of the droplet in other time periods can also be calculated by using the same method.

In the experiment, when measuring the contact angle, there are two continuously changing angles around the contact line. Both of the angles can be used to characterize the progress of wetting. For the two angles, one is contact angle at the contact line (CA_a) and the other one

is contact angle near the contact line (CA_n). As shown in Figure 2.38 (c), in the same cross section, connect the point of the contact line and the reflection point of the first fringe to form a line segment. The CA_a is the inclination angle of this line segment. From the geometric relationship about the spacing between the contact line and the first fringe (L_{CF}) and CA_a in Figure 2.38 (c), we can know that L_{CF} and CA_a are negatively correlated. The CA_n is the average value of the inclination angles at three adjacent reflection points near the contact line. Figure 2.41 indicates the relationship about position of the contact line and the first fringe, the CA_a and the CA_n in the wetting process. However, as Figure 2.41 (b) and (c) indicate, the CA_a and the CA_n show opposite trends. As Figure 2.41 (a) shows, before advancing of the contact line stops, the liquid spreads out quickly until at 64 s. At about 125 s, the contact line cannot be kept in the range of the positions in the past 61 s and starts to recede. During the wetting process, for the contact line, there are three stages can be found. They are advancing, stable and receding stage, respectively. As shown in Figure 2.41 (a), in the advancing stage, the contact line keeps advancing, and there is no big fluctuations in the L_{CF} . In the same time, as Figure 2.41 (b) and (c) shows, the CA_a shows an increasing trend, while the CA_n shows a decreasing trend. When entering the stable stage, the position of the contact line does not change significantly. However there are some big fluctuations in the first fringe, which leads some fluctuations in L_{CF} . Both of the CA_a and CA_n do not change monotonously and begin reciprocating changes. The changes are sharp. The sharp receding of the first fringe corresponds to the sharp decreasing of the CA_a . And the sharp advancing of the first fringe corresponds to the sharp increasing of the CA_a . For the CA_n , the corresponding situation of change is opposite. For the receding stage, the contact line recedes continually and there are no big fluctuations in the CA_a .

In Figure 2.42 (a), 1 to 9 indicate nine moments in the wetting process. The surface profiles of the liquid film near the contact line at these nine moments are shown in Figure 2.42 (b), (c) and (d). Among the nine moments, 1 and 2 are in the advancing stage. The moment of 2 is also the start of the stable stage. And 3 to 7 are in the stable stage. As shown in Figure 2.42 (a), the L_{CF} at the moment of 5 is shorter than it at the moment of 4 and 6. Profiles in Figure 2.43 are partial enlarged drawing of the profiles at the moments of 4 to 6 near the contact line. The profile at the moments of 4 and 6 almost overlap. In this figure, the CA_a is the inclination angle of the part indicated by the blue double arrow, and the CA_n is the inclination angle of the part indicated by the black double arrow. When the liquid film has a shorter L_{CF} , the liquid film is thicker, and has a bigger CA_a and a smaller CA_n than the liquid film with a bigger L_{CF} . There are some processes of reciprocating change in thickness, CA_a and CA_n when profiles change from 2 to 7 in the stable stage (as shown in

Figure 2.41 and Figure 2.42). It can be seen that the reciprocating changes in the two contact angles and the thickness of the liquid film near the contact line, like the edge of the surf. The moment of 8 is the end of the stable stage, as shown in Figure 2.42 (a), and it is also the end of the reciprocating changes.

For the reciprocating changes of contact angles and the thickness of the liquid film, evaporation is an important reason that has to be considered. From the profiles shown in Figure 2.39, the liquid has been evaporating. Since the liquid film near the contact line is very thin, a small amount of evaporation will affect the contact angle. As the liquid film becomes thinner, the contact angle also becomes smaller. According to Tanner's law, when the contact angle of a liquid originally in equilibrium becomes smaller, the combined force of the liquid surface tension and the solid-liquid interfacial tension will be greater than the solid-gas interfacial tension. The liquid will tend to return to the equilibrium state, so the contact angle will increase again. The repetition of this process forms the phenomenon of reciprocating changes in the contact angles and the thickness of the liquid film.

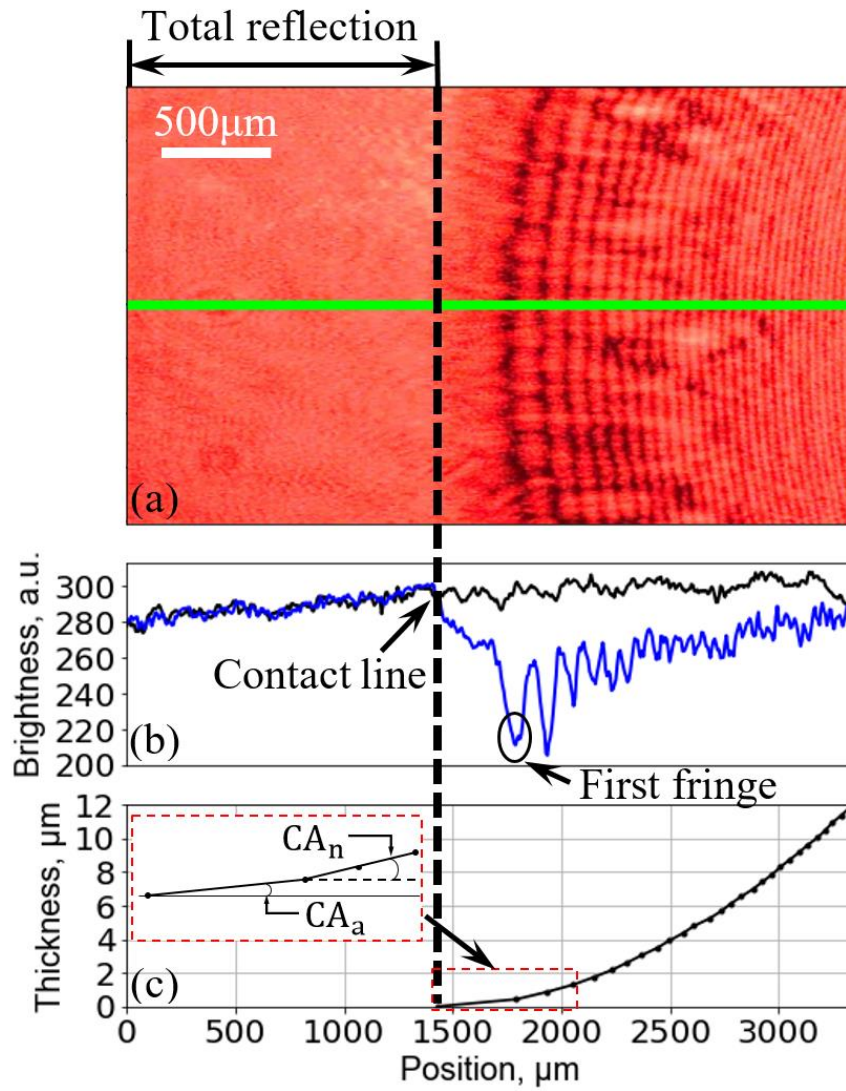


Figure 2.38 A snapshot of interference fringes of the liquid film formed by silicone oil droplet in the wetting process. The black vertical dotted line is located at the position of the contact line in Figure 2.38 (a), (b) and (c). In Figure 2.38 (a), the green horizontal line indicates the analyzing line. The black curve in Figure 2.38 (b) indicates the brightness of the reflected light when the droplet is unplaced. The blue curve indicates the brightness of the reflected light with the droplet. In Figure 2.38 (c), the black curve indicates the calculated surface profile of the droplet, and the red dotted rectangular part is an illustration of CA_a and CA_n .

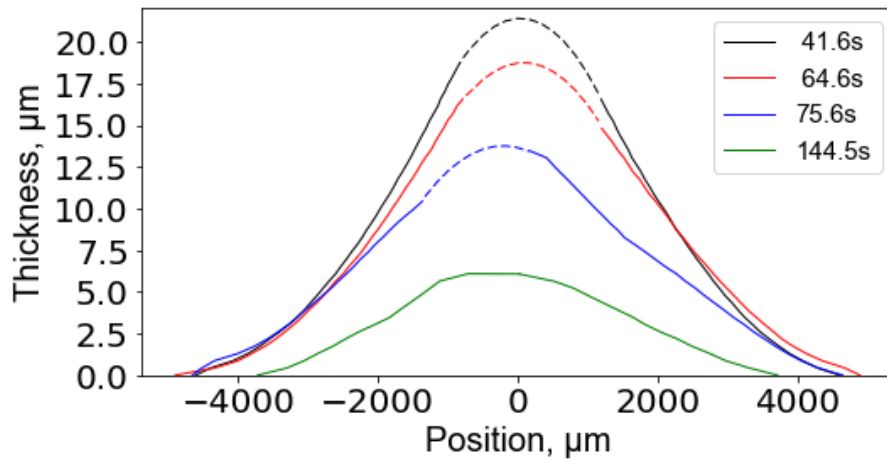


Figure 2.39 Surface profiles of the liquid film at four moments. In this figure, the solid line parts are calculated from interference fringes, and the dash line parts are fitted with a circle. With the passage of time, the wetting radius of the liquid film spreads outward from the initial position of 41.6s to the position of 64.6s, and then after 11s, the wetting radius recedes to almost the same position as that of 41.6s. However, the thickness of the liquid film continues to become thinner due to the existence of evaporation. When it is 144.5s, the thickness of the liquid film and the wetting radius have reached the minimum of these four moments.

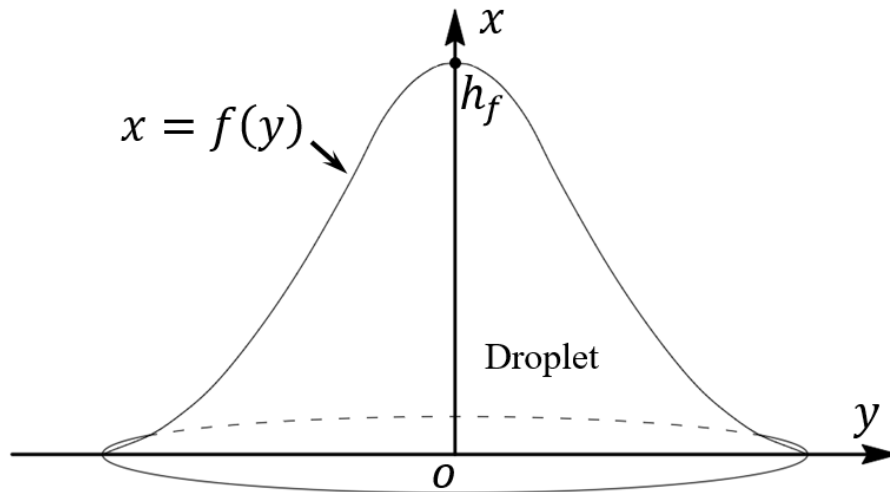


Figure 2.40 Schematic diagram of the surface profile of the droplet when it is placed in the x - y coordinate axis. In this figure, h_f is the thickness of the highest point of the droplet film and $f(y)$ is the relationship between y and x on the surface profile.

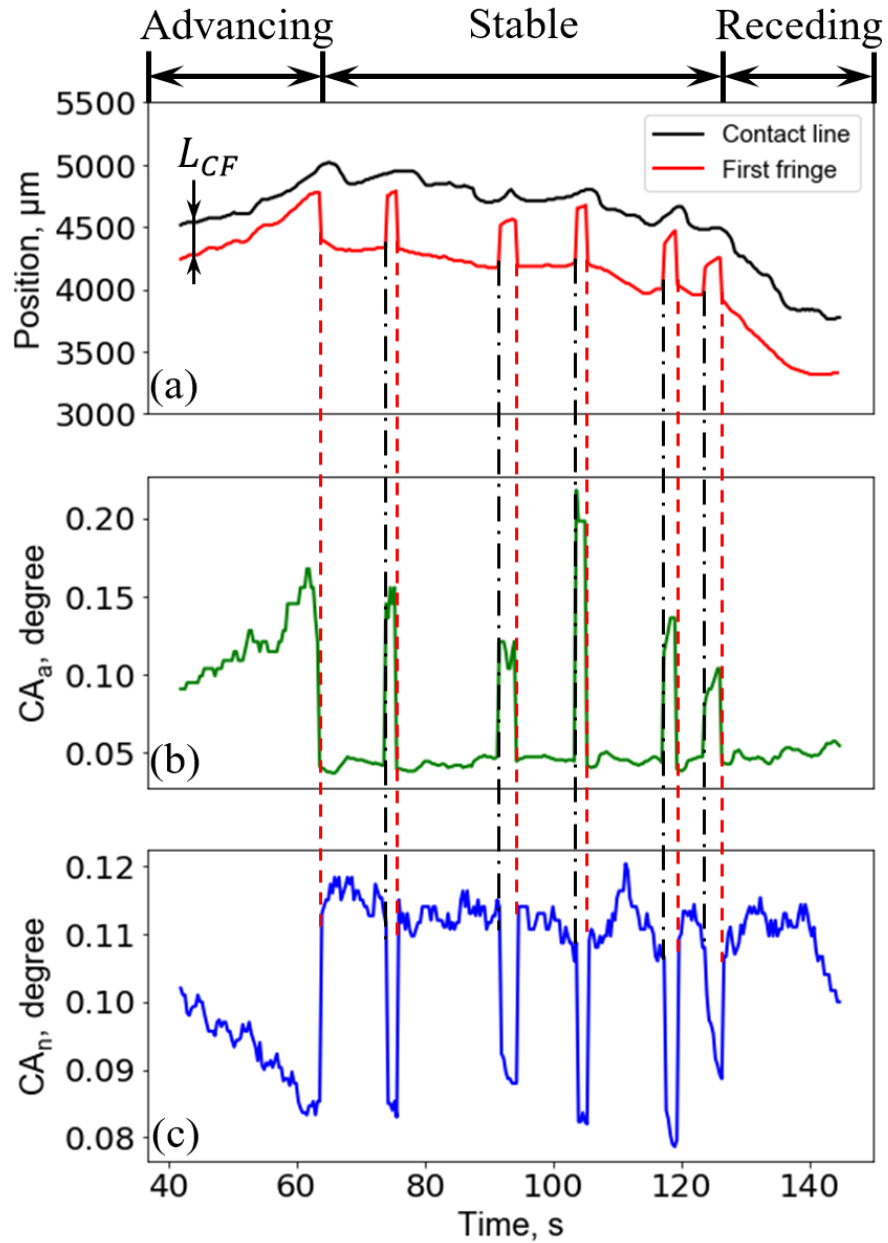


Figure 2.41 Relationship about position of the contact line and the first fringe, the CA_a and the CA_n . In Figure 2.40 (a), the black curve indicates the position of the contact line and the red curve indicates the position of the first fringe. In this figure, the red vertical dashed lines indicate the moments when the position of the first fringe recede sharply. And the black vertical dashed-dotted lines indicate the moments when the position of the first fringe advance sharply.

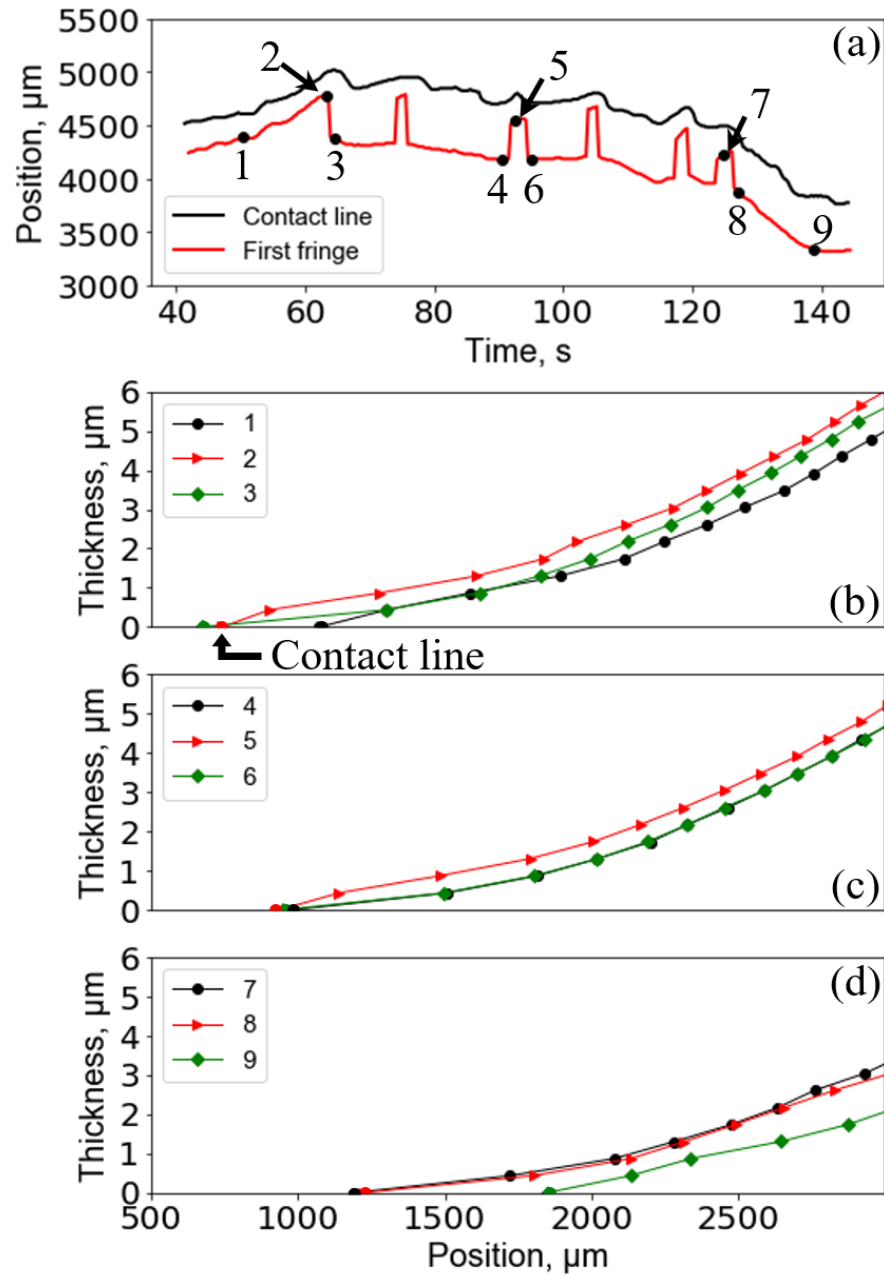


Figure 2.42 Surface profiles of the liquid film near the contact line. 1 to 9 in Figure 2.42 (a) indicate the nine moments in the wetting process. The surface profiles of the liquid film near the contact line at the nine moments are shown in Figure 2.42 (b), (c) and (d).

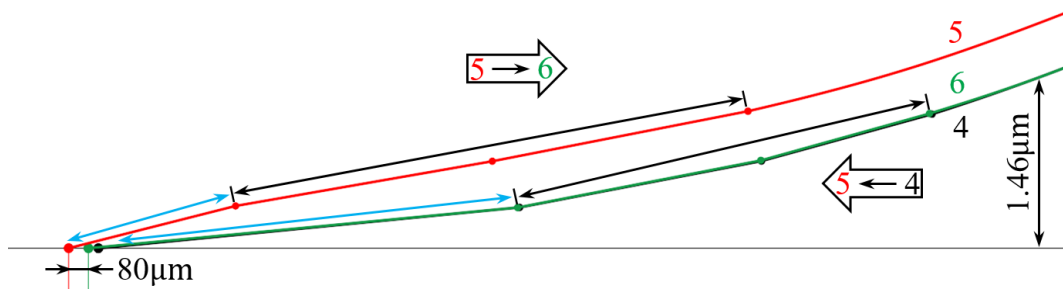


Figure 2.43 Partial enlarged drawing of the profiles at the moments of 4 to 6 near the contact line. Profile changes from moment 4 to 5, and then changes to moment 6, while the contact line moves $80\mu\text{m}$. The profile at the moments of 4 and 6 almost overlap.

2.6 Conclusion

In order to study the spreading and wetting behavior of a liquid film on a super-hydrophilic surface without considering the existence of objects above the liquid blocking the laser, an interference fringe method with oblique upward laser is developed. And with this method the contact angle and the position of the contact line of the liquid film can be measured simultaneously. The equations are confirmed by verification experiments. And the contact angle measurement is verified from 0.007° to 3° .

In the spreading and wetting experiment, by setting the incident angle of laser, so that the non-wetting part has total reflection and wetting part has partial reflection. As a result, the position of the contact line can be determined.

The spreading behavior of 6 liquids is observed. By observing the spreading process, some factors affecting spreading behavior have been confirmed. The spherical radius R_0 of liquid before it spreads has a relation to the fitting coefficient a : $R_0 \propto a$. A relation $\sigma_1/\sigma_2 \approx a_2/a_1$ is valid between octane and decane, and it is also valid between silicone oil 1 cSt and silicone oil 10 cSt. The result also shows that viscosity does not play a leading role in the influence factors of n value in the Tanner's law. In the spreading process, besides surface tension, viscosity and volume, the contact angle also plays an important role and liquids with small contact angles have a larger n value.

The wetting behavior of a liquid film of silicone oil 1 cSt on the super-hydrophilic surface is observed by this interference fringe method. The contact angles and profile of liquid film can be calculated by the derived equations with the spacing of the fringes. According to the results of the wetting experiment, position of the contact line, the surface profile of the liquid film and the contact angles can be observed simultaneously. While, when measuring the contact angle, two contact angles are measured. One is the inclination angle of the connecting line between the contact line and the reflection point of the first fringe. The other one is the average value of the inclination angles at the three adjacent reflection points near the contact line. And the two contact angles have opposite trends. In addition, there are three stages occurred in the wetting process. They are advancing, stable and receding stage. In the first stage, the position of the contact line continues advancing. And both contact angles have a monotonous change. In the second stage, the position of the contact line does not change significantly, while there are some fluctuations in the L_{CF} . That is caused by reciprocating changes in the CA_a . In the third stage, the position of the contact line is receding and the contact angles have no reciprocating changes. The advancing contact angle is often larger than the receding contact angle in the wetting process. In this experiment, the CA_a is constantly increasing in the advancing stage, however remains unchanged in the receding

stage, and the CA_a in the advancing stage is larger than it in the receding stage. For the CA_n , in the first half of the receding stage, the CA_n keeps unchanged, and in the latter half of the stage, the CA_n rapidly decreases. And the CA_n in the advancing stage is smaller than it in the receding stage.

References of chapter 2

- [1] Zhang, Y.; Shen, F.; Cao, W.; Wan, Y. Hydrophilic/hydrophobic Janus membranes with a dual-function surface coating for rapid and robust membrane distillation desalination. *Desalination* 2020, **491**, 114561.
- [2] Lai, C.C.; Chung, C.K. Hydrophilicity and optic property of polyethylene glycol coating on polydimethylsiloxane for fast prototyping and its application to backlight microfluidic chip. *Surface and Coatings Technology* 2020, **389**, 125606.
- [3] Zhong, H.; Hu, Y.; Wang, Y.H.; Yang, H.X. TiO₂/silane coupling agent composed of two layers structure: A super-hydrophilic self-cleaning coating applied in PV panels. *Applied Energy* 2017, **204**, 932-938.
- [4] Born, M.; Wolf, E. *Principles of Optics*. New York, NY: Pergamon Press INC 1959, p.37.
- [5] Sakai, J. *Fundamentals of optical instruments*, Morikita Publishing Corporation: Tokyo, 2013; pp 90-91.
- [6] Xu, M; Wang, X.H; Jin, B.Y; Ren, H.W. Infrared optical switch using a movable liquid droplet. *Micromachines* 2015, **6**, 186-195.
- [7] Tanner, L.H. The spreading of silicone oil drops on horizontal surfaces. *Journal of Physics D: Applied Physics* 1979, **12**, 1473.
- [8] Bonn, D.; Eggers, J.; Indekeu, J. Wetting and spreading. *Reviews of Modern Physics* 2009, **81**, 739-805.
- [9] Chen, J.D.; Wada, N. Wetting dynamics of the edge of a spreading drop. *Physical Review Letters* 1989, **62**, 3050.
- [10] Cazabat, A.M.; Cohen Stuart M.A. Dynamics of wetting: effects of surface roughness. *The Journal of Physical Chemistry* 1986, **90**, 5845-5849.
- [11] Levinson, P.; Cazabat, A.M.; Heslot, F. The spreading of macroscopic droplets. *Revue de physique appliquée* 1988, **23**, 1009-1016.
- [12] Lopez, J.; Miller, C.A. and Ruckenstein, E. Spreading kinetics of liquid-drops on solids. *Journal of Colloid and Interface Science* 1971, **56**, 4660-4668.
- [13] Ehrhard, P. Experiments on isothermal and nonisothermal spreading. *Journal of Fluid Mechanics* 1993, **257**, 463-483.
- [14] Legendre, D.; Maglio, M. Numerical simulation of spreading drops. *Colloids and Surfaces A: Physicochemical and Engineering Aspects* 2013, **432**, 29-37.
- [15] Eddi, A.; Winkels, K.G. and Snoeijer, J.H. Short time dynamics of viscous drop spreading. *Physics of Fluids* 2013, **25**, 013102.

3. Cross-linking adhesive force of liquid bridge

3.1 Background

More than one hundred years ago, the liquid bridge stretching was studied by Plateau and Rayleigh [1, 2]. In recent years, the industrial applications such as fiber spinning, atomization, coatings and gravure printing, are closely related to the liquid bridge stretching [3~5]. And liquid bridge stretching and pinch-off control the agglomeration of wet particles [6~8].

Especially, with the development of mechanical technology, downsizing of machines is remarkable. Unlike large machines, the effect of cross-linking adhesive force due to the liquid bridge in wet environment cannot be ignored in small machines. For example, in a humid environment, its movement is affected by liquid bridges formed between small machines. Therefore, the influence of the humid environment cannot be ignored in the design and development of small machines. It is important to evaluate the cross-linking adhesive force acting in a humid environment.

The liquid bridge is created between two rigid bodies with an arbitrary shape. As shown in Figure 3.1, it is an example of the schematic diagram of liquid bridge. In this research, the curvature of the liquid-gas interface is called the meniscus, and the three phase contact line of solid-liquid-gas, as explained in Section 1.1, is called the contact line. In this model, the upper contact surface is a spherical surface, and the lower contact surface is a plane.

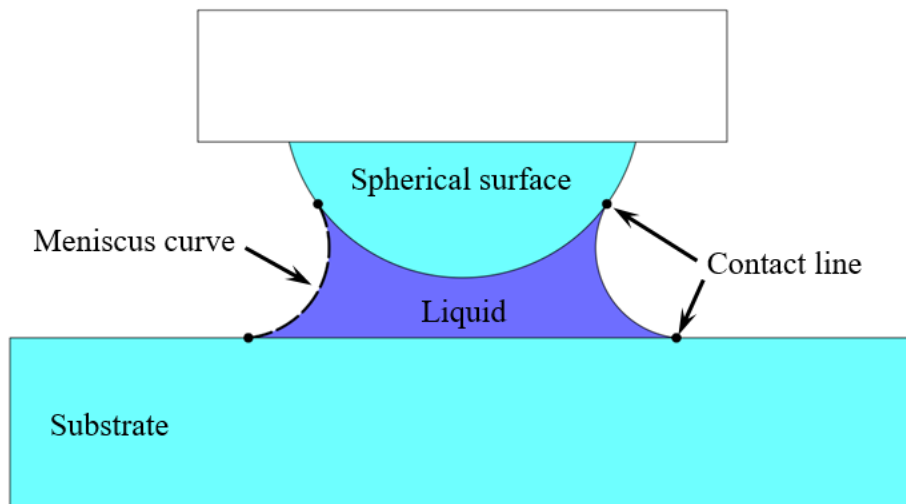


Figure 3.1 Schematic diagram of a liquid bridge.

It is known that the cross-linking adhesion force is closely related to the meniscus shape [9]. In the previous studies, the meniscus shape of liquid bridges are mainly observed directly from side with a camera. As shown in Figure 3.2 (a), is an image of liquid bridge observing by side view method. However, when the contact area (wetting area) is not round, as shown in Figure 3.2 (b)[10], the contact area is difficult to observe only by the side view method. And also in the case of a liquid with good wettability, an extremely thin film may be formed at the contact line of the liquid bridge, which is difficult to observe with the side view method. What role this film plays in the liquid bridge is still unclear.

Therefore, in this study, we performed the contact and separation experiments to observe the meniscus shape and the wetting condition by using the side view method and the total reflection method, and at the same time recorded the cross-linking adhesion force and the meniscus shape of several kinds of liquids. The purpose of this study is to observe the wetting behavior in the liquid bridge and investigate the influence of the thin film on cross-linking adhesion force.

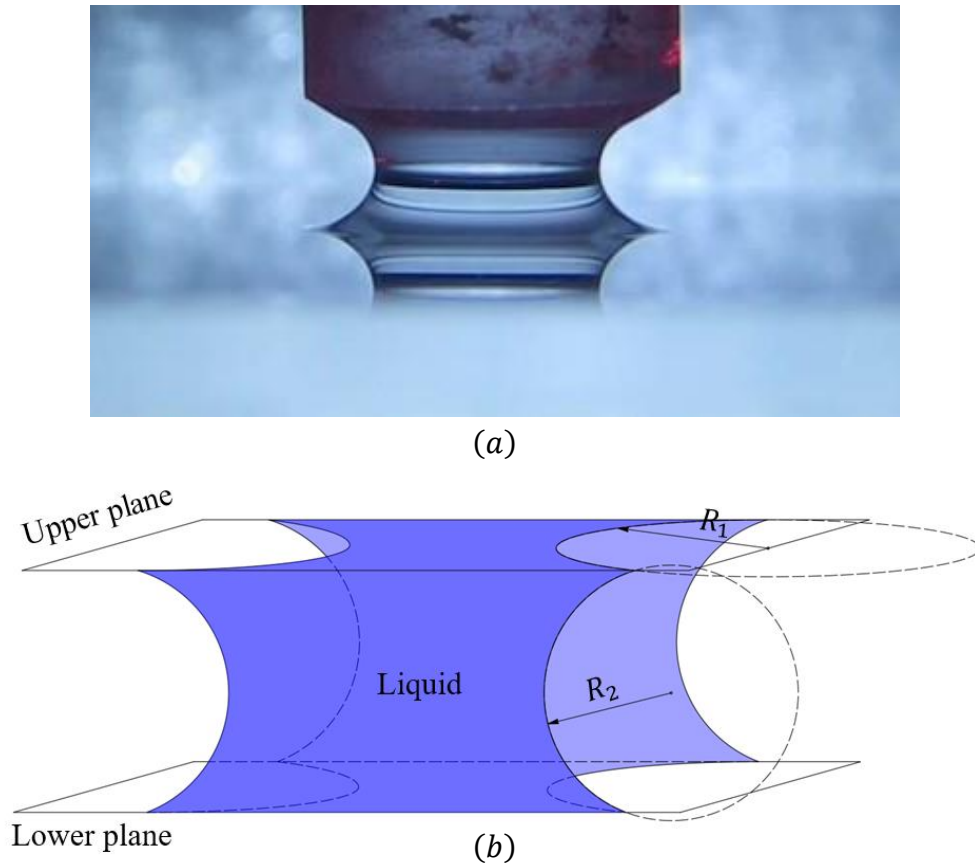


Figure 3.2 (a) Liquid bridge observed by side view method when the liquid is water. (b) Schematic diagram of the liquid bridge when the contact area is not round.

3.2 Calculation of cross-linking adhesive force

3.2.1 Calculation of Laplace pressure

When a liquid is located between two solids, the liquid forms a bridge connecting the two solids, often producing a force that attracts the solids together [11]. In this study, this force is called cross-linking adhesive force. This force is formed by the difference between the pressure inside and outside of the meniscus curved surface. The cross-linking adhesive force is produced by two forces, one is F_L due to the Laplace pressure and the other one is F_t due to the surface tension of the contact surface of the liquid bridge [11]. Therefore, the cross-linking adhesive force is affected by the surface tension of the liquid, the wettability of the liquid, etc.

As shown in Figure 3.3, is a schematic diagram of liquid bridge. The equation for calculating Laplace pressure is shown as follows:

$$F_L = \sigma \left(\frac{1}{R_1} + \frac{1}{R_2} \right) S \quad (3 - 1)$$

In equation (3 - 1), the meaning of the various symbols represent are as follows:

σ : Surface tension of the liquid in the vertical direction

R_1 : The radius of the cross-section where the thinnest place of the liquid column

R_2 : The radius of the circle where the meniscus curve lies

S : The area of the cross-section where the thinnest place of the liquid column

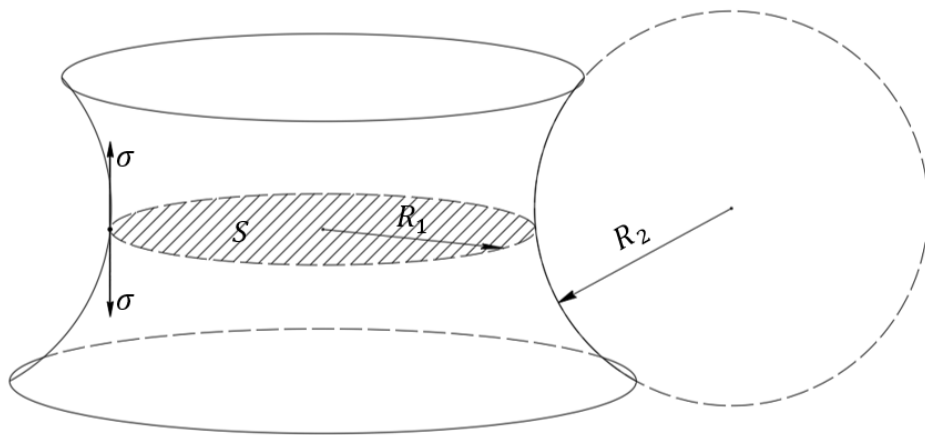


Figure 3.3 Schematic diagram of liquid bridge for calculation of Laplace pressure.

3.2.2 Calculation of wetting force

The force due to surface tension is called the wetting force in this study. The calculation of the wetting force that the spherical surface receives is shown in Figure 3.4.

The calculation equation for the vertical wetting force on the spherical surface at this moment is as follows [9]:

$$F_{t1} = 2\pi\sigma R \sin \beta \sin \alpha = 2\pi\sigma R \sin \beta \sin(\theta_1 + \beta) \quad (3 - 2)$$

In equation (3 - 2), the meaning of the various symbols represent are as follows:

α : On the spherical surface, the angle between liquid surface and horizontal plane

β : The angle describes the position of the contact line on the spherical surface

θ_1 : The contact angle of the liquid on the spherical surface

Similar to the method of calculating the wetting force of the spherical surface part, when calculating the wetting force of the glass substrate, the liquid-wetted area is approximately regarded as a part of the spherical surface with an infinite radius R . At this moment, the angle β is infinitely close to 0° , then $R \sin \beta = r$. So the equation for calculating the adhesion of the glass substrate is as follows:

$$F_{t2} = 2\pi\sigma R \sin \beta \sin \alpha = 2\pi\sigma r \sin \theta_2 \quad (3 - 3)$$

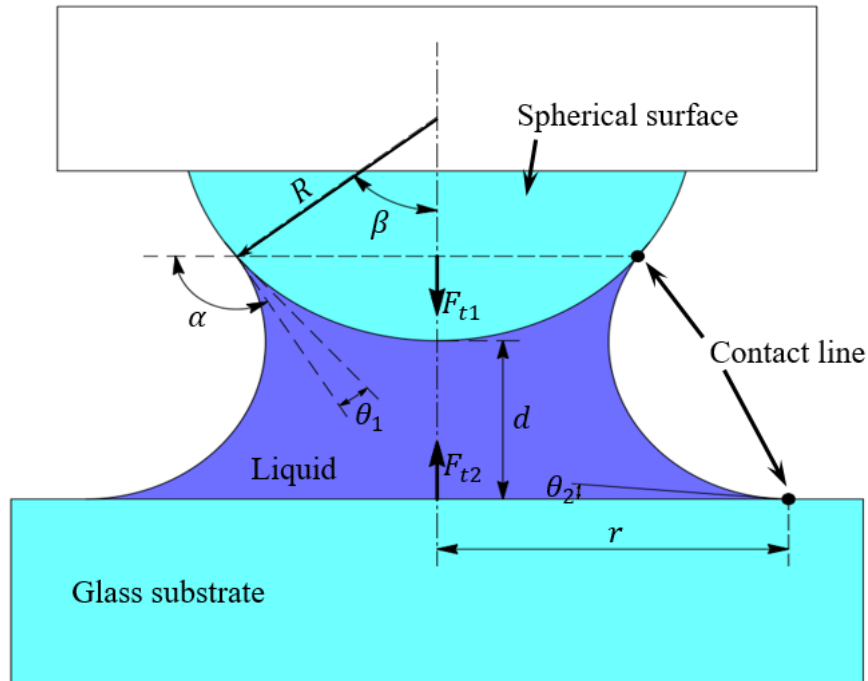


Figure 3.4 Schematic diagram of liquid bridge for calculation of wetting force. F_{t1} is the downward wetting force, F_{t2} is the upward wetting force, and θ_2 is the contact angle between the liquid and the surface of the glass substrate.

3.3 Facilities and calibrations

3.3.1 Experimental facilities

As shown in Figure 3.5, it is a schematic diagram of the measurement part of the experimental facilities. Figure 3.5 (a) is the front view, and Figure 3.5 (b) is the top view. We can see from Figure 3.5 (a) that all the experimental facilities are fixed on the bread board, and the bread board is placed on the vibration isolator. The distance and force measurement part of the experimental facility is located at the upper side, and the observation part of total reflection is located at the lower side. The capacitive displacement meter and the double cantilever spring are fixed on a Z axis motorized stage that can move up and down, and their vertical height is measured by an eddy current displacement sensor. The above four facilities are fixed on the X axis motorized stage. The total reflection part is the same as the method mentioned in section 2.2.4, that is, the laser goes through the beam expander and is reflected by the mirror, and the incident angle of $\theta_i = 60^\circ$ (as shown in Figure 2.5) is irradiated into the dove prism. Total reflection occurs at the interface between the glass substrate and the air. And then the laser illuminates into the camera 1.

The spherical lens is fixed on the double cantilever spring. Liquid bridge is formed between the spherical lens and the glass substrate. Control the Z axis motorized stage to move up and down, and measure the deformation of the double cantilever spring due to the cross-linking adhesive force through the capacitive displacement sensor, so as to accurately measure the magnitude and change of the cross-linking adhesive force. In the process of measuring the cross-linking adhesive force of the liquid bridge, the wetting behavior of liquid on the glass substrate is also recorded by the camera 1. At the same time, the liquid bridge is also observed by the camera 2 located on the side by using the side view method.

Figure 3.6 shows a schematic diagram of the entire experimental facilities. The movements of the X axis motorized stage and the Z axis motorized stage are controlled by a computer through a stage controller. The displacement signal detected by eddy current displacement sensor is first transmitted to the sensor monitor, then the signal is collected and processed by the data logger, and finally the signal data is transmitted to the computer. The displacement signal detected by the capacitive displacement sensor also goes through the same process, and finally the signal data is transmitted to the computer by the data logger. After the experiment is completed, the measured digital signal is converted into data of distance and force, and then synchronized with the data measured by camera 1 and camera 2, then the experimental result can be analyzed.

The liquids used in this experiment are water, ethanol and decane. The specification of liquids are shown in Table 3.6. Before each new experiment, the glass substrate is replaced

with a new one.

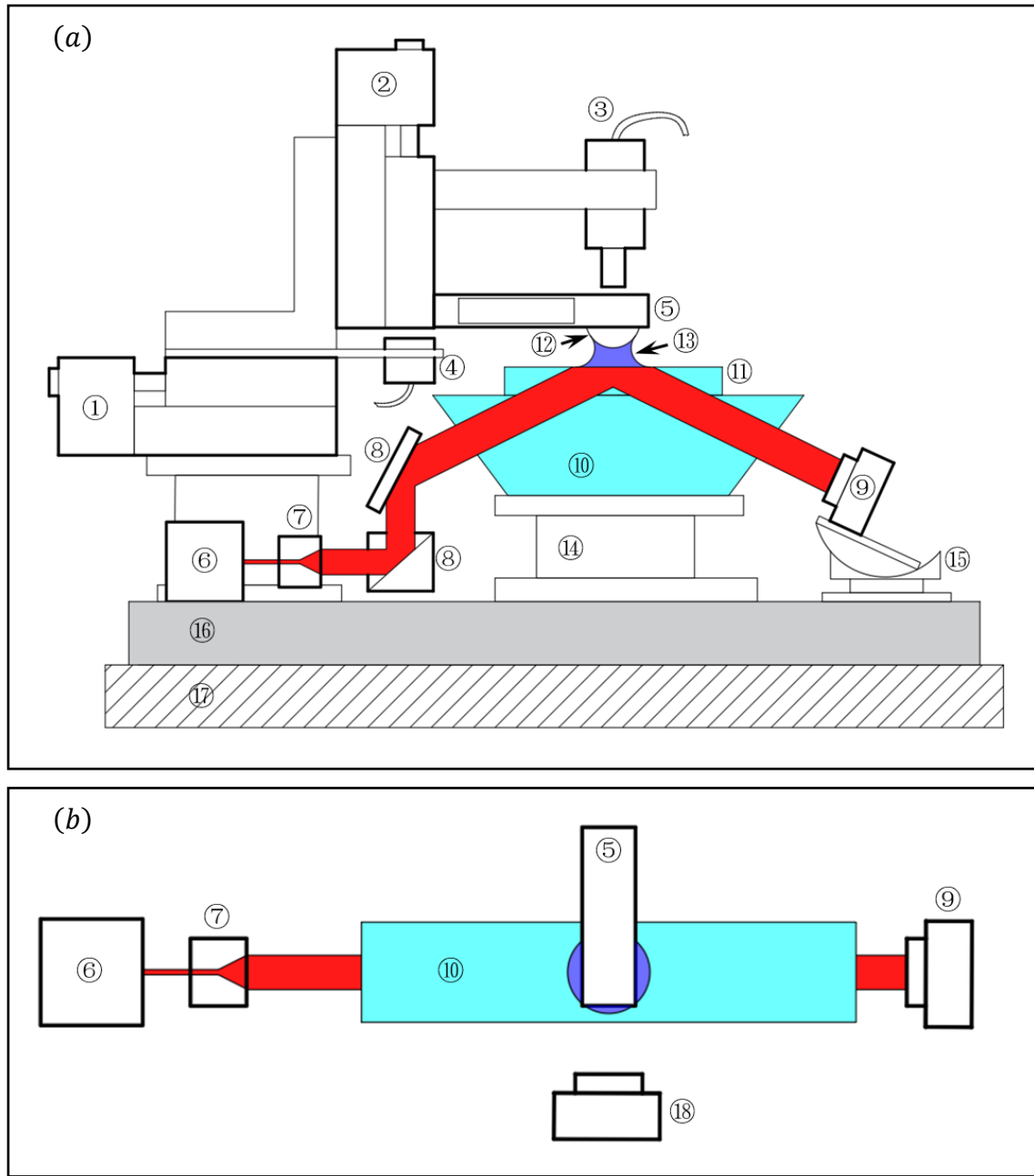


Figure 3.5 Schematic diagram of the measurement part of the experimental facilities. Figure 3.5 (a) is the front view, and Figure 3.5 (b) is the top view. Symbol ①~ ⑱ represent: ①X axis motorized stage, ②Z axis motorized stage, ③capacitive displacement sensor, ④eddy current displacement sensor, ⑤ double cantilever spring, ⑥laser, ⑦beam expander, ⑧mirror, ⑨camera 1, ⑩dove prism, ⑪glass substrate, ⑫spherical lens, ⑬liquid, ⑭Z axis stage, ⑮ α axis stage, ⑯bread board, ⑰vibration isolator, ⑱camera 2.

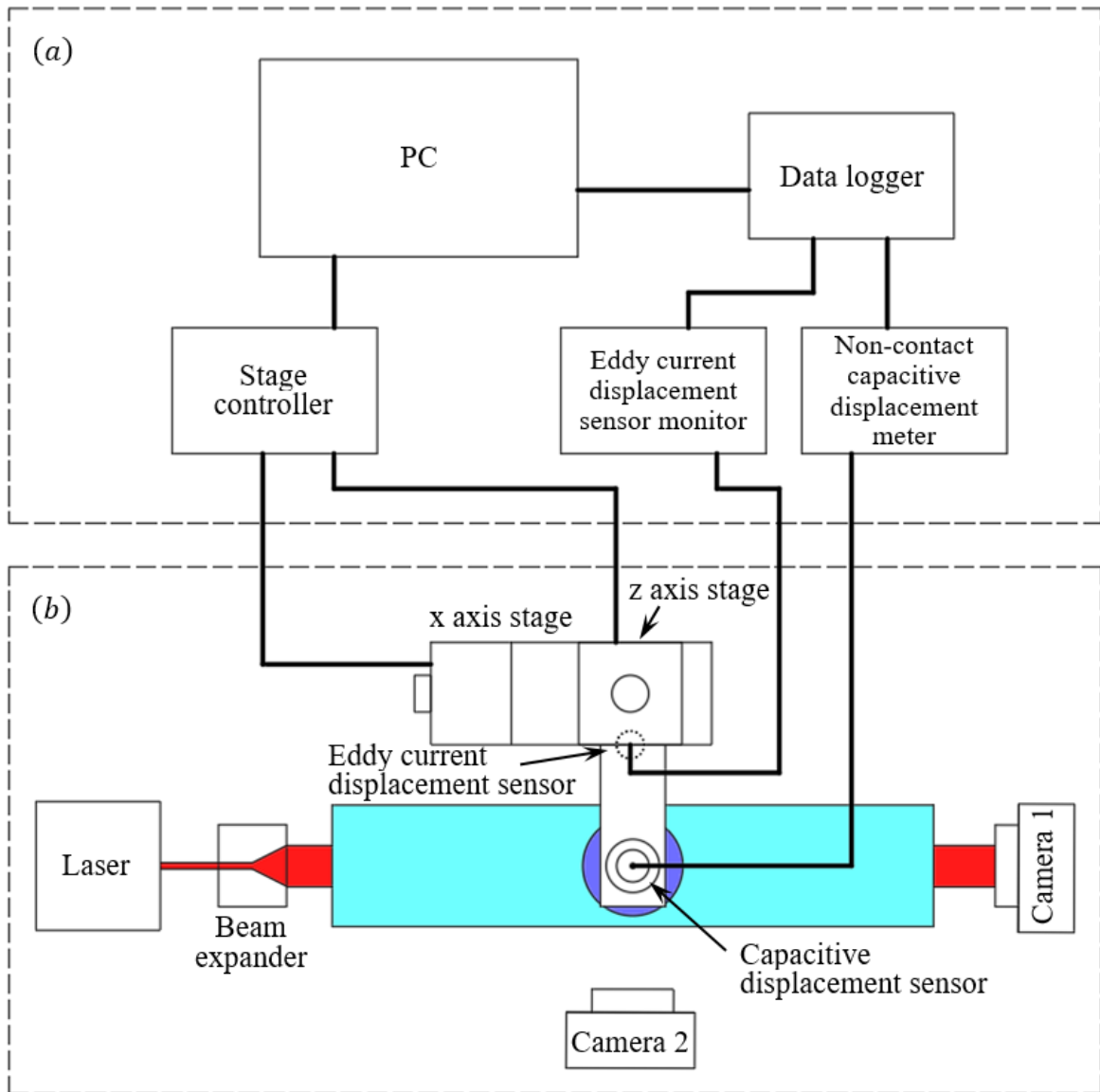


Figure 3.6 Schematic diagram of the entire experimental facilities. Figure 3.6 (a) is the information collection and processing part. Figure 3.6 (b) is the observation and measurement part.

The parameters of the experimental facilities are shown blow:

Camera 1:

Table 3.1 Specification of Nikon 1 V3

Effective Pixels	18.39 million pixels
Image sensor	13.2×8.8 mm size CMOS sensor, Nikon CX format

*data from the product manual

Camera 2:

Table 3.2 Specification of RICOH optio wg-2

Effective Pixels	16 million pixels
Image sensor	1/2.3 type CMOS

*data from the product manual

Z axis motorized stage:

Table 3.3 Specification of SGSP15-10(Z)

Amount of movement	10 mm
Table surface size	40×40 mm
Resolution (Full)	2 μm /pulse
Resolution (Half)	1 μm /pulse
Max speed	15 mm/sec
Positioning accuracy	10 μm
Repeated positioning accuracy	5 μm
Load capacity	29.4 N (3.0 kgf)

*data from the official website: <https://www.global-optosigma.com>

Stage controller:**Table 3.4** Specification of SHOT-102

GP-IB	Yes
Maximum set movement amount	16,777,214 pulse
Maximum drive speed	20,000 pps
Minimum drive speed	100 pps
Acceleration and deceleration time	0~1,000 ms

*data from the official website: <https://www.global-optosigma.com>

Eddy current displacement sensor:**Table 3.5** Specification of KEYENCE EX-11

Model	EX-110V
Amplifier unit	EX-V02
Range of measurement	0~2 mm
Display range	-19,999~19,999
Precision	±0.3% of F.S.
Resolution (average of 64 times)	0.4 μm
Sampling rate	Up to 40,000 times/sec

*data from the official website: <https://www.keyence.co.jp>

Liquids**Table 3.6** Specification of liquids

20°C	Surface tension, mN/m	Density, kg/m ³	Viscosity, mPa · s
Water	72.7	997	1.002
Ethanol	22.4	789	1.2
Decane	22.8	730	0.838

Capacitive displacement sensor:**Table 3.7** Specification of IWATSU ST-0536A

Model	ST-0536A
Sensitivity	0.5V/ μm
Range of measurement	20~ 40 μm
Precision	$\pm 2\%$ of F.S.
Resolution (1kHz)	1 nm

*data from the official website: <http://www.iti.iwatsu.co.jp>

Data logger:

In this experiment, the data collected from ST-3511 and EX-11 displacement sensor is input to GL7000 data logger. The data logger can be controlled by the PC and convert the voltage data into a CSV file and save it. In this experiment, we performed experiments at a sampling frequency of 1 kHz.

Table 3.8 Specification of DATA PLATFORM GL7000

Model	GL7000
Analysis frequency	0.08 • 0.2 • 0.4 • 0.8 • 1.6 • 2 • 3.2 • 4 • 8 • 20 • 40 • 80 • 200 • 400 • 800Hz、 2 • 4 • 8 • 20 • 40 • 80 • 200 • 400kHz
Number of analysis points	500 • 1000 • 2000 • 4000 • 10000
Average processing	Arithmetic average, indexed average, peak hold
Analysis CH	4ch
Analysis function	Y-T, linear, power, PSD, cross, transfer function, coherence, COP

*data from the official website: <https://www.graphtec.co.jp>

Glass substrate:

In this experiment, we take the Matsunami Glass Industry FF-0044 fine frost slide glass as the glass substrate. The surface roughness of the slide glass is Ra 0.02 μm .

Table 3.9 Specification of Matsunami Glass Industry FF-004 fine frost slide

Model	Frost color	Size (mm)	Thickness (mm)	Frost size (mm)
FF-004	Blue	76×26	0.9~1.2	15×26

*data from the official website: <http://www.matsunami-glass.co.jp>

Spherical lens:

A SIGMAKOKI SLB-05-08P spherical glass lens is attached to the vibrating part of the double cantilever spring to form a liquid bridge with the glass substrate.

Table 3.10 Specification of SIGMAKOKI SLB-05-08P spherical glass lens

Outer diameter	5 mm
Focal length	8 mm
Edge thickness	1.4 mm
Center thickness	2.3 mm
Back focus	6.5 mm
curvature radius	4.15 mm
Eccentricity	$< 3^\circ$

*data from the official website: <https://www.global-optosigma.com>

Vibration isolator:

During the experiment, the spring may vibrate due to the influence of the surrounding environment as well as the external force. In order to minimize the effect of the environment on the experimental result, the entire experimental facilities are placed on the AY-1510K4 steel honeycomb surface plate air spring type vibration isolator. Figure 3.7 shows the graph of voltage on function of time when the spring vibrates freely on the vibration isolator. The blue line is the graph when the vibration isolator is not activated, and the red line is the graph when the vibration isolator is activated. Since the influence of the environment can be obviously suppressed when the vibration isolator is activated, all experiments are performed with the vibration isolator activated.

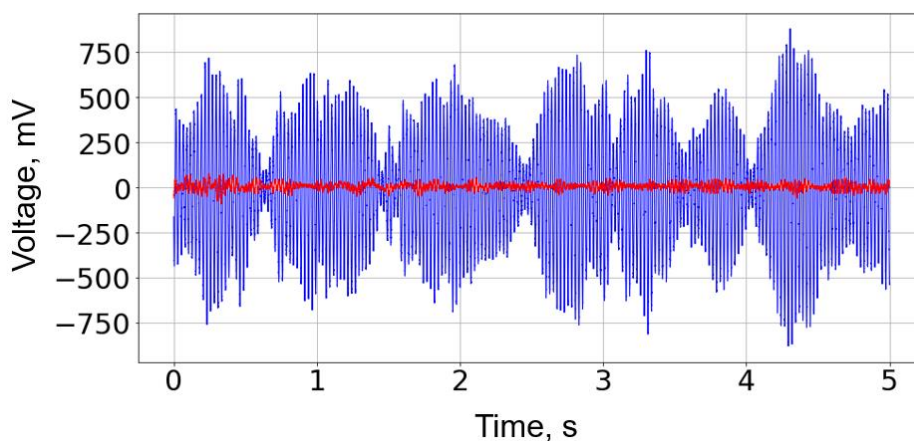


Figure 3.7 Graph of voltage on function of time when the spring vibrates freely on the vibration isolator.

Table 3.11 Specification of AY-1510K4 steel honeycomb surface plate air spring type vibration isolator

Item/Model	AY-1510K4
Natural frequency	Vertical: 1.5Hz Horizontal: 1.8Hz
Vibration isolation method	Vertical: Diaphragm air spring Horizontal: Parallel swing mechanism
Damping method	Vertical: Air damping using variable orifices Horizontal: Special damping using the α -GEL
Load weight	300 kg
Table dimensions (mm)	1500×1000
Air supply	0.35~0.70MPa

*data from the official website: <http://www.meiritz.jp>

3.3.2 Calibration of double cantilever spring

The spring constant of the double cantilever spring is calibrated for the accuracy of force measurement. Figure 3.8 shows the image of capacitive displacement sensor and double cantilever spring.

First, fix the double cantilever spring and ST-0536A type capacitive displacement sensor. Start recording the signal of the displacement sensor and give a shock to the double cantilever spring. When the natural vibration of the double cantilever spring subsides, the displacement sensor stops recording.

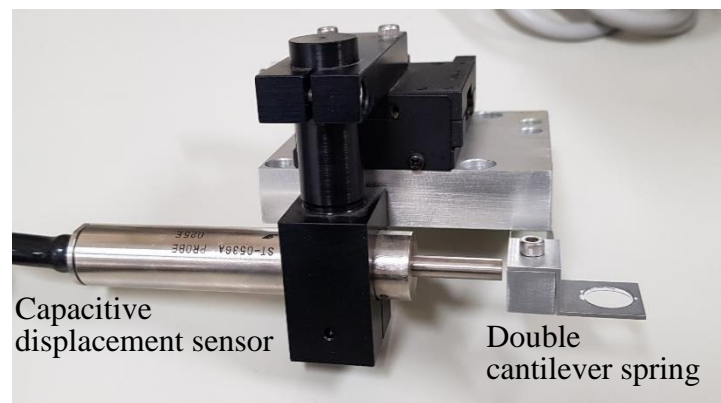


Figure 3.8 Image of capacitive displacement sensor and double cantilever spring.

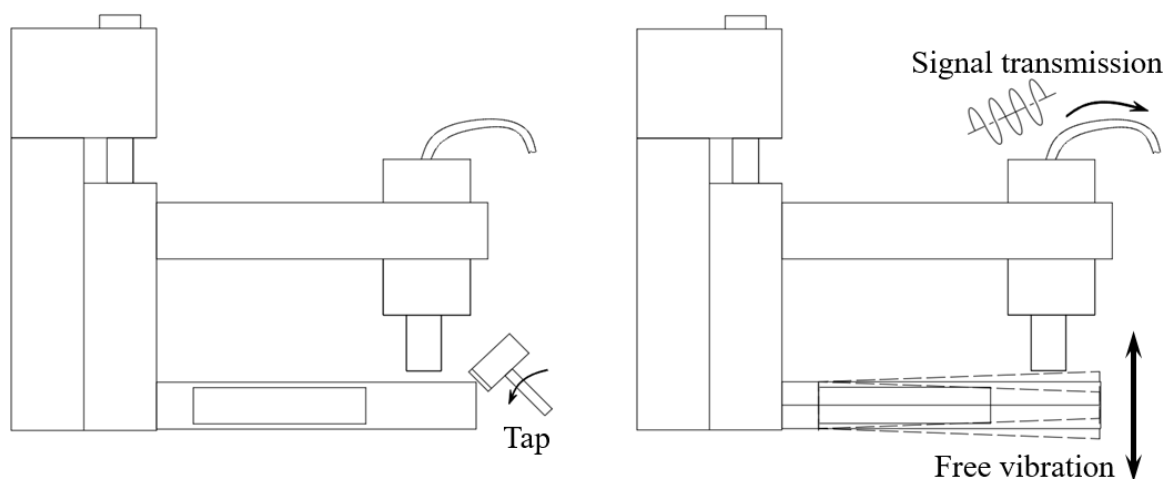


Figure 3.9 Schematic diagram of free vibration experiment of double cantilever spring.

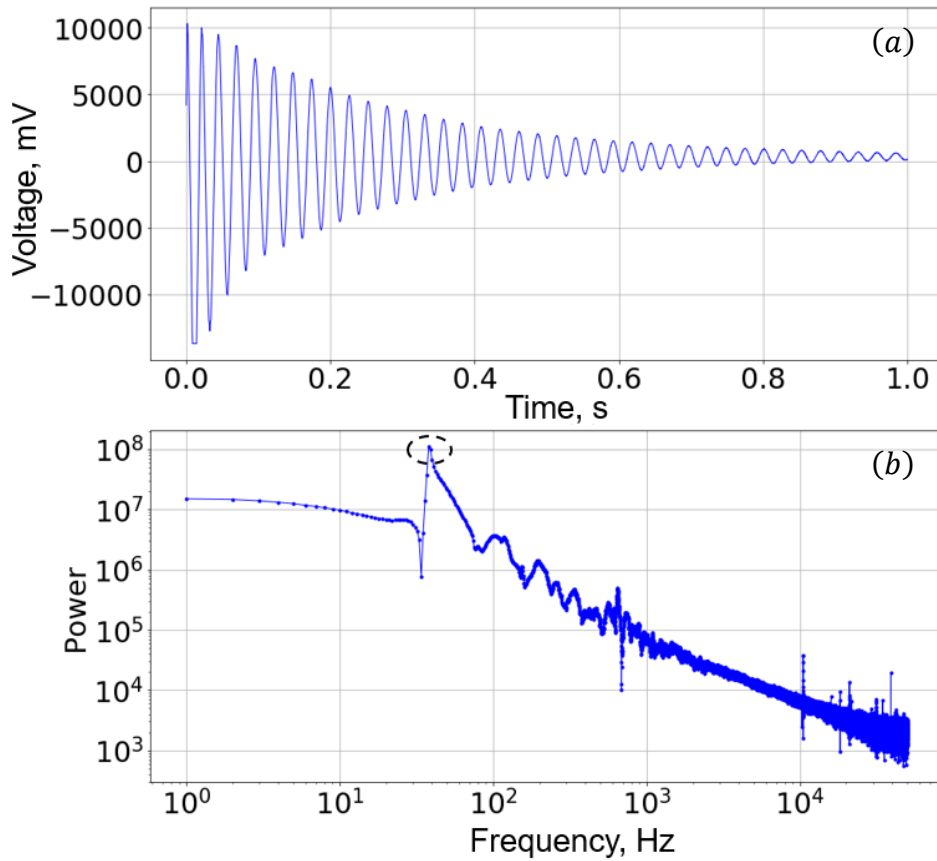


Figure 3.10 Result of free vibration experiment of double cantilever spring. Figure 3.10 (a) is graph of voltage on function of time and Figure 3.10 (b) is the graph after Fourier transform. The highest point (peak) in Figure 3.10 (b), where the black dashed circle lies, is the natural frequency of vibration.

As shown in Figure 3.10, is the result of free vibration experiment of double cantilever spring. Figure 3.10 (a) shows the relationship between the voltage of the displacement sensor and time, when the double cantilever spring is shocked. Figure 3.10 (b) shows the graph after the Fourier transform of the voltage data. The horizontal axis is the frequency and the vertical axis is the intensity at that frequency. One peak appears in the Fourier transform graph. This peak is considered to be the natural frequency of the double cantilever spring.

The theoretical calculation of the natural frequency of the spring has an equation:

$$f = \frac{1}{2\pi} \sqrt{\frac{k}{m}} \quad (3 - 4)$$

In Equation (3 – 4), the parameters are as follows:

f : Natural frequency of the spring

k : Spring constant

m : Mass of vibration part of spring

The natural frequency of spring can be get from Figure 3.10, but the mass of vibration part of spring is unknown.

Therefore, the experiment is performed two times with different masses, as shown in Figure 3.11. The spring constant can be calculated by the following equations:

$$f_1 = \frac{1}{2\pi} \sqrt{\frac{k}{m + m_1}} \quad (3 - 5)$$

$$f_2 = \frac{1}{2\pi} \sqrt{\frac{k}{m + m_2}} \quad (3 - 6)$$

In the equations:

f_1 : Natural frequency when the mass of m_1 is added

f_2 : Natural frequency when the mass of m_2 is added

k : Spring constant, the same with k in Equation (3 – 4)

According the results of the two experiments, the spring constant calculated by Equations (3 – 5) and (3 – 6) is $k = 333.0 \text{ N/m}$.

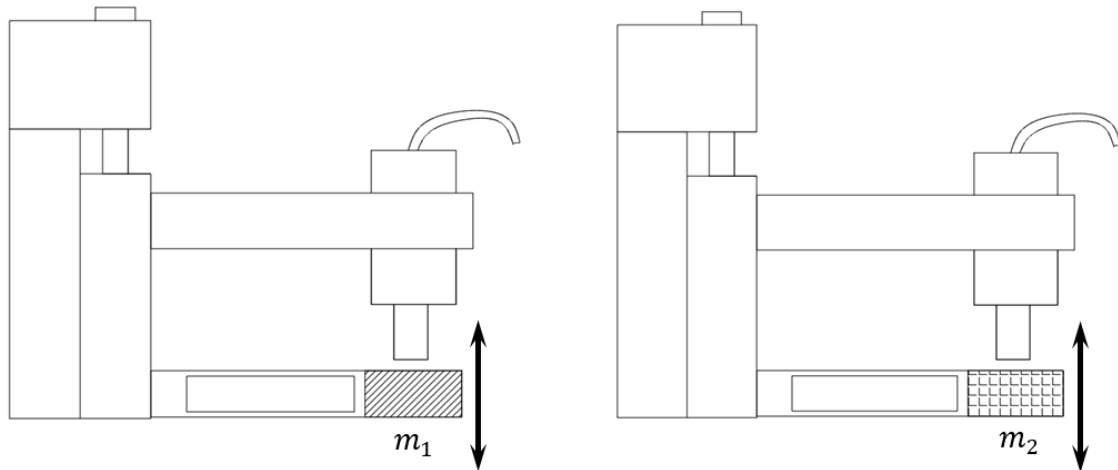


Figure 3.11 Schematic diagram of two experiments of spring free vibration with mass m_1 and mass m_2 added.

In theory, the spring constant can also be calculated by using the following equation according to the material parameters:

$$k = \frac{2Ebt^2}{L^2} \quad (3 - 7)$$

In the equation:

E : Young's modulus of cantilever spring material

b : Width of cantilever spring

t : Thickness of cantilever spring

L : Length of cantilever spring

The parameters of E , b , t and L of the double cantilever spring are 68.3 kN/mm², 10 mm, 0.2 mm and 30 mm.

Substituting the above parameters into Equation (3 – 7), we can get $k=404.7$ N/m. This result is similar to the experimental result 333.0 N/m. Taking into account the flatness of the spring surface and the environmental factors during the experiment, we think that the actual spring constant of the double cantilever spring should be closer to the experimental value.

According to Table 3.7, the resolution (1kHz) of the capacitive displacement sensor is 1 nm, so that, in this experiment the measurement resolution of force is 0.333 μ N.

3.4 Experimental procedure

The experiment of liquid bridge has the process of approaching, contact and separation, as shown in Figure 3.12. First, before the process of contact, make the lens approach the glass substrate and find the distance that make sure the liquid can contact with the glass substrate. And, set the distance as d_0 . Move back a distance of Δd , and set the present position as the original position. Then the liquid is attached to the spherical lens, and adjust the capacitive displacement sensor to the zero state. Then the Z axis motorized stage is controlled to make the cantilever spring and the spherical lens as a whole approach the glass substrate. When the lens reaches the set distance d_0 , liquid comes into contact with the glass substrate, the Z axis motorized stage stops moving and stands still for 5 seconds. Then move away from the glass substrate, and stop moving after the liquid bridge breaks.

According to Table 3.4, the amount of movement per pulse of the motorized stage U_{rh} is $1\text{ }\mu\text{m}$ and the minimum drive speed of the controller P_{mini} is 100 pps. Therefore, the minimum moving speed of the actuator and the corresponding settable speed interval can be calculated as follows:

$$U_{mini} = U_{rh} \cdot P_{mini} = 100\text{ }\mu\text{m/s}$$

The speed of the Z axis motorized stage is set to $300\text{ }\mu\text{m/sec}$. Experiments are performed in an environment with a temperature of $25\pm 1^\circ\text{C}$ and a humidity of $77\pm 2\%$.

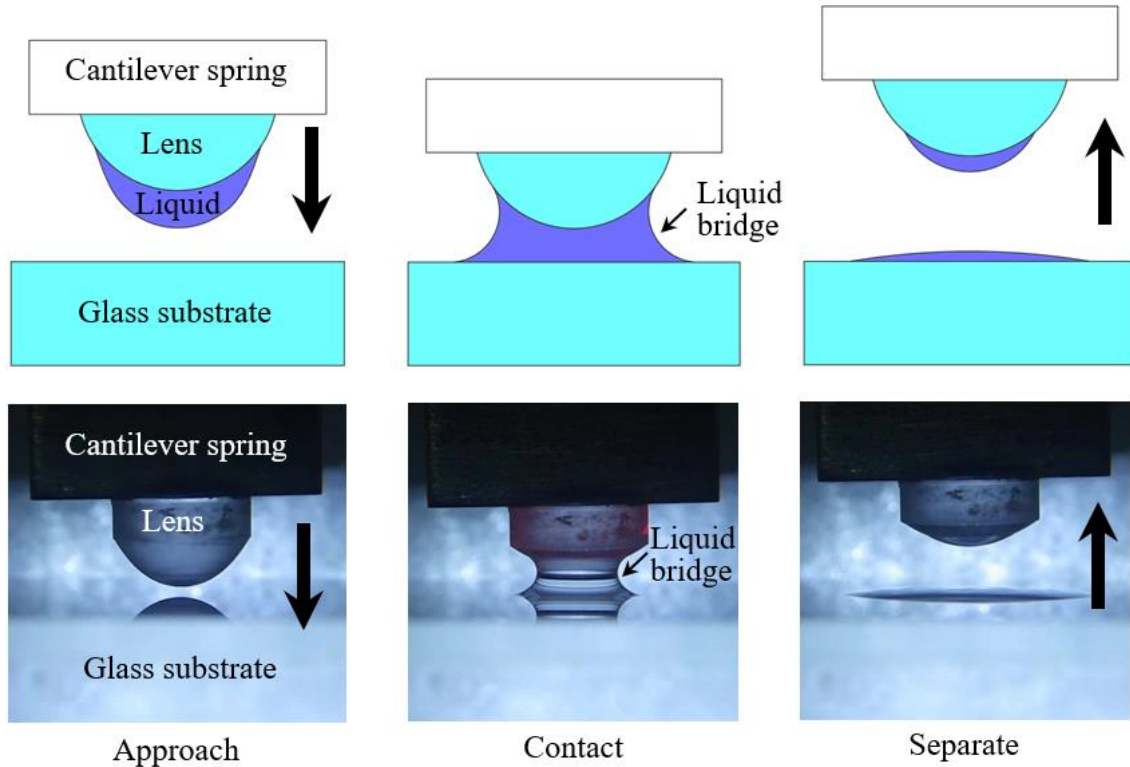


Figure 3.12 Schematic diagram and observing image of the experimental procedure of liquid bridge (decane).

(I) Measuring for the cross-linking adhesive force

The relationship between the cross-linking adhesive force and the distance between the two surfaces of the spherical lens and the glass substrate in the contact separation process is investigated. The cross-linking adhesive force calculated from voltage data can be expressed by the following equation:

$$F = \Delta U_1 a_1 k \quad (3 - 8)$$

In Equation (3 – 8) the parameters are:

F : Cross-linking adhesive force calculated from voltage data

ΔU_1 : Change in voltage of capacitive displacement sensor

a_1 : Relationship between voltage of capacitive displacement sensor and distance between double cantilever spring and capacitive displacement sensor

k : Spring constant

The vertical height of the Z axis motorized table is measured by the eddy current displacement sensor. The calculation equation of the distance is as follows:

$$d = \Delta U_2 a_2 \quad (3 - 9)$$

In Equation (3 – 9) the parameters are:

d : Distance between spherical lens and glass substrate

ΔU_2 : Change in voltage of eddy current displacement sensor

a_1 : Relationship between voltage of eddy current displacement sensor and distance between Z axis motorized table and eddy current displacement sensor

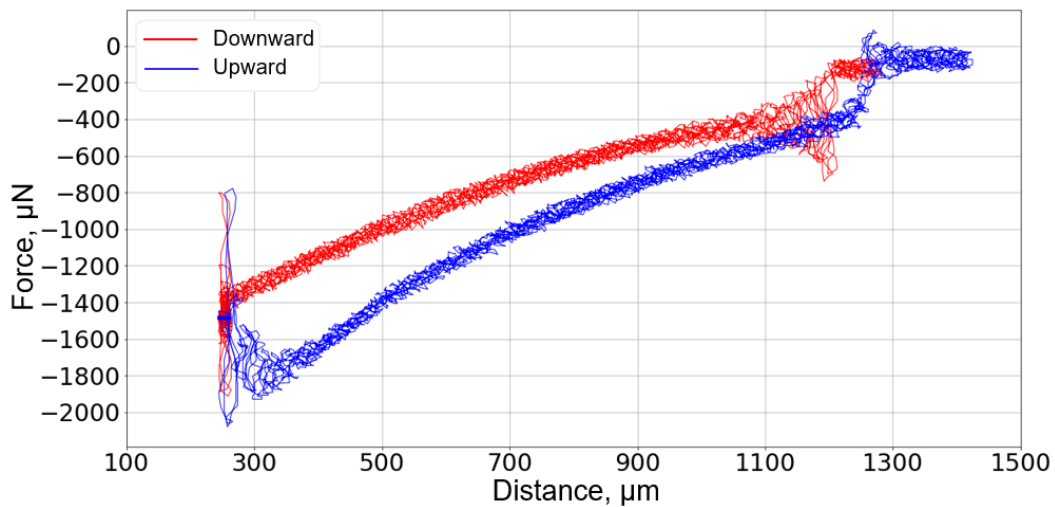


Figure 3.13 Diagram of force on function of distance from experimental result of liquid bridge (water). The time scale of data recording is 1 ms.

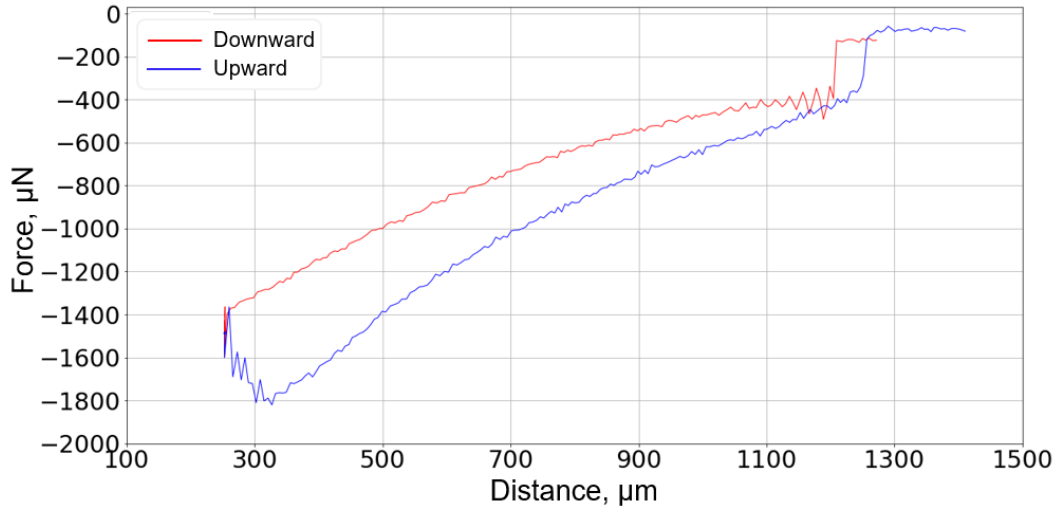


Figure 3.14 Diagram of force on function of distance from experimental result of liquid bridge (water) after a time averaging of 20 ms.

As shown in Figure 3.13, is the diagram of cross-linking adhesive force on function of distance from experimental result of liquid bridge when the liquid is water. And the time scale of data recording is 1 ms. In figure 3.13, the red line represents the process when the spherical lens approach the glass substrate (downward) and the blue line represents the process when the spherical lens moves away (upward). Obviously, due to the extremely small time scale of the data recording, there are too much noise in the figure, which is not convenient for intuitive observation of the result. Therefore, we performed a time averaging of 20 ms, and the result is shown in Figure 3.14. The force-distance relationship in this figure becomes easier to observe.

(II) Observation for the wetting radius and meniscus

The wetting radius at the glass substrate is observed according to the side view method and total reflection method. As shown in Figure 3.15 (a), is the image of liquid bridge (ethanol) taken by camera 2. The wetting radius r can be measured directly. For the total reflection method, the method of reading the wetting radius is the same as that shown in Figure 2.26 in section 2.5. Figure (b), (c) and (d) are the wetting images of ethanol, decane and water taken by camera 2. The wetting images of decane and water are almost the same that radius r can be observed directly. Only when the liquid is ethanol, there are two radius, outer radius r_o and inner radius r_i , appeared.

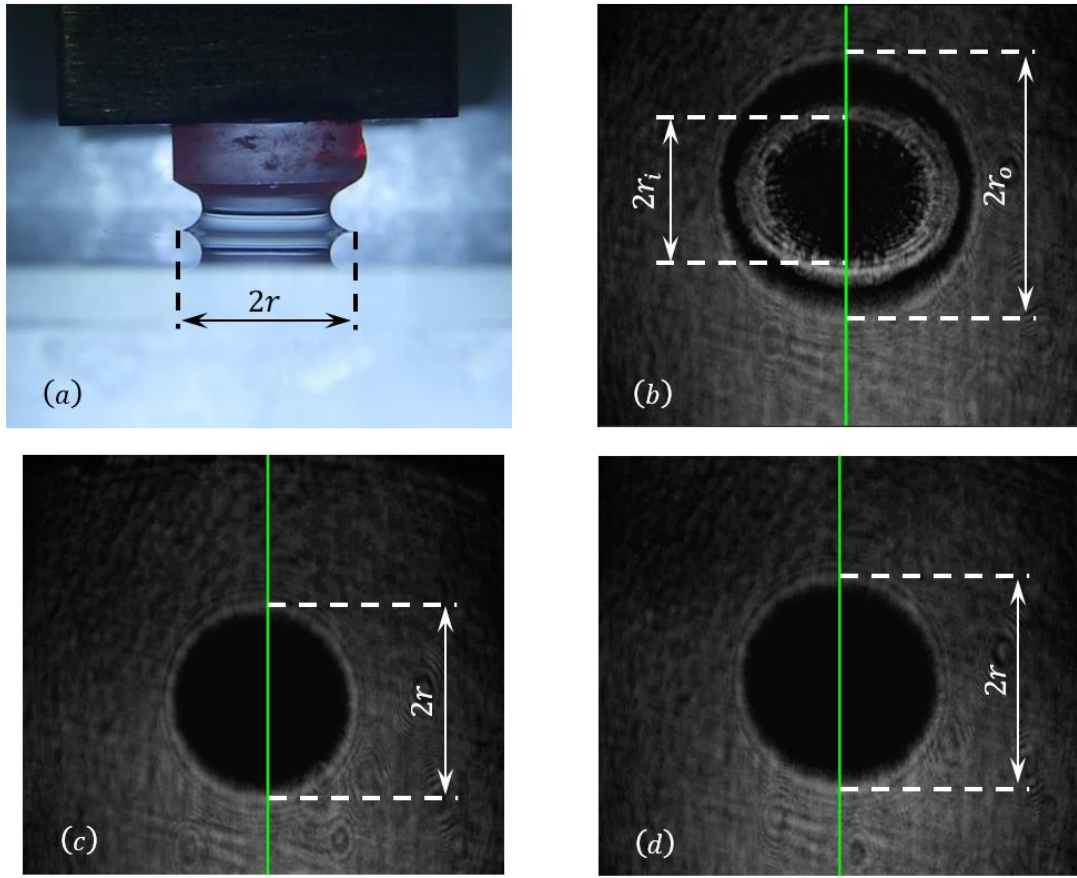


Figure 3.15 Diagram of measuring the wetting radius. Figure 3.15 (a) is the image of liquid bridge (ethanol) observing by side view method. Figure 3.15 (b), (c) and (d) are the wetting images of ethanol, decane and water observing by total reflection method.

When the liquid is ethanol, the radius R_1 of the cross-section of the thinnest part of the liquid bridge and meniscus curvature radius R_2 can be measured in Figure 3.16 (a). And the contact angle θ_2 can be measured in Figure 3.16 (b). When measuring the contact angle θ_2 , first, it is necessary to fit a circle O_3 according to the outline curve of the liquid surface near the contact line, and then draw a perpendicular O_3B from the circle center O_3 to the plane of the glass substrate. Connect the point A on the contact line and the circle center O_3 . The angle θ'_2 between line AO_3 and line O_3B is equal to the contact angle θ_2 . And the angle θ'_2 can be calculated by the radius R_3 and the length of perpendicular O_3B .

When calculating the Laplace pressure, it can be obtained by substituting the values of R_1 , R_2 , surface tension σ of the liquid and the area of the surface where R_1 is located, into Equation (3 – 1). The wetting force on the glass substrate can be calculated by using

Equation (3 – 3), and the values of the wetting radius r , surface tension σ of the liquid and contact angle θ_2 .

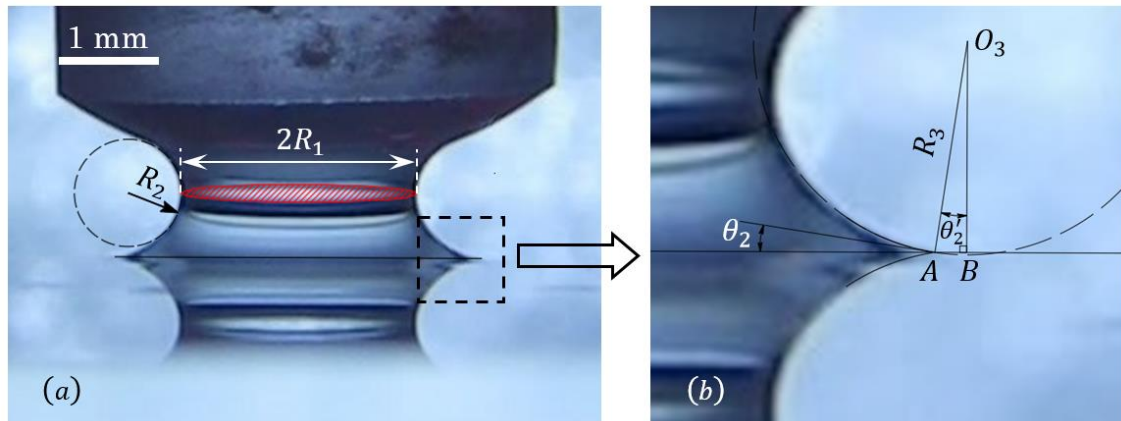


Figure 3.16 Diagram of measuring the liquid bridge radius R_1 , meniscus curvature radius R_2 and contact angle θ_2 . In Figure 3.16 (a) the red shaded area represents the cross-section of the thinnest part of the liquid bridge. And the dashed circle with radius R_2 next to the red shaded area is a circle fitted with the curve of the meniscus. Figure 3.16 (b) is a partial enlarged view of the part enclosed by the dashed square in Figure 3.16 (a). Figure 3.16 (b) shows the method of measuring the contact angle θ_2 .

3.5 Results

Figure 3.17, Figure 3.18 and Figure 3.19 are the experimental results of the liquid bridge of water, decane and ethanol respectively. Among them, (a) of each figure is a force-time relationship diagram. The recording starts before the liquid comes into contact with the glass substrate. The recording data includes the change in force in the contact process, force in the pause process, and force in the process the breaking of the liquid bridge. It can be seen that there are many small fluctuations in force curve in the figure, which affect the specific analysis of the force. To solve it, the processing method is the same as when processing the image in Figure 3.13, and the force data is time averaged for 20 ms. Comparing the force-time diagrams of these three liquids, it can be found that the graphs of decane and ethanol are very similar, and the graph of water is different. The contact time between water and the glass substrate is earlier. This is because the wettability of water to the spherical glass lens is not as good as decane and ethanol, so that, resulting in a larger contact angle and a higher height of the droplet itself.

Figure 3.17 (b), Figure 3.18 (b) and Figure 3.19 (b) are the wetting radius-time diagrams of water, decane and ethanol, respectively. In these figures, the blue lines with dot marks are the radii measured by the total reflection method, and the black lines with cross marks are the radii measured by the side view method. In Figure 3.19 (b), the blue and red lines are the radii r_o and r_i as shown in Figure 3.15 (b). From Figure 3.17 (b) and Figure 3.18 (b), it can be seen that although the radius measured by the side view method is generally consistent with the radius measured by the total reflection method, there are still some small gaps. The reason for the gap is that the side view method cannot accurately determine the contact line. The latter calculations will use the radius measured by total reflection. Unlike Figure 3.17 (b) and Figure 3.18 (b), there are two radii in figure 3.19 (b). By comparing the measurement results with the side view method, it is found that the radius r_i equals the radius r measured by the side view method. And the reason for the existence of the outer radius r_o is that there is a thin film of only several micrometers which keeps spreading out from the original contact line. And the latter calculations will be performed using the radius r_i .

Figure 3.20, Figure 3.21 and Figure 3.22 are the force-time diagrams of the experimental results of the liquid bridge of water, decane and ethanol, respectively. The force data has been processed by time averaging. The cross marks and triangle marks in the figures indicate the calculated wetting force on the glass substrate side during the downward and upward processes, respectively. The dot marks and the square marks indicate the calculated Laplace pressure in downward and upward processes, respectively. The red lines and marks in these

figures represent the data of the downward process in which the liquid contacts with the glass substrate. The blue lines and marks represent the data of the upward process in which the liquid bridge breaks.

Unlike the graphs of decane and ethanol, the lines of the two processes of the water in force-time diagram have a large difference. The reason for this difference is also that the wettability of water is not as good as the wettability of the latter two. Shortly after the beginning of the downward movement, the water contacts the glass substrate, but the spherical glass lens has not yet reached the set position. The spherical glass lens continues to move downward, forcing the water droplets to wetting more area of the glass lens surface, while at the same time the wetting radius of the water on the glass substrate keeps not changing. When the spherical glass lens moves upward, the angle β gradually becomes smaller (as shown in Figure 3.4), and the cross-linking adhesive force becomes larger due to the presence of wetting force. According to Schellenberger et al. [9], there is an angle β_m that maximizes the wetting force. In Figure 3.20, the angle β_m with the largest wetting force exists near the distance of 300 μm . When the spherical glass lens continues to move upward, the value of the angle β is gradually smaller than β_m . The value of Laplace pressure gradually decreases until the liquid bridge suddenly breaks. In the process of the liquid bridging and breaking, the Laplace pressure and the wetting force at the glass substrate are calculated based on the observing results of side view method. It can be seen that the calculated Laplace pressure is basically consistent with the measured cross-linking adhesive force.

Decane and ethanol have similar surface tension and good wettability, and the results of the liquid bridge experiment are also very similar. As shown in Figure 3.21 and Figure 3.22, after the two liquids are in contact with the glass substrate, the force-time graphs of the downward and upward processes overlap. Moreover, the calculated Laplace pressure and the measured cross-linking adhesive force are in good agreement. At the same time, the wetting force at the glass substrate is also calculated.

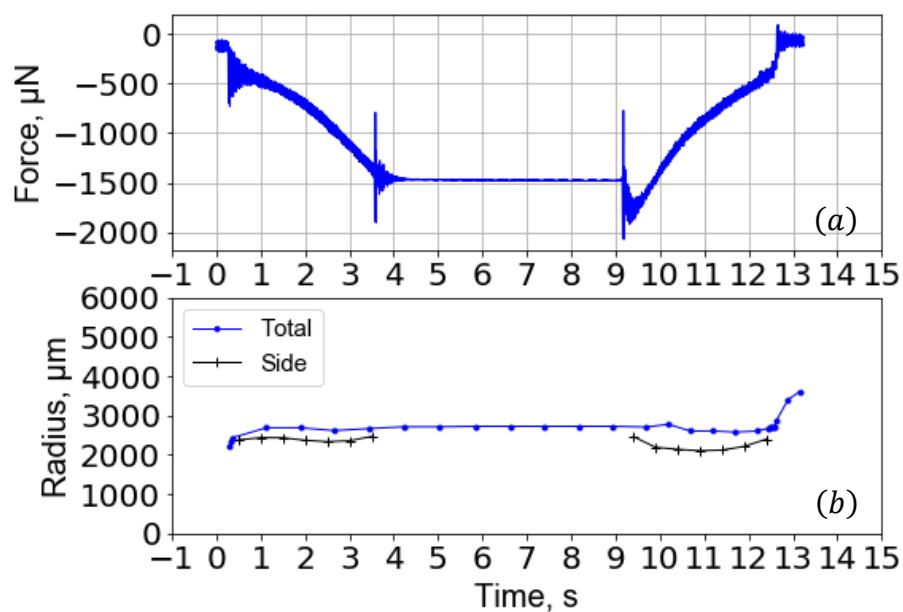


Figure 3.17 Experimental result of water (a) is diagram of cross-linking adhesive force-time. (b) is diagram of wetting radius-time.

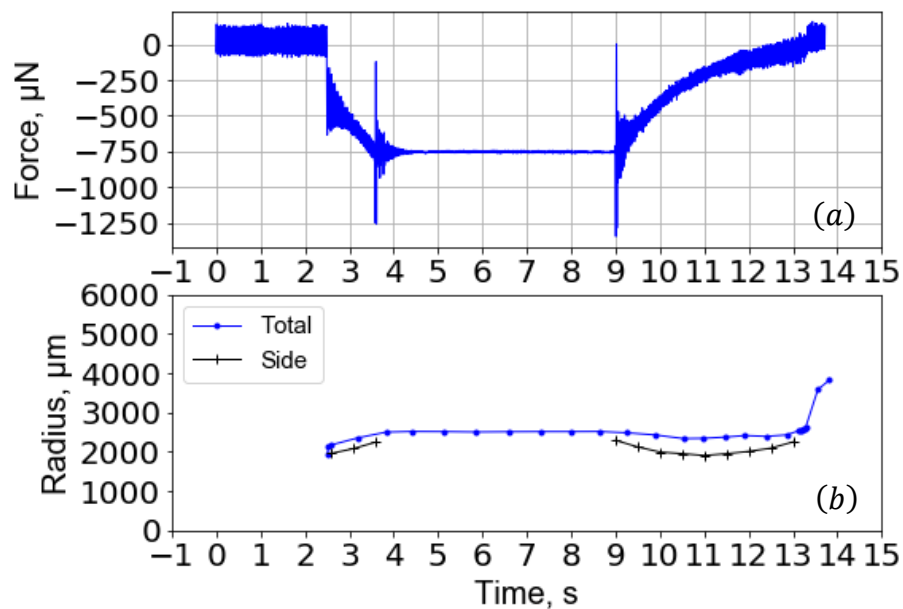


Figure 3.18 Experimental result of decane (a) is diagram of cross-linking adhesive force-time. (b) is diagram of wetting radius-time.

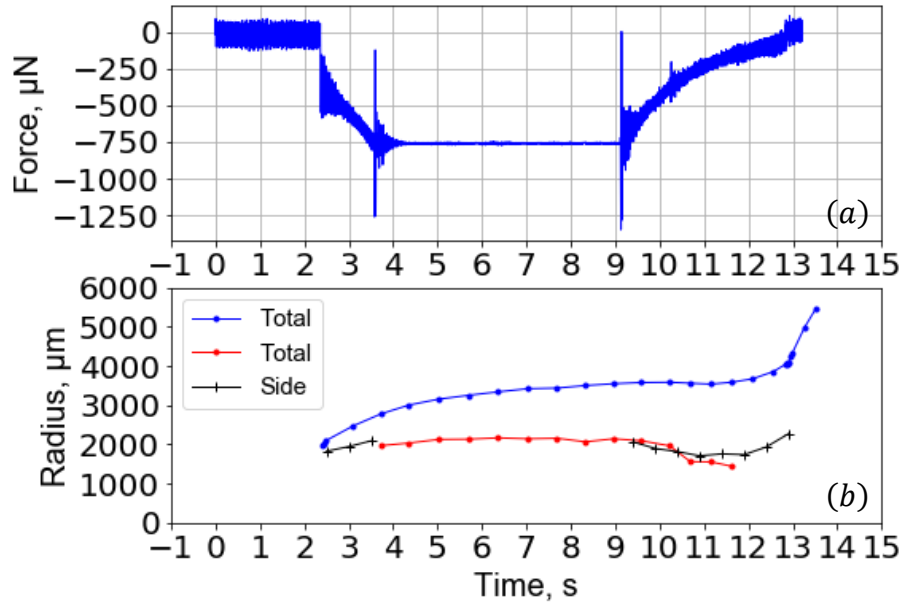


Figure 3.19 Experimental result of ethanol (a) is diagram of cross-linking adhesive force-time. (b) is diagram of wetting radius-time.

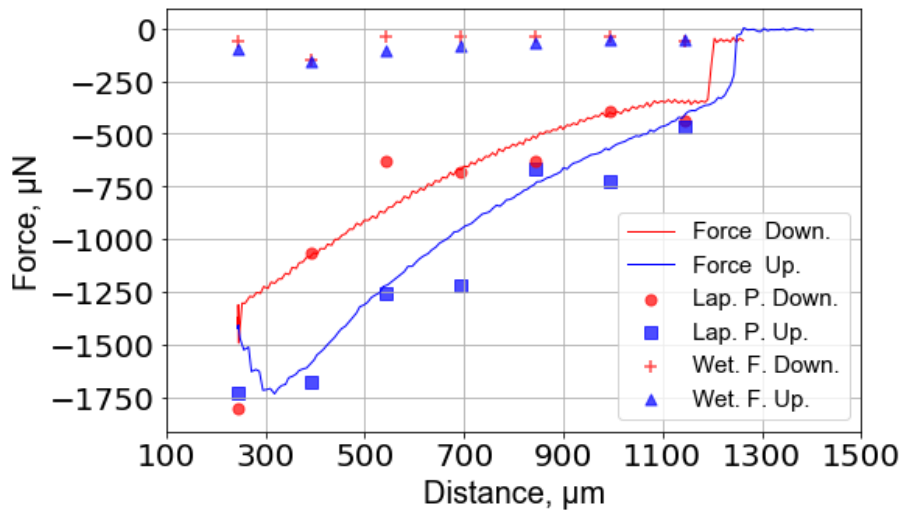


Figure 3.20 Force curve of water in experiment of liquid bridge.

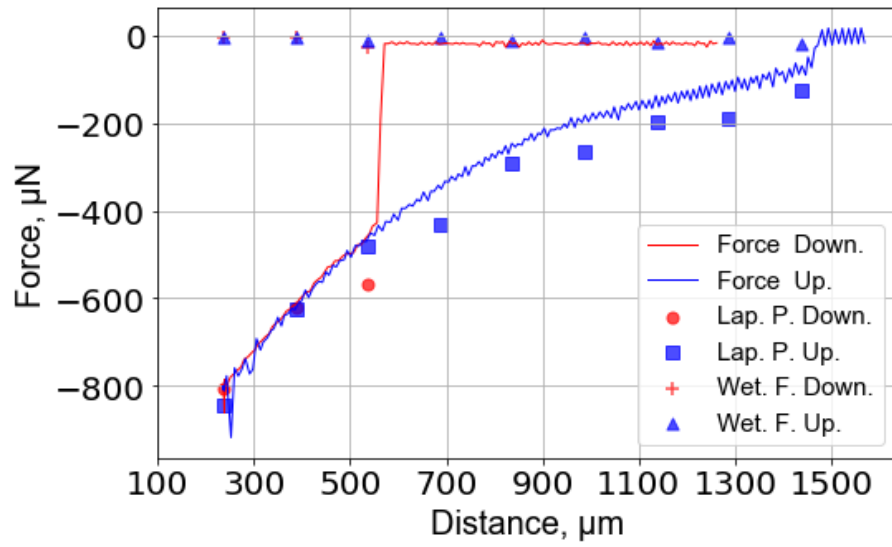


Figure 3.21 Force curve of decane in experiment of liquid bridge.

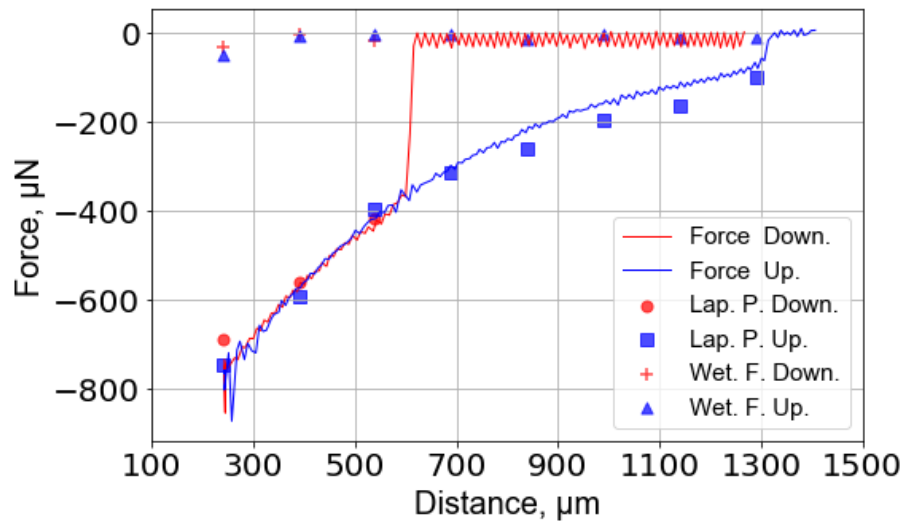


Figure 3.22 Force curve of ethanol in experiment of liquid bridge.

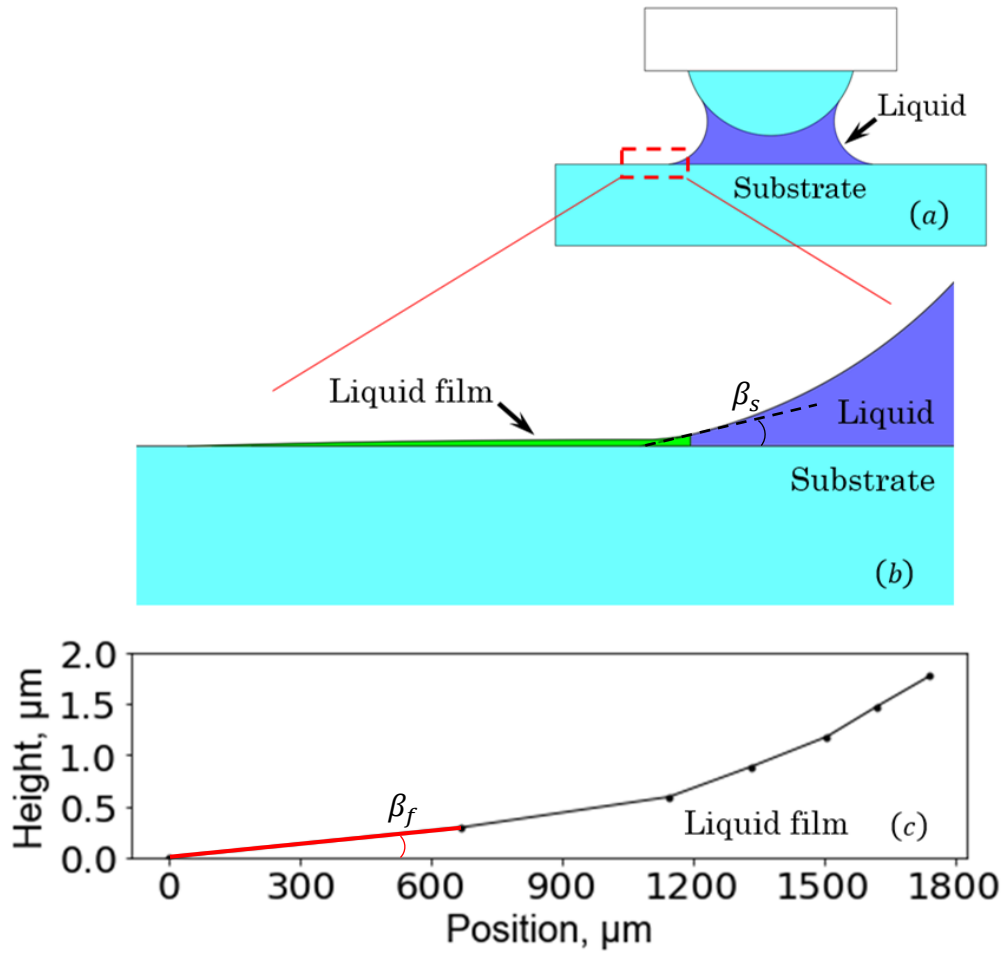


Figure 3.23 Profile of liquid film in the liquid bridge when the liquid is ethanol. Figure 3.23 (b) is a partial enlarged view of Figure 3.23 (a). In Figure 3.23 (b), the green part is the liquid film, and β_s is contact angle measured by side view method. Figure 3.23 (c) is the surface profile of liquid film calculated by fringe method. The inclination angle β_f of the red line segment is the contact angle of the liquid film.

Figure 3.23, shows the schematic diagram of liquid bridge when the liquid is ethanol and in the upward process. Figure 3.23 (b) is a partial enlarged view of Figure 3.23 (a). The surface profile of liquid film calculated by fringe method when the distance (as shown in Figure 3.22) is 540 μm , is shown in Figure 3.23 (c). We can see that the thickness of this liquid film is very thin, and in a distance of 1800 μm , the thickness is only less than 2 μm . In Figure 3.23 (c), the contact angle β_f of the liquid film is 0.025° , and the wetting radius r_o is 3512 μm . Wetting force can be calculated according to Equation (3 – 3):

$$F_{t2} = -2\pi \times 22.4 \times 3.512 \times \sin 0.025^\circ = -0.216\mu\text{N}$$

In Figure 3.22, the wetting force calculated at distance of 540 μm using the side view method is -4 μN . We can see that the wetting force at the wetting radius r_i is much greater than the wetting force of the liquid film at the radius r_o . Therefore, when calculating the wetting force of the liquid bridge, since the wetting force generated at the liquid film is very small, it can be ignored. That is, the liquid film produced by the ethanol liquid has no additional influence on the calculation of the wetting force.

For Figure 2.21, 2.22 and 2.23, if we focus on the wetting force at the glass substrate, we will find that these wetting forces are very small compared to the Laplace pressure. This is because the contact angle of the liquid is small. When the contact angle is close to 0° , the wetting radius cannot be infinity. According to Equation (3 – 3), the calculated wetting force will also be close to zero. The contact angle and surface tension of water are large, so it can be seen that the wetting force of water is much larger than that of decane and ethanol.

Although in the process of liquid bridging and breaking, the wetting force is very small, but the role of wetting force cannot be ignored. We can see that in Figure 3.20, Figure 3.21 and Figure 3.22, as the Laplace pressure decreases, the ratio of the wetting force to the Laplace pressure increases. This trend continued until the liquid bridge broke.

3.6 Conclusion

In this chapter, we used the side view method and the total reflection observation method to perform experiment of liquid bridge on water, decane and ethanol. In the process of the experiment, the changes of the cross-linking adhesive force, the wetting radius and the meniscus are recorded. By fitting the curvature of the meniscus, we calculated the Laplace pressure. By reading the brightness of the total reflection image, we can accurately find the contact line. And at the contact line, fit the curve of surface profile of the liquid to get the contact angle. Using Equation (3 – 3), the value of wetting force is calculated.

From the experimental results, we can know that the liquid with low surface tension and good wettability has a small wetting force. Among the three liquids, ethanol has a liquid film with several microns thick. The interference fringe method is used to calculate the contact angle of the liquid film to obtain the wetting force generated by the liquid film. This wetting force is so small compared with other measured forces that it can be ignored in the calculation.

In the process of liquid bridging and breaking, the wetting force is much smaller than the Laplace pressure for most of the time. But the wetting force cannot be ignored. Because as the liquid bridge stretches, the Laplace pressure continues to decrease, and the ratio of the wetting force to the Laplace pressure becomes larger. This trend continues until the liquid bridge breaks.

When experimenting with ethanol, a liquid film with thickness of a few micrometers appears outward from the contact line. However, this liquid film has no obvious effect on the wetting force. However, due to the existence of this liquid film, after the liquid bridge is broken, the ethanol liquid on the glass substrate can spread very quickly.

References of chapter 3

- [1] Plateau, J. Experimental and threoretical researches on the figures of equilibrium of a liquid mass withdrawn from the action of gravity. The London, Edinburgh, and Dublin Philosophical Magazine and Journal of Science 1857, **14**, 1-22.
- [2] Rayleigh, L. On the capillary phenomena of jets. Proceedings of the Royal Society of London 1879, **29**, 71-97.
- [3] Jarrahbashi, D.; Sirignano, W.; Popov, P.; Hussain, F. Early spray development at high gas density: hole, ligament and bridge formations. Journal of Fluid Mechanics 2016, **792**, 186-231.
- [4] Ambravaneswaran, B.; Basaran, O.A. Effects of insoluble surfactants on the nonlinear deformation and breakup of stretching liquid bridges. Physics of Fluids 1999, **11**, 997-1015.
- [5] Gordillo, J.M.; Gekle, S. Generation and breakup of worthington jets after cavity collapse. Journal of Fluid Mechanics 2010, **663**, 331-346.
- [6] Parveen, F.; Josset, S.; Briens, C.; Berruti, F. Effect of size and density on agglomerate breakage in a fluidized bed. Powder Technology 2012, **231**, 102-111.
- [7] Rossetti, D.; Pepin, X.; Simons, S.J. Rupture energy and wetting behavior of pendular liquid bridges in relation to the spherical agglomeration process. Journal of Colloid and Interface Science 2003, **261**, 161-169.
- [8] Darabi, P.; Li, T.; Pougatch, K.; Salcudean, M.; Grecov, D. Modeling the evolution and rupture of stretching pendular liquid bridges. Chemical Engineering Science 2010, **65**, 4472-4483.
- [9] Schellenberger, F.; Papadopoulos, P.; Kappl, M.; etc. Detaching microparticles from a liquid surface. Physical Review Letters 2018, **121**, 048002.
- [10] Bina, O.; Aminshahidy, B.; Dadvar, M.; Moghadasi, J. Capillary continuity in fractured porous media; part II: Evaluation of fracture capillary pressure in the presence of liquid bridges using a novel microfluidic approach. Journal of Molecular Liquids 2020, **314**, 113666.
- [11] Taura, H.; Kaneko, S. Meniscus forces of liquid bridge between two parallel planes. Transactions of the JSME(in Japanese) 2012, **78**, 2266-2277.

4. Conclusion

In this paper, in order to study the wetting behavior of a liquid film on a super-hydrophilic surface without considering the existence of objects above the liquid blocking the laser, the interference fringe method with oblique upward laser is developed.

The features of the method used in this experiment are that: This method allows to detect the position of contact line precisely and observe the surface profile of very thin film. And due to the total reflection, the contact line can also be measured accurately at the same time. Through the verification experiment, the applicability of the calculation equation and observation method used in this experiment has been verified. The contact angle measurement is verified from 0.007° to 3° .

By using this experimental method, the spreading behavior, wetting behavior of liquid and wetting behavior in liquid bridge experiment are observed.

In the experiment of observing the spreading behavior, due to the total reflection area and partial reflection area, it is easy to determine the position of the contact line from the brightness-position curve, so that the wetting radius can be measured. It is confirmed that, the spherical radius of liquid before it spreads has a positive relationship with the time-independent fitting coefficient of Tanner's law. In the spreading process, besides surface tension, viscosity and volume, the contact angle also plays an important role and liquids with small contact angles have a larger time index.

In the experiment of observing the wetting behavior, the wetting behavior of silicon oil 1cSt droplet on a glass substrate is observed precisely. By measuring the spacing of the adjacent interference fringes which are produced by the curvature of the air-liquid interface, the surface profile of the liquid film can be calculated. During the wetting process, for the contact line, three stages can be found. They are advancing, stable and receding stage, respectively. The wetting behavior is firstly observed that there are some reciprocating changes in the two angles and the thickness of the liquid film near the contact line during the stable stage.

In the experiment of liquid bridge, the side view method and the total reflection observation method are used. In the process of the experiment, the changes of the cross-linking adhesive force, the wetting radius and the meniscus are recorded. The result shows that the liquid with low surface tension and good wettability has a small wetting force. In the process of liquid bridging and breaking, the wetting force is much smaller than the Laplace pressure for most of the time. As the liquid bridge stretches, the Laplace pressure continues to decrease, and the ratio of the wetting force to the Laplace pressure becomes larger.

Acknowledgements

This doctoral thesis started in May 2020, and I did my best to complete it in August. The content of the thesis is a summary of what I have studied in the doctoral course of Graduate School of Marine Science and Technology, Tokyo University of Marine Science and Technology. During writing this paper, I was encouraged and helped by many people. Without them, I would not have my current results, so I would like to express my deep gratitude to them. And their names are written below:

Associate Professor Kentaro Tanaka, my main instructor, took care of me when I first came to Japan from China. When I first came to a strange country, my language barrier caused a lot of inconvenience in daily life and study. It was Associate Professor Tanaka who patiently guided me to learn, and cared for my life, so that I could adapt to life and study in Japan smoothly. Especially in research, Associate Professor Tanaka has given me great help. With his help, now I have the ability to independently find problems, and solve them. Associate Professor Tanaka's education for me will be very useful all my life. Here, I sincerely thank you.

Professor Katsumi Iwamoto, my deputy instructor, is the leader of our mechanical design laboratory. "Have fun, and learn hard." is the slogan of our laboratory. It is with Professor Iwamoto that our laboratory has a cheerful learning atmosphere. In daily life, Professor Iwamoto is also very kind and caring about students. He often drinks coffee and dessert with students and chats happily. Although Professor Iwamoto is very tolerant to students, he is very serious in studying and educating students and he is a veritable teacher and friend. Professor Iwamoto has given me a lot of help in my study and life. Here, I express my deep gratitude.

Professor Tatsuya Hazuku is a rigorous and serious teacher. When educating students, Professor Hazuku can accurately point out research problems and the direction of thinking in solving problems. In my impression, Professor Hazuku is an energetic and talented teacher. In this thesis's writing, Professor Hazuku gave me a lot of important guiding opinions and suggestions. Here, I would like to express my sincere gratitude to Professor Hazuku.

Associate Professor Toshikazu Fujino, a young but very capable teacher, provided many important opinions and suggestions in my thesis. These are very useful for my research. Associate Professor Fujino is one of I respect teachers and from him, I saw the direction of my efforts in the future. Here, I express my sincere thanks to Associate Professor Fujino.

In addition, Mr. Kazuo Toyama, the technical staff member in mechanical design laboratory, also gave me a lot of help in daily life and equipment placement. There are also students Junchang Wu, Hiroto Araki, Qiyu Peng, Jun Cui, etc. who have graduated from the

mechanical design laboratory. I am very grateful to be able to study and live with you.

There are also friends who have always been in contact with me since college, such as Yuzheng Ren, Suxia Kou, Yanjun Guo, Peng Yang, etc. You often give me support and encouragement. There are also a lot of my classmates and friends whose names are not written here. I thank all of you and wish you have good health and smooth work.

Finally, the long student life is coming to an end. I want to thank my parents who gave birth to me and brought me up and my elder brother who grew up with me. I wish my family health and happiness.

Author

He Li